EXHIBIT B

GFP expression in various organs of nestin-GFP mouse 2

A. GFP expression in the retina & parts of the brain (See through the skull).
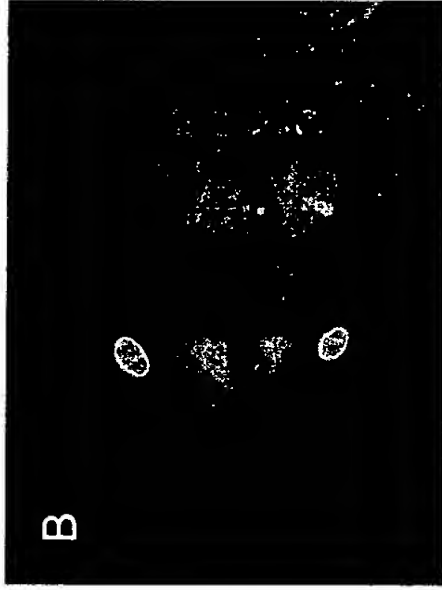
B. GFP expression in the retina & parts of the brain (Open the skull).

C. GFP expression in the inferior brain.
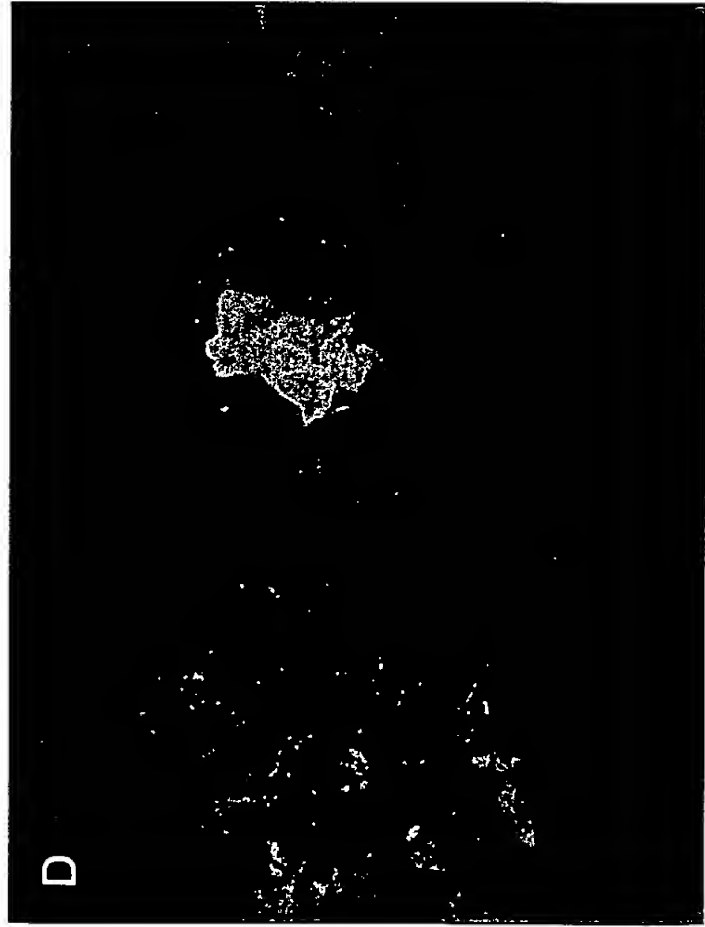
D. GFP expression in the pancreas.
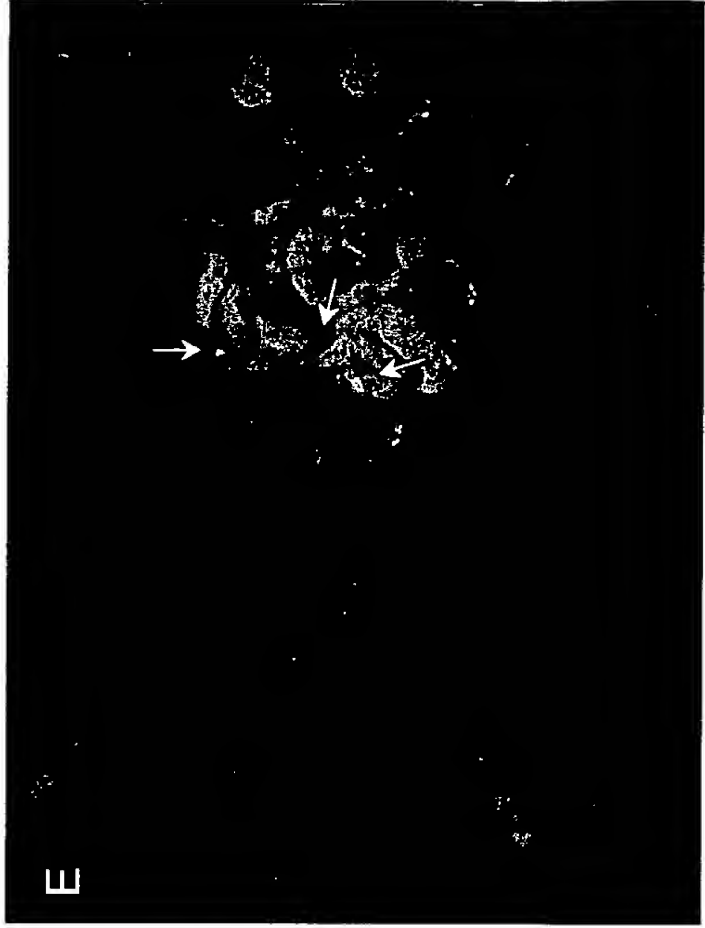
E. GFP expression in the testicles and pancreas(arrows).

DATA EXHIBITS 1A-1F.

GFP expression in the brain of nestin-GFP mouse
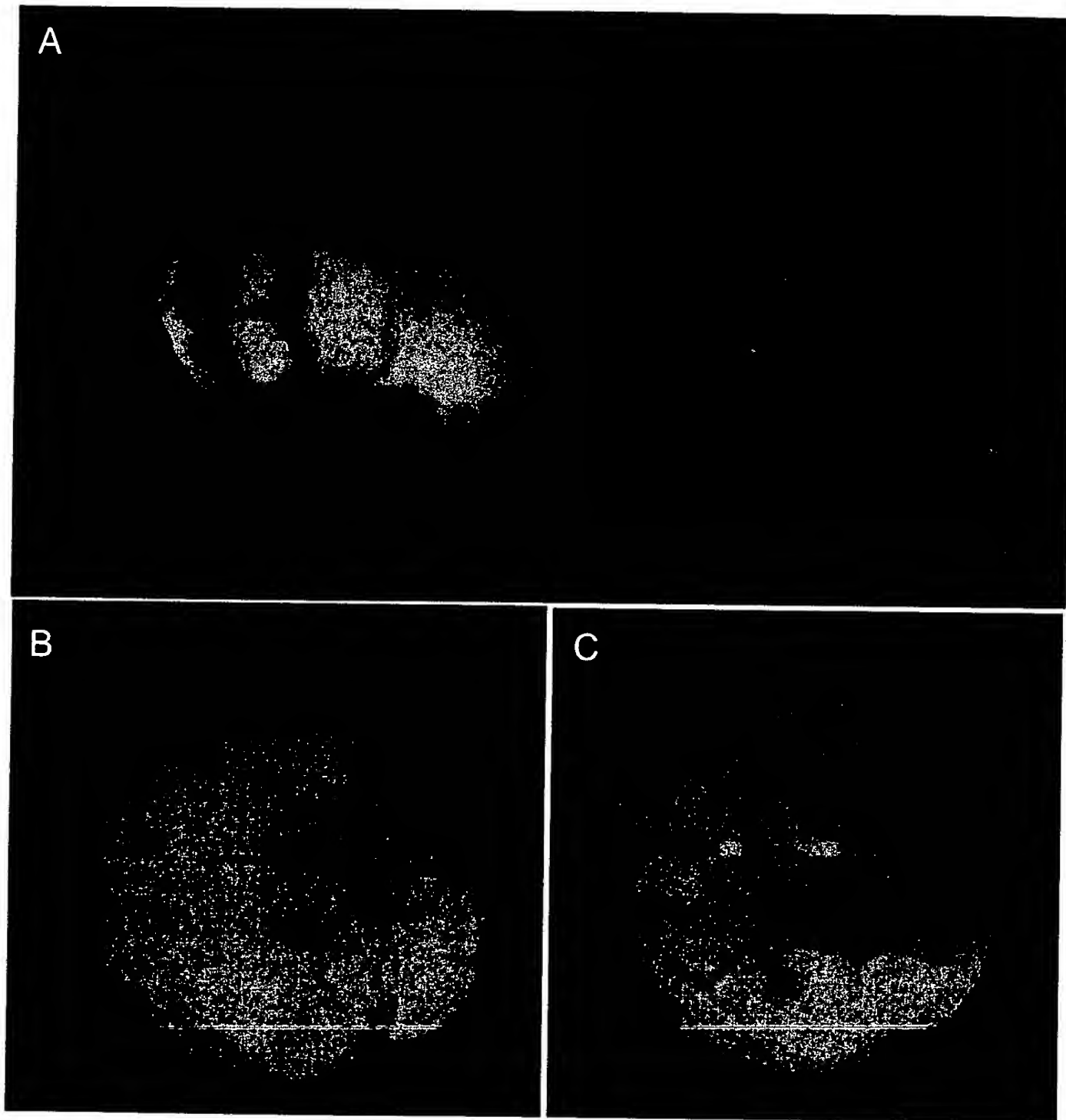
A. Whole-body image of GFP expression in the brain of a 3 week-old nestin-GFP mouse. Image was acquired through the skull via a scalp flap window. B. Direct image of GFP expression in the brain (dorsal view). B. Direct image of GFP expression in the brain (ventral view).

DATA EXHIBIT II

GFP expression in the pancreas of nestin-GFP mouse
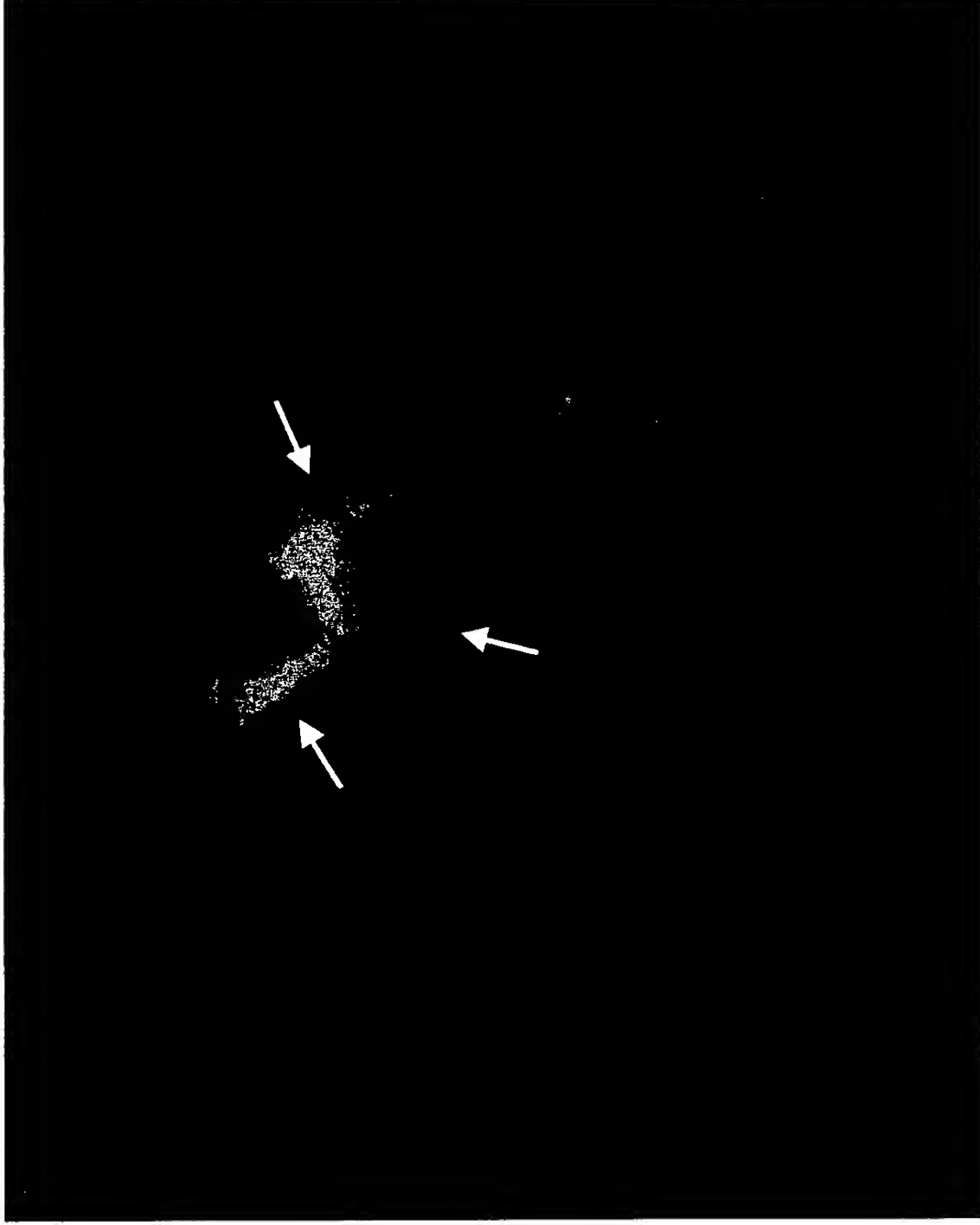
GFP expression in the pancreas of nestin-GFP mouse can be seen through the abdominal wall by opening a skin flap (arrows).

DATA EXHIBIT III

GFP expression in the pancreas of nestin-GFP mouse 2
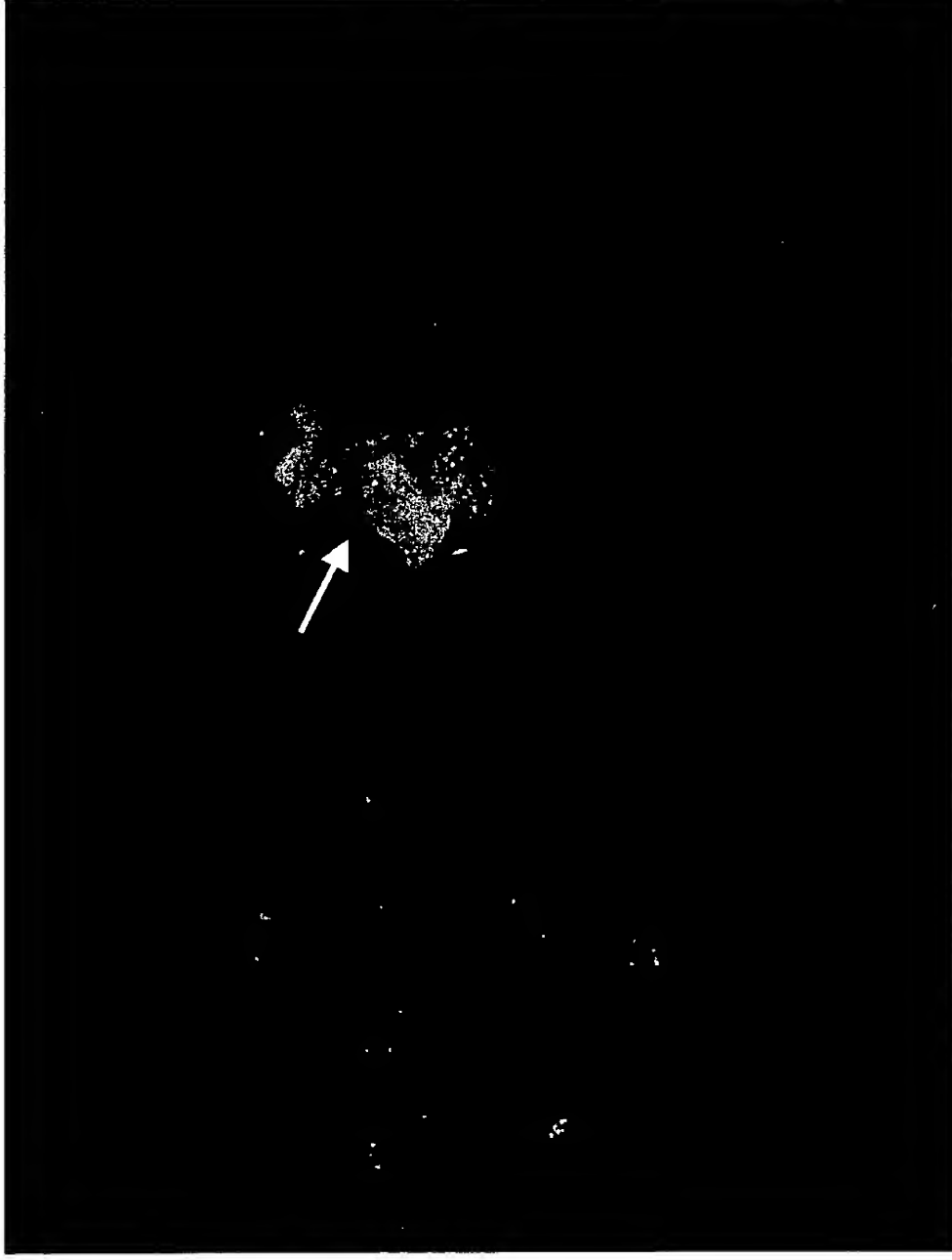
GFP expression in the pancreas (arrow).

GFP expression in the pancreas and testicles in nestin-GFP mouse
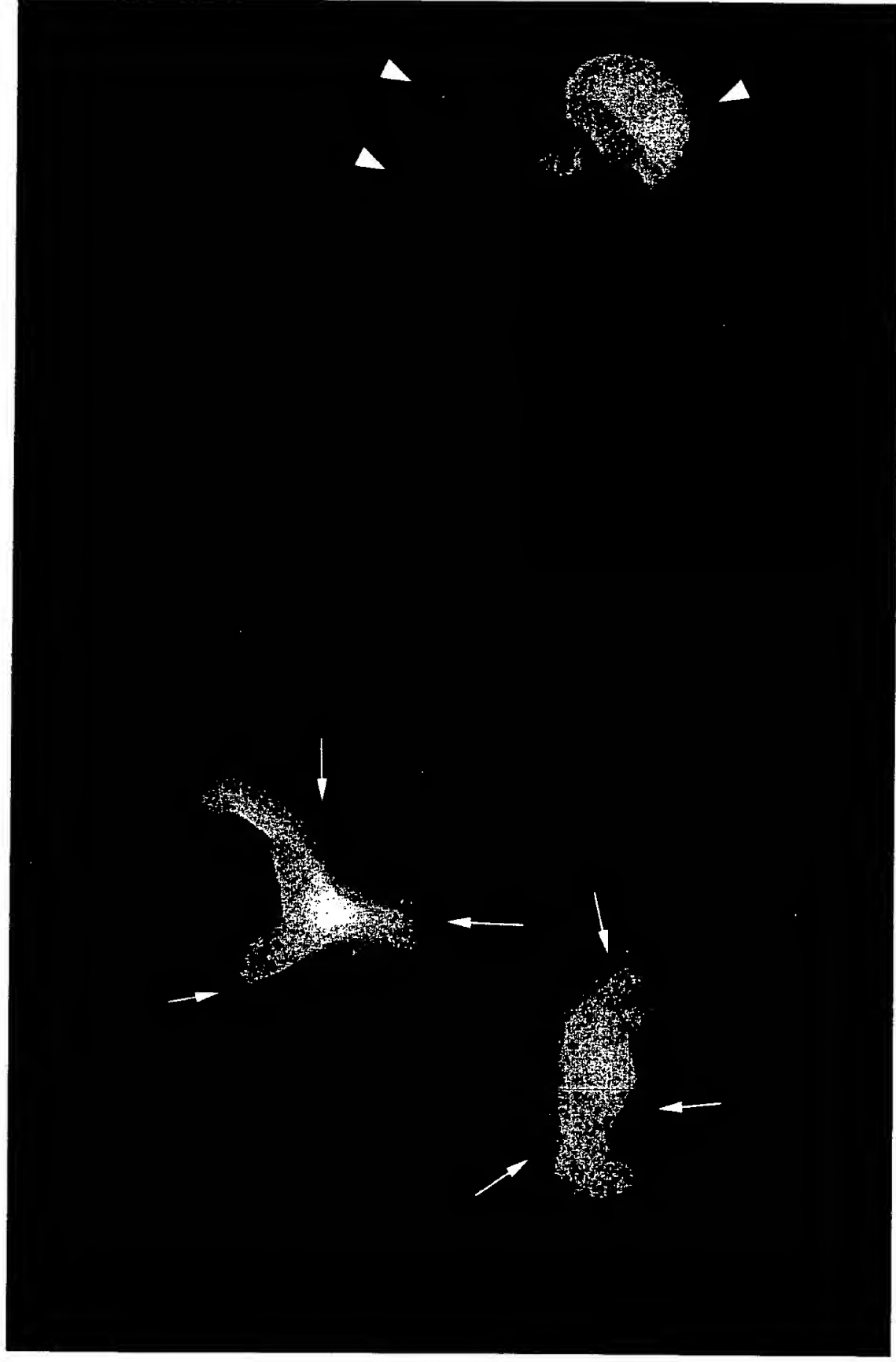
Direct image of GFP expression in the pancreas (arrows) and the testicles (arrowheads) in a 3 week-old nestin-GFP mouse.

DATA EXHIBIT V

Whole-body optical imaging of green fluorescent protein-expressing tumors and metastases

Meng Yang*[†‡], Eugene Baranov*, Ping Jiang*, Fang-Xian Sun*, Xiao-Ming Li*, Lingna Li*, Satoshi Hasegawa*[†‡], Michael Bouvet[†], Maraya Al-Tuwaijri*[†], Takashi Chishima*[†‡], Hiroshi Shimada[‡], A. R. Moossa[†], Sheldon Penman[§], and Robert M. Hoffman*[†¶]

*AntiCancer, Inc., 7917 Ostrow Street, San Diego, CA 92111; [†]Department of Surgery, University of California, 200 West Arbor Drive, San Diego, CA 92103-8220; [‡]Department of Surgery, Yokohama City University School of Medicine, Yokohama 236, Japan; and [§]Department of Biology, Massachusetts Institute of Technology, 77 Massachusetts Avenue, Cambridge, MA 02139-4307

We have imaged, in real time, fluorescent tumors growing and metastasizing in live mice. The whole-body optical imaging system is external and noninvasive. It affords unprecedented continuous visual monitoring of malignant growth and spread within intact animals. We have established new human and rodent tumors that stably express very high levels of the *Aequorea victoria* green fluorescent protein (GFP) and transplanted these to appropriate animals. B16F0-GFP mouse melanoma cells were injected into the tail vein or portal vein of 6-week-old C57BL/6 and nude mice. Whole-body optical images showed metastatic lesions in the brain, liver, and bone of B16F0-GFP that were used for real time, quantitative measurement of tumor growth in each of these organs. The AC3488-GFP human colon cancer was surgically implanted orthotopically into nude mice. Whole-body optical images showed, in real time, growth of the primary colon tumor and its metastatic lesions in the liver and skeleton. Imaging was with either a trans-illuminated epifluorescence microscope or a fluorescence light box and thermoelectrically cooled color charge-coupled device camera. The depth to which metastasis and micrometastasis could be imaged depended on their size. A 60-μm diameter tumor was detectable at a depth of 0.5 mm whereas a 1,800-μm tumor could be visualized at 2.2-mm depth. The simple, noninvasive, and highly selective imaging of growing tumors, made possible by strong GFP fluorescence, enables the detailed imaging of tumor growth and metastasis formation. This should facilitate studies of modulators of cancer growth including inhibition by potential chemotherapeutic agents.

cancer | animal model | fluorescence gene | external imaging

Current methods of external imaging of internally growing tumors include x-rays, MRI, and ultrasonography. Although these methods are well suited for the noninvasive imaging of large-scale structures in the human body (1), they have limitations in the investigation of internal growing tumors. In particular, monitoring growth and metastatic dissemination by these methods is impractical because they either use potentially harmful irradiation or require harsh contrast agents and, therefore, cannot be repeated on a frequent, real-time basis.

Optical imaging of cancers has been challenging because tumor cells usually do not have a specific optical quality that clearly distinguishes them from normal tissue. Also, conventional optical imaging has been severely limited by the strong absorbance and scattering of the illuminating light by tissue surrounding the target. As a result, neither the sensitivity nor spatial resolution of current methods is sufficient to image early-stage tumor growth or metastasis (2).

Previous attempts to endow tumors with specific, detectable spatial markers have met mostly with indifferent success. These included labeling with mAbs and other high-affinity vector molecules targeted against tumor-associated markers (3–7). However, results were limited due to a low tumor/background contrast and by the toxicity of the procedures.

Intravital videomicroscopy (IVVM) is another approach to optical imaging of tumor cells. IVVM allows direct observation of cancer cells but only if they are visible in the blood vessels (8). Even in this limited arena, IVVM does not lend itself to following tumor growth, progression, and internal metastasis in a live, intact animal.

A major conceptual advance in optical imaging was to make the target tumor the source of light. This renders the incident light scattering much less relevant. One early attempt inserted the luciferase gene into tumors so that they emit light (9). However, luciferase enzymes transferred to mammalian cells require the exogenous delivery of their luciferin substrate, an essentially impractical requirement in an intact animal. Also, it is not known whether luciferase genes can function stably over significant time periods in tumors and in the metastases derived from them.

A more practical approach to tumor luminance is to make the target tissue selectively fluorescent. Tumor-bearing animals were infused with protease-activated, near-infrared fluorescent probes (10). Tumors with appropriate proteases could activate the probes and be imaged externally. However, the system proved to have severe restrictions. The selectivity was limited because most normal tissues have significant protease activity. In fact, the normal activity in liver is so high as to preclude imaging in this most important of metastatic sites. The short lifetime of the fluorescence probes would appear to rule out growth and efficacy studies. The requirement of appropriate, tumor-specific protease activity and the requirement of effective tumor delivery of the probes also limit this approach (10).

We report here a new approach to producing tumors whose fluorescence can be viewed externally in intact animals. This is an extension of our previous work, which used stable green fluorescent protein (GFP) expression in cancer cells as an extremely effective tumor cell marker in conventional diagnostic dissections. The fluorescence-enhanced sensitivity illuminated tumor progression and allowed detection of metastases in exposed or isolated fresh visceral organs and tissues down to the single-cell level (11). Tracking of cancer cells that stably express GFP *in vivo* is far more sensitive and rapid than the traditional, cumbersome procedures of histopathological examination or immunohistochemistry. In particular, GFP labeling markedly improved the ability to visualize metastases in fresh soft organs and bone (11–18).

A major advantage of GFP-expressing tumor cells is that imaging requires no preparative procedures and, therefore, is uniquely suited for visualizing in live tissue (11–18). Using stable, high-GFP-expression tumor cells that we have selected (11–18),
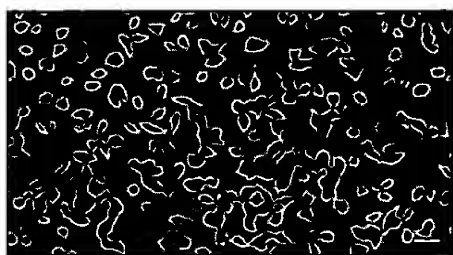
Fig. 1. Stable, high-level GFP-expressing B16F0 murine melanoma transductants *in vitro*. The murine malignant melanoma cell line B16F0 was transduced previously with the RetroXpress vector pLEIN, which expresses EGFP (19) and the neomycin resistance gene on the same bicistronic message (18). Stable, high-expression clones were selected in 800 μg/ml G418 (18). (Bar = 40 μm.)

we demonstrate external, noninvasive, whole-body, real-time fluorescence optical imaging of internally growing tumors and metastases in transplanted animals.

Materials and Methods

Microscopy. A Leica fluorescence stereo microscope (model LZ12) equipped with a mercury 50-W lamp power supply was used. Selective excitation of GFP was produced through a D425/60 band-pass filter and 470 DCXR dichroic mirror. Emitted fluorescence was collected through a long-pass filter (GG475; Chroma Technology, Brattleboro, VT) on a Hamamatsu C5810 three-chip cooled color charge-coupled-device camera (Hamamatsu Photonics Systems, Hamamatsu City, Japan). Images were processed for contrast and brightness and analyzed with the use of IMAGE PRO PLUS 3.1 software (Media Cybernetics, Silver Springs, MD). High-resolution images of 1,024 × 724 pixels were captured directly on an IBM PC or continuously through video output on a high-resolution Sony VCR, model SLV-R1000 (Sony, Tokyo).

Doubling Time of Stable GFP Clones. B16F0-GFP (18) or nontransduced cells were seeded at 1.5 × 10^4 in 35-mm culture dishes. The cells were harvested and counted every 24 hr with a hemocytometer (Reichert). The doubling time was calculated from the cell-growth curve over 6 days (data not shown).

Animals and Cell Injection. Six-week-old female B57CL/6 mice were injected with 10^6 B16F0-GFP cells in the lateral tail vein. Cells first were harvested by trypsinization and washed three times with cold serum-free medium and then injected in a total volume of 0.2 ml by using a 1-ml 27G2 latex-free syringe (Becton Dickinson) within 30 min of harvesting. Six-week-old BALB/c *nu/nu* male and female mice were transplanted with 10^6 B16F0-GFP cells in the lateral tail vein or portal vein by using the same method as described above.

All animal studies were conducted in accordance with the principles and procedures outlined in the National Institutes of Health Guide for the Care and Use of Animals under assurance number A3873-1. Mice were fed with autoclaved laboratory rodent diet (Tecklad LM-485; Western Research Products, Orange, CA).

Surgical Orthotopic Implantation (SOI) (20). Tumor fragments (1 mm^3) from the liver-metastatic AC3488 tumor (21), stably expressing GFP after *in vivo* transduction (M.Y. and R.H.M., unpublished data), were implanted by SOI in nude mice. During proper exposure of the colon after a lower midline abdominal incision, the serosa of the colon was removed and two pieces of 1-mm^3 tumor fragments per mouse were implanted. An 8-0 surgical suture was used to penetrate these small tumor pieces and suture them on the wall of the intestine, which then was
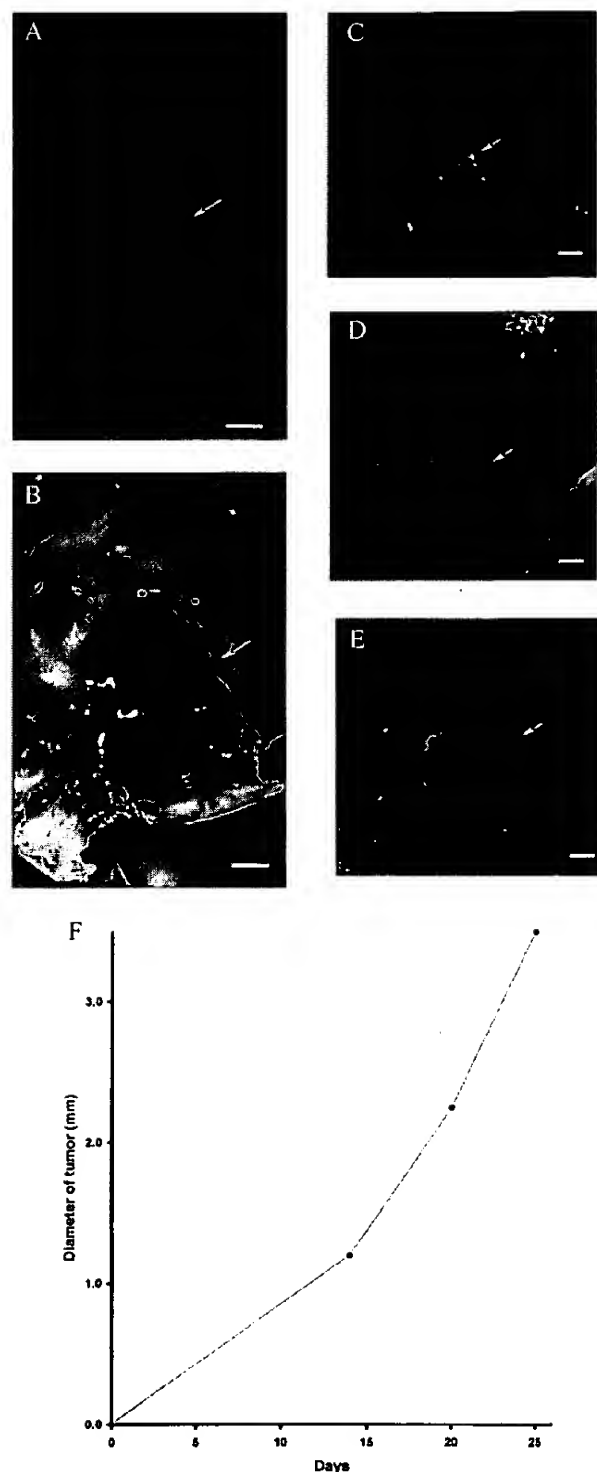
Fig. 2. External images of murine melanoma (B16F0-GFP) metastasis in brain. Murine melanoma metastases in the mouse brain were imaged by GFP expression under fluorescence microscopy. Clear images of metastatic lesions in the brain can be visualized through the scalp and skull. See *Materials and Methods* for imaging equipment and procedures. (*A*) External GFP image of brain metastasis through the scalp and scull of an intact mouse 3 weeks after injection of 10^6 B16F0-GFP cells in the tail vein. (Bar = 1,280 μm.) (*B*) GFP image of same area as in *A*, with skull opened. (Bar = 1,280 μm.) (*C*) External image obtained of the tumor in the brain of the nude mouse on day 14 after GFP tumor cell injection. (Bar = 1,280 μm.) (*D*) Same as *C*, day 19 after injection. (Bar = 1,280 μm.) (*E*) Same as *C* and *D*, day 25 after injection. (Bar = 1,280 μm.) (*F*) Brain tumor growth curve determined by external images (*C-E*).

MEDICAL SCIENCES

14 days

20 days

25 days

F

Days

Fig. 3. External images of B16F0-GFP bone metastasis. In the proximal tibia of the left hind leg of C57BL/6 mouse (hair removed). No metastasis can be detected under bright-field microscopy (A). Clear, external images of metastatic lesions of B16F0-GFP in the proximal tibia of the intact mouse were obtained under fluorescence microscopy (B). Time course metastatic growth of B16F0-GFP in the proximal tibia of the intact nude mouse was imaged externally under fluorescence microscopy (C–E). (A) Bright-field microscopy of knee joint of hind leg. (Bar = 640 μm.) (B) Same as A; external fluorescent image of knee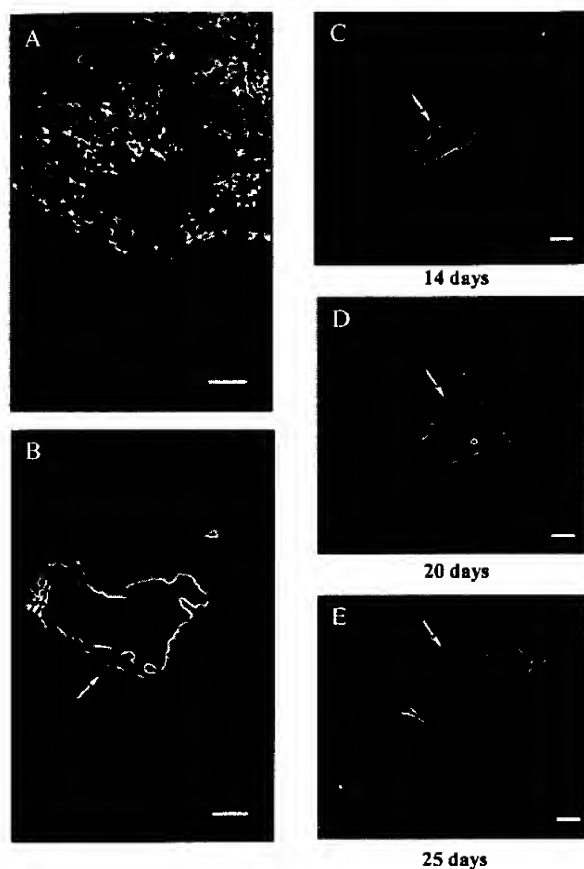 joint visualizing extensive melanoma metastasis, day 21 after injection. (Bar = 640 μm.) (C) External image obtained in tibia of nude mouse day 14 after tail vein injection. (Bar = 640 μm.) (D) Same as C, day 20. (Bar = 640 μm.) (E) Same as C and D, day 25. (Bar = 640 μm.) (F) Growth curve of tibia metastatic lesion determined by external images (Fig. 2 C–E).
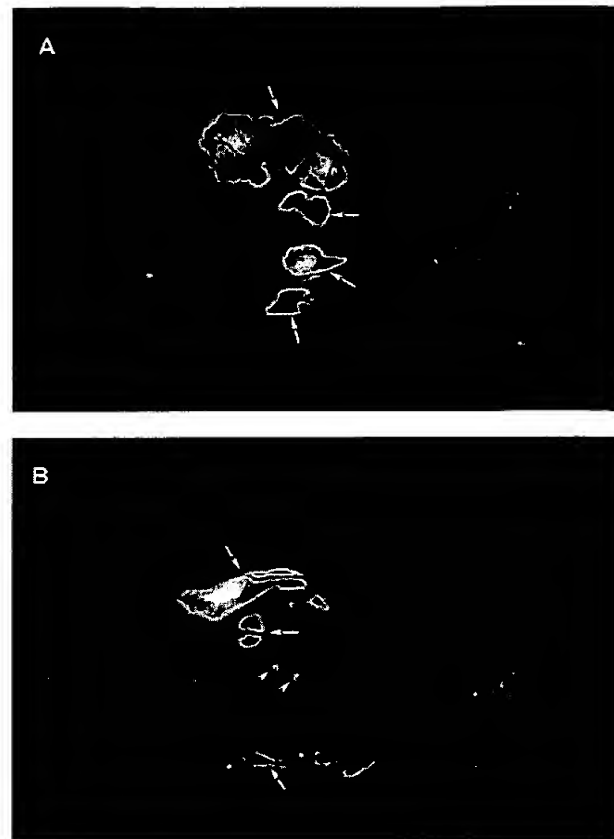

Fig. 4. External images of B16F0-GFP colonizing the liver. A metastatic lesion of B16F0-GFP in the liver growing at a depth of 0.8 mm after portal vein injection was externally imaged through the abdominal wall of the intact nude mouse. (A) An external image of multilobe liver metastases of the B16F0-GFP cells (large arrows). (B) An external image of small liver metastatic lesions of approximately 1.5 mm in diameter (small arrows) and other larger metastatic lesions (large arrows).

returned to the abdominal cavity. The incision in the abdominal wall was closed with a 7-0 surgical suture in one layer (20). The animals were kept under isofluorane anesthesia during surgery. All procedures of the operation described above were performed with a ×7 magnification microscope (MZ6; Leica, Deerfield, IL). Animals were kept in a barrier facility under HEPA filtration (20).

Analysis of Metastases. Periodically, the tumor-bearing mice were examined by whole-body fluorescence microscopy or in a fluorescence light box (Lightools Research, Encinitas, CA), as described above. In the case of C57BL/6 mice, hair was removed with Nair (Carter–Wallace, New York, NY).

Fluorescent Cross-Section. A cross-section was made at the position, as shown in Fig. 5B, to simulate tomography and localize the external images. The animals were sacrificed and kept frozen after external fluorescence images were acquired. The whole mouse then was sliced in cross-section at approximately 1-mm thickness by using disposable microtome blades (Model 818; Leica). The sections then were observed directly under fluorescence microscopy.

Determination of Minimum GFP-Expressing Tumor Size Externally Imaged at Various Depths. A Leica MZ12 fluorescence microscope coupled with a Hamamatsu C5810 three-chip cooled color
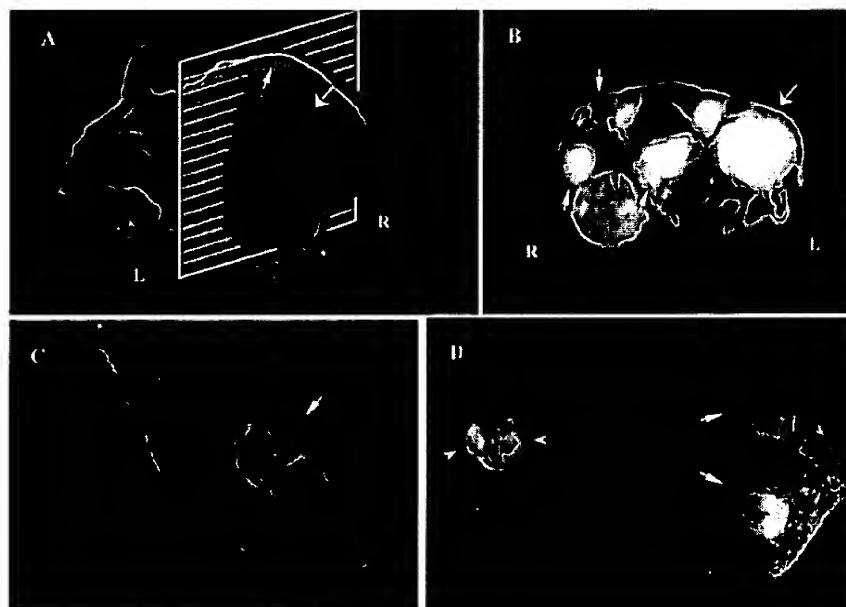
Fig. 5. External and internal images of liver lesions of AC3488-GFP. (A) Lateral, whole-body image of metastatic liver lesions of a GFP-expressing human colon cancer in the left (thick arrow) and right lobes (fine arrow) of a live nude mouse at day 21 after surgical orthotopic transplantation. (B) Cross-section of mouse shown in A corresponding to the level of the external image of the tumor in the liver that was acquired (A). Fine arrows show metastatic lesions in the right lobe of liver, and the thick arrow shows the metastatic lesion in the left lobe of liver. (C) Fluorescent whole-body ventral image of primary colon tumor (arrow). (D) Dorsal external image of metastatic tumor in the caudal region of the left and right lobes of the liver (thick arrows) and skull metastasis (arrowheads).

charge-coupled-device camera was used to acquire the images as described above. The actual size of the GFP-expressing tumors or metastases externally imaged was measured directly by imaging the GFP-expressing tumor after direct exposure of the tumor-containing tissue. Tumor specimen size is expressed as a diameter assuming spherical geometry. The depth of the GFP-expressing tumors was determined in isolated tissues by acquiring calibrated images with IMAGE PRO PLUS 3.1 software.

Results

Isolation of Stable, High-Level Expression GFP Transductants of B16F0-GFP Cells. GFP- and neomycin-transduced B16F0 cells were selected previously in multiple steps for growth in levels of Geneticin (G418) up to 800 μg/ml and for high GFP expression (18). The selected B16F0-GFP cells have a strikingly bright GFP fluorescence that remains stable in the absence of selective agents after numerous passages (18) (Fig. 1). There was no difference in the doubling times of parental cells and selected transductants as determined by comparison of proliferation in monolayer culture (data not shown).

External Images of Internally Growing B16F0-GFP Tumors. Metastatic lesions of B16F0-GFP in the brain, bone, liver, and lymph nodes were externally imaged by GFP expression in intact mice after tail vein or portal vein cell injection of B16F0-GFP cells (Figs. 2, 3, and 4).

External Images of Brain Metastasis of B16F0-GFP. A comparison was made between an external and direct image of a brain metastasis of B16F0-GFP. A fluorescent image (5.5 mm in diameter and 0.8 mm in depth) of B16F0-GFP cells was obtained externally through the scalp and skull of a C57BL/6 mouse (Fig. 2A). The externally acquired image closely matched the image acquired from the open brain after the scalp and skull were removed (Fig. 2B). A series of external fluorescence images of the B16F0-GFP brain tumor in a single animal was obtained from day 14 to day

25 after tail vein injection of B16F0-GFP in a nude mouse. As determined by external imaging, the size of the metastatic lesion grew progressively with time (Fig. 2 C–E). The size of the external image was ≈1.2 mm in diameter at day 14, ≈2.25 mm at day 20, and ≈3.5 mm at day 25.

External Images of Bone Metastasis of B16F0-GFP. An example of an external fluorescence image of a B16F0-GFP bone metastasis is shown in Fig. 3. The tumor was ≈0.8 mm deep and 2.33 mm in equivalent diameter. The image was acquired at day 21 after tail vein injection. External fluorescent images were acquired throughout the axial skeleton, including the skull, scapula, femur, tibia, and pelvis. Fig. 3 C–E shows a series of external fluorescence images of a tumor in the tibia that were obtained from day 14 to day 25 after tail vein injection of B16F0-GFP in nude mice. The size of the metastatic lesion was ≈0.96 mm in diameter at day 14, ≈1.76 mm at day 20, and ≈3.14 mm at day 25 (Fig. 3F).

External Images of Liver Metastasis of B16FP-GFP. Metastatic lesions of B16F0-GFP in the nude mouse liver were formed after portal vein injection. A clear external image of multiple metastatic lesions in the liver could be seen through the abdominal wall of the intact mouse at a depth of 0.8 mm (Fig. 4). The image was comparable to the image acquired from the exposed liver (data not shown).

External Images of the AC3488 GFP Human Colon Tumor. Fluorescent images of the primary colon tumor, multilobe liver metastases, and a skull metastases are shown in Fig. 5. A lateral view of the mouse demonstrates fluorescent liver metastases on the left and right lobes of the liver (Fig. 5A). A cross-section of the mouse, simulating a tomograph, internally localizes the external lateral images of metastatic tumor in the left and right lobes of the liver (Fig. 5B). A dorsal view of the mouse shows the images of metastatic tumors on the caudal portion of these two lobes of the
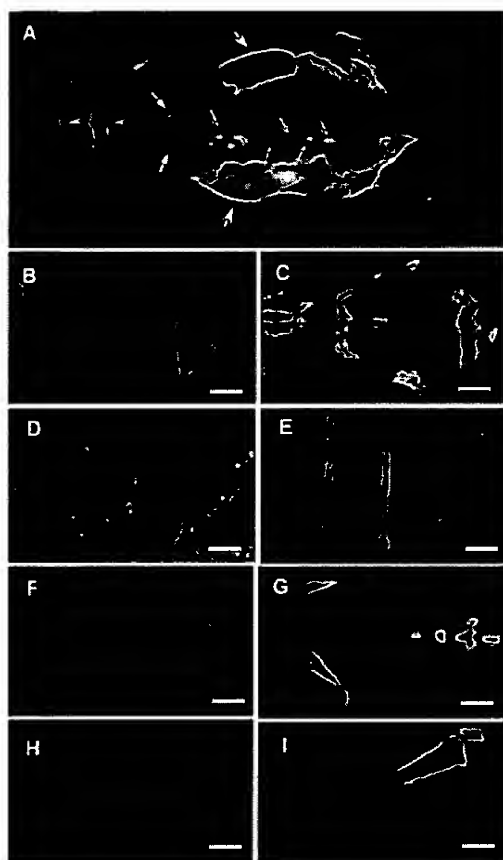
Fig. 6. External and internal images of bone metastasis of AC3488 GFP. External fluorescent whole-body images compared with direct images of skeletal metastases. (*A*) External images of tumors in the skeletal system including the skull (arrow heads), scapula (thick arrows), spine (fine arrows), and liver metastasis (largest arrows) in a dorsal view of live, intact nude mouse. (*B–I*) Series of external fluorescence images of metastatic lesions in the skull, ribs, spine, and tibia, (*B*, *D*, *F*, and *H*) compared with corresponding images of the exposed skeletal metastases (*C*, *E*, *G*, and *I*) (Bars = 1280 μm).

Table 1. Minimum-sized fluorescent optical tumor images at increasing depth

Depth, mm	Minimum-sized tumor imaged, μm (equivalent diameter)
0.5	59
0.6	100
0.7	210
0.8	250
1	283
1.3	488
2.2	1,861

Tumor images were acquired with a Leica MZ12 microscope coupled with a Hamamatsu C5810 three-chip cooled color charge-coupled device camera. See *Materials and Methods* for details.

liver (Fig. 5*D*). The primary colon tumor is imaged in a ventral view of the mouse and suggests local–regional spread (Fig. 5*C*).

External Images of Skeletal Metastasis of AC3488 GFP. External fluorescent images of colon tumor metastases throughout the nude mouse skeleton were acquired and compared with direct images of the exposed metastatic lesions (Fig. 6). Fig. 6*A* shows external, whole-body images of tumors in the skeletal system including the skull, scapula, and spine in a dorsal view of a live, intact nude mouse. External and direct images of the bone metastases were compared. Fig. 6 *B–I* shows a series of external fluorescent images of metastatic lesions in the skull, ribs, spine, and tibia, which are compared with corresponding images of these skeletal sites acquired after direct exposure of the metastases. It can be seen that the external images correspond highly to the images of the exposed metastatic lesions.

Imaging Sensitivity and Resolution. GFP-expressing primary and metastatic lesions were considered to be externally measurable if the average fluorescence of the GFP-expressing tumor was at least 20% above the average fluorescence of the surrounding skin. The level of background dorsal and abdominal skin fluorescence of nude mice was in a range of 6–9% of the exposed tumor fluorescence. The intensity of GFP fluorescence of a

tumor (1 mm in diameter) growing at a depth of ≈0.8 mm was approximately ≈25% of that of the exposed tumor. The minimum tumor size that could be imaged was a function of depth. The range of minimal size of GFP-expressing tumors that have been imaged externally thus far was from ≈59 μm in diameter at a depth of 0.5 mm to ≈1.86 mm in diameter at a depth of 2.2 mm in various tissues (Table 1).

External imaging can provide invaluable real-time data for tracking tumor growth and metastasis formation in live, intact animals. Melanoma metastases in the brain and tibia were imaged over 11 days when they grew from 1.2 to 3.5 mm (Fig. 2 *C–F*) and from 0.95 to 3.14 mm (Fig. 3 *C–F*) in equivalent diameter, respectively.

Discussion

The GFP-based fluorescent optical tumor imaging system presents many powerful features. Only the tumors and metastases contain the heritable GFP gene and therefore are selectively imaged with very high intrinsic contrast to other tissues. GFP expression in the tumor cells is stable over indefinite time periods, allowing the quantitative imaging of tumor growth and metastasis formation as well as their inhibition by agents of all types. The very bright GFP fluorescence enables internal tumors and metastases to be observed externally in critical organs such as colon, liver, bone, brain, pancreas (data not shown), and, presumably, breast, lymph nodes, prostate, etc. No contrast agents or other compounds or treatment need to be administered to the animals; only blue light illumination is necessary.

Current sensitivity is limited, in part, by the nonoptimal spectrum of the green GFP fluorescence (520 nm). At this relatively short wavelength, the emitted radiation is strongly scattered by surrounding tissue. However, powerful new techniques of using ultrafast lasers (22), dual photon imaging (23), and ballistic photon imaging (24, 25) may offer large gains in sensitivity, increased depth of detection, and spatial resolution.

The experiments with the B16 melanoma utilized tumor cells that were labeled by external GFP transduction and implanted. However, external labeling is not a necessary limitation on the technique. Recent findings in our laboratory suggest that *in situ* labeling, with the GFP gene, of tumors growing *in vivo* is feasible, as shown by the labeling of AC3488 colon tumor in this study (S.H., M.Y., and R.M.H., unpublished data). A wide variety of tumors now can be followed for subsequent tumor growth, spread, and metastases, all reported by inherited GFP expression.

GFP does not appear to be antigenic in either the nude mouse or normal C57B1/6 mouse, because long-term tumor growth and metastasis readily occur in these animals. This new technology will be of very broad use for the understanding of tumor growth and metastasis as well as therapy.

1. Tearney, G. J., Brezinski, M. E., Bouma, B. E., Boppart, S. A., Pitris, C., Southern, J. F. & Fujimoto, J. G. (1997) *Science* 276, 2037–2039.
2. Taubes, G. (1997) *Science* 276, 1991–1993.
3. Baum, P. R. & Brummendorf, T. H. (1998) *Q. J. Nucleic Med.* 42, 33–42.
4. Teates, C. D. & Parekh, J. S. (1993) *Curr. Probl. Diagn. Radiol.* 22, 229–226.
5. Dessureault, S. (1997) *Breast Cancer Res. Treat.* 45, 29–37.
6. Pasqualini, R., Koivunen, E. & Ruoslahti, R. (1997) *Nat. Biotechnol.* 15, 542–546.
7. Neri, D., Carnelmolla, B., Nissim, A., Leprini, A., Querze, G., Balza, E., Pini, A., Tarli, L., Halin, C., Neri, P., *et al.* (1997) *Nat. Biotechnol.* 15, 1271–1275.
8. Chambers, A. F., MacDonald, I. C., Schmidt, E. E., Koop, S., Morris, V. L., Khokha, R. & Groom, A. C. (1995) *Cancer Metastasis Rev.* 14, 279–301.
9. Sweeney, T. J., Mailander, V., Tucker, A. A., Olomu, A. B., Zhang, W., Cao, Y.-A., Negrin, R. S. & Contag, C. H. (1999) *Proc. Natl. Acad. Sci. USA* 96, 12044–12049.
10. Weissleder, R., Tung, C. H., Mahmood, U. & Bogdanov, A., Jr. (1999) *Nat. Biotechnol.* 17, 375–378.
11. Chishima, T., Miyagi, Y., Wang, X., Yamaoka, H., Shimada, H., Moossa, A. R. & Hoffman, R. M. (1997) *Cancer Res.* 57, 2042–2047.
12. Chishima, T., Miyagi, Y., Wang, X., Tan, Y., Shimada, H., Moossa, A. R. & Hoffman, R. M. (1997) *Anticancer Res.* 17, 2377–2384.
13. Chishima, T. Miyagi, Y., Wang, X., Baranov, E., Tan, Y., Shimada, H., Moossa, A. R. & Hoffman, R. M. (1997) *Clin. Exp. Metastasis* 15, 547–552.
14. Chishima, T., Miyagi, Y., Li, L., Tan, Y., Baranov, E., Yang, M., Shimada, H., Moossa, A. R. & Hoffman, R. M. (1997) *In Vitro Cell Dev. Biol. Animal* 33, 745–747.
15. Chishima, T., Yang, M., Miyagi, Y., Li, L., Tan, Y., Baranov, E., Shimada, H., Moossa, A. R., Penman, S. & Hoffman, R. M. (1997) *Proc. Natl. Acad. Sci. USA* 94, 11573–11576.
16. Yang, M., Hasegawa, S., Jiang, P., Wang, X., Tan, Y., Chishima, T., Shimada, H., Moossa, A. R. & Hoffman, R. M. (1998) *Cancer Res.* 58, 4217–4221.
17. Yang, M., Jiang, P., Sun, F.-X., Hasegawa, S., Baranov, E., Chishima, T., Shimada, H., Moossa, A. R. & Hoffman, R. M. (1999) *Cancer Res.* 59, 781–786.
18. Yang, M., Jiang, P., An, Z., Baranov, E., Li, L., Hasegawa, S., Al-Tuwaijri, M., Chishima, T., Shimada, H., Moossa, A. R. & Hoffman, R. M. (1999) *Clin. Cancer Res.*, 5, 3549–3559.
19. Flotte, T. R., Beck, S. E., Chesnet, K., Potter, M., Poirier, A. & Zolotukhin, S. (1998) *Gene Ther.* 5, 166–173.
20. Fu, X., Besterman, J. M., Monosov, A. & Hoffman, R. M. (1991) *Proc. Natl. Acad. Sci. USA* 88, 9345–9349.
21. Sun, F.-X., Sasson, A. R., Jiang, P., An, Z., Gamagami, R., Li, L., Moossa, A. R. & Hoffman, R. M. (1999) *Clin. Exp. Metastasis* 17, 41–48.
22. Alfano, R. R., Demos, S. G. & Gayen, S. K. (1997) *Ann. N. Y. Acad. Sci.* 820, 248–270.
23. Masters, B. R., So, P. T. & Gratton, E. (1998) *Ann. N. Y. Acad. Sci.* 838, 58–67.
24. Wu, J., Perelman, L., Dasari, R. & Feld, M. (1997) *Proc. Natl. Acad. Sci. USA* 94, 8783–8788.
25. Alfano, R. R., Demos, S. G., Galland, P., Gayen, S. K., Guo, Y., Ho, P. P., Liang, X., Liu, F., Wang, L., Wang, Q. Z., *et al.* (1998) *Ann. N. Y. Acad. Sci.* 838, 14–28.

Direct external imaging of nascent cancer, tumor progression, angiogenesis, and metastasis on internal organs in the fluorescent orthotopic model

Meng Yang*, Eugene Baranov*, Jin-Wei Wang*, Ping Jiang*, Xiaoen Wang*, Fang-Xian Sun*, Michael Bouvet†, A. R. Moossa†, Sheldon Penman‡, and Robert M. Hoffman*†§

*AntiCancer, Inc., 7917 Ostrow Street, San Diego, CA 92111; †Department of Surgery, University of California, 200 West Arbor Drive, San Diego, CA 92103-8220; and ‡Department of Biology, Massachusetts Institute of Technology, 77 Massachusetts Avenue, Cambridge, MA 02139-4307

Mouse tumor models have undergone profound improvements in the fidelity of emulating human disease. Replacing ectopic s.c. implantation with organ-specific orthotopic implantation reproduces human tumor growth and metastasis. Strong fluorescent labeling with green fluorescent protein along with inexpensive video detectors, positioned externally to the mouse, allows the monitoring of details of tumor growth, angiogenesis, and metastatic spread. However, the sensitivity of external imaging is limited by light scattering in intervening tissue, most especially in skin. Opening a reversible skin-flap in the light path markedly reduces signal attenuation, increasing detection sensitivity many-fold. The observable depth of tissue is thereby greatly increased and many tumors that were previously hidden are now clearly observable. This report presents tumor images and related quantitative growth data previously impossible to obtain. Single tumor cells, expressing green fluorescent protein, were seeded on the brain image through a scalp skin-flap. Lung tumor microfoci representing a few cells are viewed through a skin-flap over the chest wall, while contralateral micrometastases were imaged through the corresponding skin-flap. Pancreatic tumors and their angiogenic microvessels were imaged by means of a peritoneal wall skin-flap. A skin-flap over the liver allowed imaging of physiologically relevant micrometastases originating in an orthotopically implanted tumor. Single tumor cells on the liver arising from intraportal injection also were detectable. Possible future technical developments are suggested by the image, through a lower-abdominal skin-flap, of an invasive prostate tumor expressing both red and green fluorescent proteins in separate colonies.

skin-flap window | GFP | RFP | micrometastasis | dormancy

A nimal models of human cancer have undergone profound improvements. For many years these simply consisted of ectopic, s.c. implantation of human tumors into immunodeficient mice. Such models usually differed radically from the original donor tumor. For example, such tumors were usually encapsulated (unlike most donor tissue), had radically altered growth characteristics, and, most importantly, did not exhibit metastatic behavior. Also, the important early stages of tumor development were essentially hidden.

Among the attempts to overcome these limitations were skin-fold chambers, intravital microscopy of exteriorized organs, and s.c. windows composed of semitransparent material (1–3). However, none of these techniques have been widely adopted because they are suitable primarily for ectopic models and for relatively short periods of observation. One application of the dorsal skin chamber in mice used two-photon confocal microscopy to examine tumor gene expression, angiogenesis, and physiology in a green fluorescent protein (GFP)-expressing tumor (1). Such studies are, however, limited to the ectopic primary tumor and can provide only limited information. Another approach was intravital microscopy of GFP-expressing tumors on exteriorized organs (3). However, the serious morbidity of the procedure precluded long-term spatial-temporal studies.

The greatest fidelity to donor cancer tissue was achieved with GFP models employing orthotopically implanted tumors (4–14). These tumors closely emulate the metastatic behavior of the donor in rate and seed similar target tissues. Also, the GFP-expressing tumors were sufficiently bright that they often could be viewed through simple video equipment situated externally to the animal (13). However, the sensitivity of tumor visualization was limited by absorption through overlying tissue and worked best for relatively shallow tumors. In this report, we shall show that much of this absorption is caused by scattering in the skin. The simple expedient of introducing a minimally invasive, reversible skin flap can increase sensitivity of detection, often by an order of magnitude or more. This increase makes possible direct observation of tumor growth and metastasis as well as tumor angiogenesis and gene expression. The images revealed the microscopic stages of tumor growth and metastatic seeding, often down to the single-cell level, as well as later stages of tumor spread and angiogenesis. Perhaps most importantly, the ability to follow tumor cells in a relatively noninvasive manner in the intact animal makes possible previously unobtainable precision in the studies of tumor behavior and response to chemotherapeutic agents.

Materials and Methods

Expression Vectors. The pLEIN and pLNCX₂ vectors were purchased from CLONTECH. The pLEIN vector expresses enhanced green fluorescent protein and the neomycin resistance gene on the same bicistronic message that contains an internal ribosome expression site. The pLNCX₂ vector contains the neomycin resistance gene for antibiotic selection in eukaryotic cells (13–15). The red fluorescent protein (RFP; DsRed2, CLONTECH; ref. 16) was inserted in the pLNCX₂ vector at the Egl II and NotI sites.

GFP Vector Production. For retroviral transduction, PT67, an NIH 3T3-derived packaging cell line expressing the 10 A1 viral envelope, was purchased from CLONTECH. PT67 cells were cultured in DMEM (Irvine Scientific) supplemented with 10% (vol/vol) heat-inactivated FBS (Gemini Biological Products, Calabasas, CA). For vector production, packaging cells (PT67) at 70% confluence were incubated with a precipitated mixture of DOTAP transfection reagent (N-[1-(2,3-dioleoyloxy)propyl]-N,N,N-trimethylammonium methylsulfate; Roche Molecular Biochemicals) and saturating amounts of pLEIN for 18 h. Fresh medium was replenished at this time. The cells were examined by fluorescence microscopy 48 h after transfection. For selection, the cells were cultured in the

presence of 500–2,000 μg/ml of G418 increased in a step-wise manner (Life Technologies, Grand Island, NY) for 7 days.

GFP Gene Transduction of Human and Animal Tumor Cell Lines. For GFP gene transduction, 20–40% confluent human and animal tumor cells were incubated with a 1:1 precipitated mixture of retroviral supernatants of PT67 cells and RPMI medium 1640 or other culture media (GIBCO) containing 10% (vol/vol) FBS (Gemini Biological Products) for 72 h. Human U87 glioma tumor cells, mouse Lewis lung carcinoma cells, human BxPC-3 pancreatic carcinoma cells, and rat Dunning prostate carcinoma cells were incubated with a 1:1 precipitated mixture of retroviral supernatants of PT67 cells and RPMI medium 1640 containing 10% (vol/vol) FBS (Gemini Biological Products) for 72 h. Fresh medium was replenished at this time. Tumor cells were harvested with trypsin/EDTA and subcultured at a ratio of 1:15 into selective medium that contained 50 μg/ml of G418. The level of G418 was increased to 800 μg/ml in a step-wise manner. Clones expressing GFP were isolated with cloning cylinders (Bel-Art Products) by trypsin/EDTA and were amplified and transferred by conventional culture methods in the absence of selective agent.

RFP Gene Transformation. Dunning prostate cancer cells were cultured in RPMI medium 1640 (GIBCO) containing 10% (vol/vol) FBS (Gemini Biological Products). For expression-vector transfection, near-confluent Dunning cells were incubated with a precipitated mixture of Lipofectamine Plus (GIBCO) and saturating amounts of the RFP-expressing pLNCX$_2$-DsRed2 plasmid for 6 h before being replenished with fresh medium. Dunning cells were harvested with trypsin/EDTA 48 h after transfection and subcultured at a ratio of 1:15 into selective medium that contains 200 μg/ml of G418. Cells with stably integrated plasmids were selected by growing transiently transfected cells in 200 μg/ml of G418-containing medium. Clones were isolated with cloning cylinders (Bel-Art Products) by trypsin/EDTA and were amplified and transferred using conventional culture methods in the absence of selective agent.

s.c. Tumor Stock. To have growing tumor tissue stock for subsequent orthotopic implantation, six-week-old *nu/nu* female mice were injected s.c. with a single dose of 10^6–10^7 GFP- or RFP-expressing human or animal tumor cells. Cells were first harvested by trypsinization, washed three times with cold serum-containing medium, and then kept on ice. Cells were injected in the s.c. space of the flank of the animal in a total volume of 0.2–0.4 ml within 40 min of harvesting. The nude mice were killed to harvest tumor tissue 3 to 6 weeks after tumor cell injection for surgical orthotopic implantation (SOI) of tumor fragments (see below).

Brain Cancer Model. The parietal bone of the skull was exposed after an arc-shaped scalp incision. Twenty microliters containing 5 × 10^5 U87-GFP cells per mouse was injected into the right parietal lobe of the brain with a 1-ml 27G1/2 latex-free syringe (Becton Dickinson). The incision in the scalp was closed with a 7-0 surgical suture in one layer. The animals were kept under isoflurane anesthesia (Iso-Thesia, Vetus Animal Health, Burns Veterinary Supply, Rockville Center, NY) during surgery.

Lung Cancer Model. Tumor pieces (1 mm³) from s.c.-growing GFP-expressing Lewis lung carcinoma were implanted by SOI onto the left visceral pleura of nude mice (17). The mice were anesthetized by isoflurane inhalation. A small 1-cm transverse incision was made on the left-lateral chest of the nude mice through the fourth intercostal space. A small incision provided access to the pleural space and resulted in total lung collapse. Two tumor pieces were sewn together with an 8-0 nylon surgical suture (Look, Norwell,
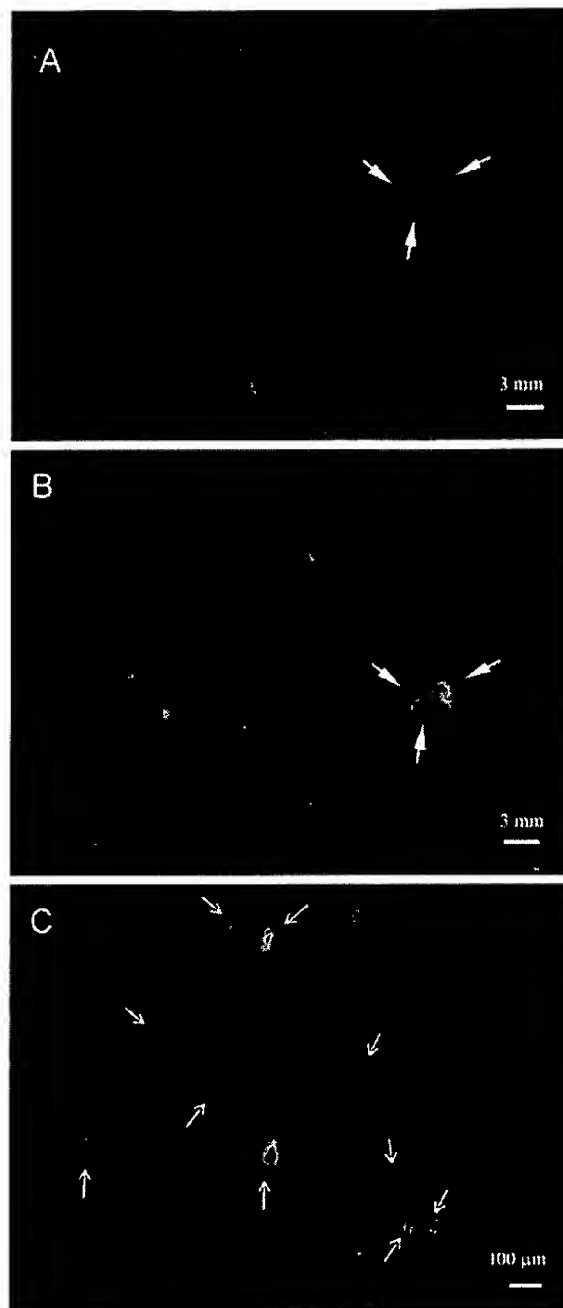
Fig. 1. Whole-body and direct view of macro and microfocal tumors in the brain. (*A*) Whole-body external imaging through the scalp of the bolus of U87-GFP tumor cells immediately after inoculation of tumor cells. The imaged area was ~2 mm in diameter. (Bar = 3 mm.) (*B*) The scalp-flap window enabled direct view of the bolus of U87-GFP tumor cells immediately after inoculation of tumor cells. The imaged area was ~2 mm in diameter. (Bar = 3 mm.) (*C*) Direct view of single tumor cells that separated from the bolus via the scalp-flap window. (Bar = 100 μm.) See *Materials and Methods* for details.

MA) and fixed by making one knot. The lung was taken up by forceps, and the tumor pieces were sewn into the lower part of the lung with one suture. The lung tissue then was returned into the chest cavity, and the chest muscles and skin were closed with a single layer of 6-0 silk sutures. The lung was reinflated by withdrawing air

Fig. 2. Whole-body and direct view of lung cancer. (*A*) Whole-body transcutaneous image of orthotopically growing Lewis lung tumor (arrows) in an intact live mouse on day 14 after SOI. (Bar = 3 mm.) (*B*) Direct view of orthotopically growing Lewis lung tumor via skin-flap window also imaged in *A* (arrows). The primary tumor (large arrows) and invading tumor cells (small arrows) are visible. Vessels also can be visualized in the primary tumor. (Bar = 3 mm.) (*C*) Direct view of microfoci (arrows) on the ipsilateral lung on day 5 after SOI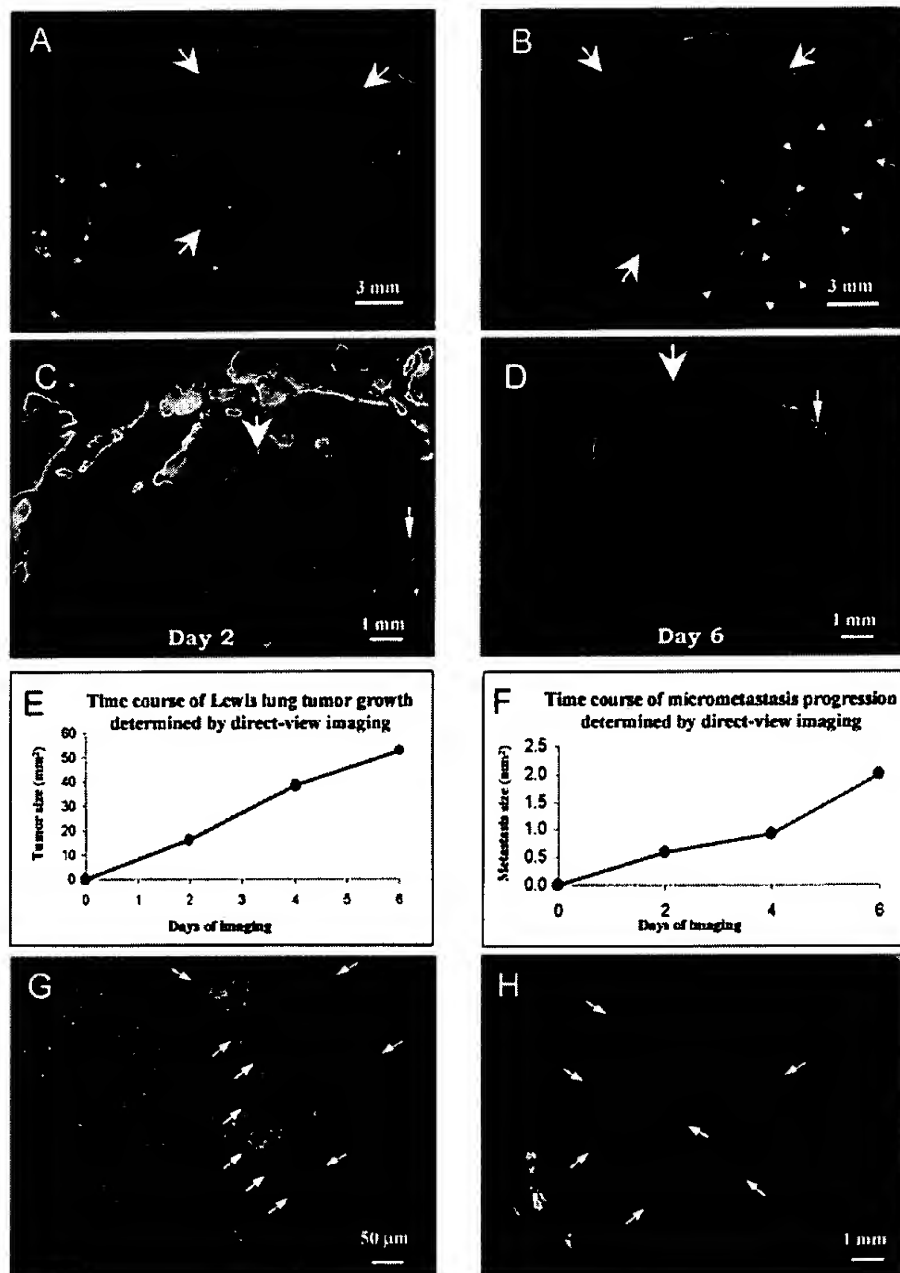. (Bar = 1 mm.) (*D*) Same as *C*, day 9 after SOI. (Bar = 1 mm.) (*E*) Growth curve of large tumor determined by direct-view images (*C* and *D*, indicated by thick arrows). (*F*) Growth curve of microfocal tumor determined by direct-view images (*C* and *D*, indicated by fine arrows). (*G*) Two three-cell microfoci in the ipsilateral lung at day 5 after SOI visualized by direct-view imaging. (Bar = 50 μm.) (*H*) Micrometastases (arrows) in the contralateral lung at day 7 after SOI visualized by direct-view imaging. (Bar = 1 mm.) See *Materials and Methods* for details.

from the chest cavity with a 23-gauge needle. All procedures of the operation described above were performed with a 7× dissection microscope (MZ6, Leica, Deerfield, IL).

Liver-Metastases Models. *Spontaneous liver-metastasis model.* Tumor fragments (1 mm³) from the liver-metastatic AC3488 tumor stably expressing GFP were implanted by SOI on the colon in nude mice. After proper exposure of the colon after a lower midline

abdominal incision, the serosa of the colon was removed and two pieces of 1 mm³ tumor fragments per mouse were implanted. An 8–0 surgical suture was used to penetrate these small tumor pieces and suture them on the wall of the colon, which then was returned to the abdominal cavity. The incision in the abdominal wall was closed with a 7–0 surgical suture in one layer (12). The animals were anesthetized during surgery with a ketamine-mixture of Ketaset and PromAce (both from Fort Dodge Laboratories, Fort Dodge,
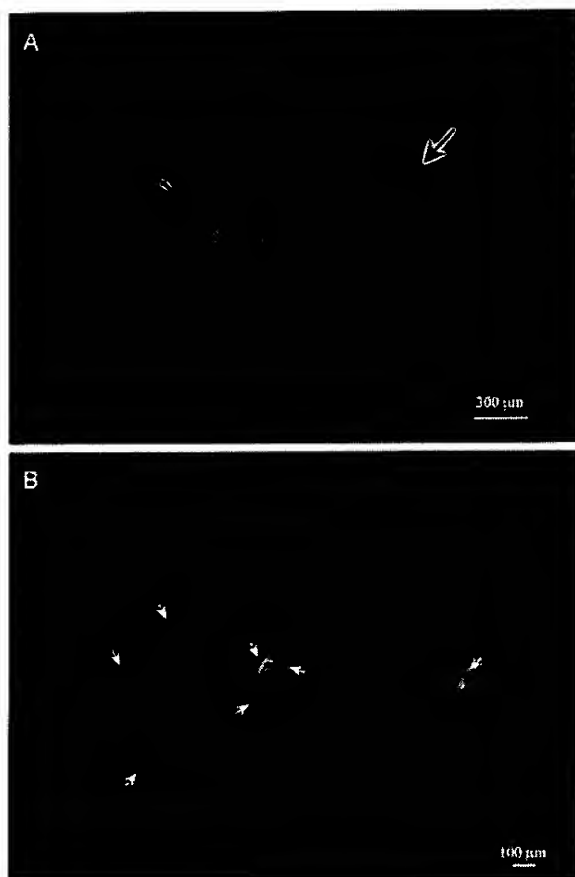
Fig. 3. Direct view of colon cancer liver micrometastasis. (*A*) Ventral direct view of micrometastasis of AC3488-GFP in the right lobe of the liver via a skin-flap window over the upper abdominal wall at day 7 after SOI. The smaller micrometastasis is ~150 μm in diameter (fine arrow), and the larger is ~300 μm in diameter (thick arrow). (*B*) Direct view of single cells (arrows) in right lobe of the liver after intraportal injection of 10^6 Colo-320 GFP cells. (Bar = 100 μm.) See *Materials and Methods* for details.

IA) and Xylazine HCl (American Animal Health, Wisner, NE). All procedures were performed with the 7× dissection microscope.

Experimental liver-metastasis model. Colo 320-GFP cells first were harvested by trypsinization and washed three times with cold serum-free medium. After proper exposure of the portal vein after an upper midline abdominal incision, 100 μl containing 10^6 GFP cells were injected in the portal vein with a 1-ml 39G1 latex-free syringe (Becton Dickinson). The puncture hole in the portal vein was pressed for about 10 s with a sterile cotton bar to prevent bleeding. The incision in the abdominal wall was closed with a 7–0 surgical suture in one layer. The animals were kept under the ketamine-mixture anesthesia during surgery. All procedures of the operation described above were performed with the 7× dissection microscope.

Pancreatic Cancer Model. The Bx-PC-3 human pancreatic tumor, expressing GFP and grown s.c. in nude mice, was resected aseptically. Necrotic tissues were cut away, and the remaining healthy tumor tissues were cut with scissors and minced into ~1-mm³ pieces in Hanks' balanced salt solution containing 100 units per ml of penicillin and 100 units per ml of streptomycin. Mice were anesthetized by the ketamine-mixture. The abdomen was sterilized with alcohol. An incision then was made through the left upper abdominal pararectal line and peritoneum. The

pancreas was carefully exposed, and three tumor pieces were transplanted on the middle of the pancreas with a 6–0 Dexon (Davis-Geck, Manati, Puerto Rico) surgical suture. The pancreas then was returned into the peritoneal cavity, and the abdominal wall and the skin were closed with 6–0 Dexon sutures. Animals were kept in a sterile environment. All procedures of the operation described above were performed with the 7× dissection microscope (18).

Prostate Cancer Model. Tumor tissue used for surgical orthotopic implantation was derived from a tumor growing s.c. after injection of Dunning prostate carcinoma-GFP or Dunning prostate carcinoma-RFP tumor cells in nude mice. Tissue from the periphery of the tumor was harvested in log phase, and necrotic tissue was carefully removed. The viable tissue then was cut into small cubes of 1 mm³ in standard tissue culture medium under sterile conditions. To minimize variation in subsequent tumor growth and metastasis, these tumor pieces were randomly mixed, and an equal amount was implanted in each mouse as described below. Mice were anaesthetized with the ketamine-mixture and positioned supinely. An arc-shaped skin flap was made right above the pubis symphysis to expose the prostate gland. The fascia surrounding the ventral portion of the prostate was carefully isolated, and the two ventral lateral lobes of the gland were exposed by a small incision using a pair of fine surgical scissors. One piece of Dunning GFP tissue was sutured into one lobe with an 8–0 nylon suture. Similarly, one piece of Dunning RFP tissue was sutured into the other lobe. The abdomen was closed with a 6–0 suture (19). All procedures of the operation were performed with the 7× dissection microscope.

Skin-Flap Windows. Tumor cells on the various internal organs were visualized through the skull or body wall through different skin-flap windows over the scalp, chest wall, upper abdomen, and lower abdomen. The animals were anesthetized with the ketamine-mixture. An arc-shaped incision was made in the skin, and s.c. connective tissue was separated to free the skin flap. The skin flap could be opened repeatedly to image tumor cells on the internal organs through the nearly transparent mouse body walls or skull and simply closed with an 6–0 suture. This procedure greatly reduced the scatter of fluorescent photons.

Fluorescence Imaging. A Leica fluorescence stereo microscope model LZ12 equipped with a mercury 50W lamp power supply was used (13–15, 20). To visualize both GFP and RFP fluorescence at the same time, excitation was produced through a D425/60 band pass filter, 470 DCXR dichroic mirror, and emitted fluorescence was collected through a long pass filter GG475 (Chroma Technology, Brattleboro, VT). Macroimaging was carried out in a light box (Lightools Research, Encinitas, CA). Fluorescence excitation of both GFP and RFP tumors was produced through an interference filter 440+/−20 nm using slit fiber optics for animal illumination. Fluorescence was observed through a 520-nm long pass filter. Images from the microscope and light box were captured on a Hamamatsu C5810 3-chip Cool-Color charge-coupled device camera (Hamamatsu Photonics, Hamamatsu City, Japan).

Images were processed for contrast and brightness and analyzed with the use of IMAGE PRO PLUS v.4.0 software (Media Cybernetics, Silver Spring, MD). High resolution images of 1024 × 724 pixels were captured directly on an IBM PC or continuously through video output on a high-resolution Sony VCR model SLV-R1000 (Sony, Tokyo; refs. 13–15).

All animal studies were conducted in accordance with the principles and procedures outlined in the National Institute of Health Guide for the Care and Use of Animals under assurance number A3873–1. Animals were kept in a barrier facility (12). Mice
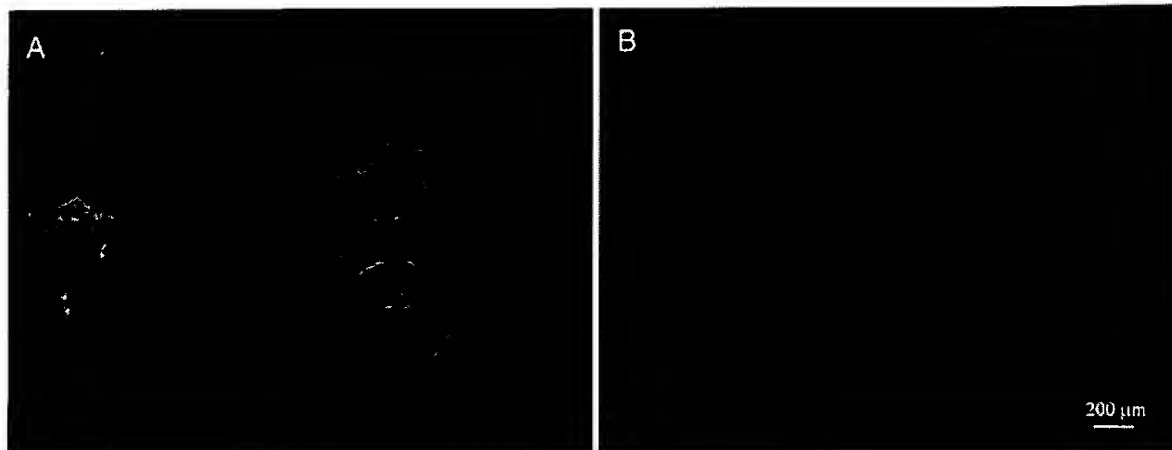
MEDICAL SCIENCES

Fig. 4. Direct view of microvessels of orthotopically growing pancreatic cancer. (A) The human Bx PC-3-GFP pancreatic tumor, microvessels, and metastasis to the spleen (fine arrows) were directly viewed via a skin-flap window over the abdominal wall of a nude mouse at day 58 after SOI. (B) Microvessels were directly viewed and highly resolved through the skin-flap window at higher magnification. (Bar = 200 μm.) See Materials and Methods for details.

were fed with autoclaved laboratory rodent diet Tecklad LM-485 (Western Research Products, Orange, CA).

Results

Optical Efficacy of the Skin Flap. Fig. 1 shows the direct view images of a fluorescent brain tumor. U87-GFP cells were inoculated on to the right parietal lobe of the brain. Fig. 1A shows the image obtained through the skull and scalp. Fig. 1B shows the same preparation but with the scalp open via a skin flap. Quantitative measurement of the fluorescence shows a twenty-fold increase in intensity when the intervening scalp tissue is removed. Fig. 1C shows an adjoining area in which single fluorescent cells are clearly resolved and which could not be imaged through the scalp.

Quantitative Imaging of Lung Cancer Microfoci. A powerful advantage conferred by the skin-flap technique is the opportunity to return to the same tumor and obtain quantitative measurements over time. The relatively modest invasiveness and low morbidity of the technique allows meaningful long-term measurements. An example of such an application is afforded by the data in Fig. 2. Lewis lung-GFP was implanted on the ipsilateral lung by SOI. The whole-body image through the skin (Fig. 2A) was compared with the external direct-view images obtained through a skin-flap window over the chest wall (Fig. 2B). The direct-view image allows fine details such as tumor microfoci and angiogenic vessels on the primary tumor to be imaged, which is not possible through the skin. Images of primary tumor and microfoci progression were recorded over a 6-day period (Fig. 2 C and D), and tumor growth curves were constructed (Fig. 2 E and F). The congruence between the data points and the expected growth curve suggests that the technique yields accurate quantitative measurements. Microfoci as small as one or two cells on the ipsilateral lung could be clearly imaged through the skin flap on day 5 (Fig. 2G). Similarly, microfoci seeded by metastasis from the ipsilateral lung were directly imaged by means of a skin-flap window over the contralateral lung on day 7 (Fig. 2H).

External Direct View Images of Liver Micrometastasis. AC3488-GFP, when implanted orthotopically in mice, mimics a common behavior of colon cancer, i.e., metastasis to liver. Metastatic microfoci were clearly visible by day 7 after implantation. Two metastatic lesions of 150 μm and 300 μm in diameter were externally imaged through a skin-flap window over the abdominal wall of the mouse (Fig. 3A). The 150 μm metastatic lesion

appeared to be formed by a single tumor microfocus, whereas the 300 μm lesion appeared to be separable into five separate colonies. The largest of these colonies, approximately 130 μm in diameter, was located in the center of the metastatic lesion. Closely associated were the other four smaller microfoci that ranged in size from 80 to 100 μm in diameter. These satellite microfoci may have arisen through separate metastatic events.

Another model of metastatic spread is the intraportal injection of cells of GFP-expressing colon cancer line, colo-320. Microfoci and even single cells were clearly visible in the liver when externally viewed through a skin-flap window (Fig. 3B).

Imaging Orthotopically Growing Pancreatic Cancer and Its Angiogenic Microvessels. One of the less obvious properties of the fluorescent orthotopic model is the ability to image induced angiogenic microvessels. This ability is made possible, in part, by the extensive angiogenic microvessel induction when tumors are implanted orthotopically. Also, the brilliance of the tumor fluorescence, facilitated by the reduced absorption through the skin-flap window, allows imaging of the induced microvessels as

Fig. 5. Dual-color direct view of Dunning-GFP and Dunning-RFP. Dual-color green and red fluorescent direct-view image of the Dunning-GFP tumor growing on the left lateral lobe and Dunning-RFP tumor growing on right lateral lobe of the mouse prostate via a lower abdominal wall skin-flap window one day after SOI. (Bar = 1 mm.) See Materials and Methods for details.

dark against a bright background. Fig. 4 shows the orthotopically growing BxPC 3-GFP human pancreatic tumor surrounded by its microvessels visible by their dark shadows.

Dual Color External Direct-View Imaging. The development of other fluorescence colors opens up many new possibilities of experimental design. The ability to image simultaneous green and red fluorescence was shown in Fig. 5. Dunning prostate RFP and GFP tumors were implanted on separate lobes of the nude mouse prostate. A ventral skin flap allowed external direct-view imaging of the GFP tumor growing on the left lateral lobe and the RFP labeled tumor on the right lateral lobe. Both tumors were less than 1 mm in diameter. Some of the potential of dual labeling is suggested in *Discussion* below.

Discussion

This report demonstrates a previously unobtainable sensitivity for external imaging of internal fluorescent tumors. The improvement in sensitivity afforded by the skin-flap window now permits imaging on essentially any internal organ of animals at least mouse-sized. In many cases, single cells can be visualized, thus allowing study of the earliest events in tumor establishment. Similarly, micrometastases of one to two cells were visualized on the lung and on the liver, allowing study of the earliest events in metastatic colonization. The quantitative time-course studies reported here illustrate the feasibility of obtaining precise growth data. These will permit accurate, rapid and economical assessment of new chemotherapeutic agents.

Angiogenesis has become one of the most intense areas of cancer research; studies attest to its crucial role in tumor growth and metastasis. Such data are central to understanding phenomena such as interference of the primary tumor of metastatic growth (21, 22) and, most importantly, the effect of chemotherapeutic agents on angiogenic vessels. However, obtaining precise data relating angiogenesis to tumor growth and metastasis is difficult as long as animal killing is required for each measurement. The fluorescent orthotopic metastatic model affords a relatively noninvasive method of visualizing angiogenic vessel

induction, in both space and time, for primary and metastatic tumors. Fig. 4 shows angiogenic vessels anastomosing the mouse pancreas. These vessels appear as dark shadows against the background of a brilliant fluorescent tumor. The microvessels were directly visualized through a skin-flap window on the peritoneal wall. The vessel development can be closely followed and quantified in real time, allowing precise answers to the relation of angiogenesis and cancer progression. The technique also affords rapid evaluation of drugs that may affect development of these vessels. Of special interest is the very low morbidity associated with the technique, which allows tumors to be followed for long periods of time.

An especially intriguing and currently little understood phenomenon is that of interference between disparate tumors. Apparently, the presence of a primary tumor can suppress the growth, angiogenesis, or metastasis of a second distinct tumor (21, 22). Research into tumor interference has largely used ectopic tumors such as s.c. xenografts or intraportally injected second tumor populations. The externally viewed, fluorescent orthotopic tumor model affords several new and powerful approaches to this question. Tumors can be placed into their natural environments and allowed to grow without surgical interference. Secondly, and most important, tumors can be labeled in two colors, which allows great flexibility in placement and timing of the tumors, which can then be followed for growth and angiogenesis for an unlimited period.

The external direct imaging by means of a skin-flap window of GFP- and RFP-labeled tumor cells affords extraordinarily high resolution, down to single cells, with a small investment in a light source and detection equipment. In contrast, luciferase based bioluminescence assays are two to three orders of magnitude less sensitive, they cannot detect single tumor cells, and they require both elaborate equipment and restraint of the experimental animal (23). The system described here is capable of multicolor fluorescence and affords a unique approach to the study of the critical factors in cancer progression.

1. Brown, E. B., Campbell, R. B., Tsuzuki, Y., Xu, L., Carmeliet, P., Fukumura, D. & Jain, R. K. (2001) *Nat. Med.* **7**, 864–868.
2. Ciancio, S. J., Coburn, M. & Hornsby, P. J. (2000) *J. Surg. Res.* **92**, 228–232.
3. Naumov, G. N., Wilson, S. M., MacDonald, I. C., Schmidt, E. E., Morris, V. L., Groom, A. C., Hoffman, R. M. & Chambers, A. F. (1999) *J. Cell Sci.* **112**, 1835–1842.
4. Chishima, T., Miyagi, Y., Wang, X., Yamaoka, H., Shimada, H., Moossa, A. R. & Hoffman, R. M. (1997) *Cancer Res.* **57**, 2042–2047.
5. Chishima, T., Miyagi, Y., Wang, X., Tan, Y., Shimada, H., Moossa, A. R. & Hoffman, R. M. (1997) *Anticancer Res.* **17**, 2377–2384.
6. Chishima, T., Miyagi, Y., Wang, X., Baranov, E., Tan, Y., Shimada, H., Moossa, A. R. & Hoffman, R. M. (1997) *Clin. Exp. Metastasis* **15**, 547–552.
7. Chishima, T., Miyagi, Y., Li, L., Tan, Y., Baranov, E., Yang, M., Shimada, H., Moossa, A. R. & Hoffman, R. M. (1997) *In Vitro Cell. Dev. Biol.* **33**, 745–747.
8. Chishima, T., Yang, M., Miyagi, Y., Li, L., Tan, Y., Baranov, E., Shimada, H., Moossa, A. R., Penman, S. & Hoffman, R. M. (1997) *Proc. Natl. Acad. Sci. USA* **94**, 11573–11576.
9. Yang, M., Hasegawa, S., Jiang, P., Wang, X., Tan, Y., Chishima, T., Shimada, H., Moossa, A. R. & Hoffman, R. M. (1998) *Cancer Res.* **58**, 4217–4221.
10. Yang, M., Jiang, P., Sun, F. X., Hasegawa, S., Baranov, E., Chishima, T., Shimada, H., Moossa, A. R. & Hoffman, R. M. (1999) *Cancer Res.* **59**, 781–786.
11. Yang, M., Jiang, P., An, Z., Baranov, E., Li, L., Hasegawa, S., Al-Tuwaijri, M., Chishima, T., Shimada, H., Moossa, A. R. & Hoffman, R. M. (1999) *Clin. Cancer Res.* **5**, 3549–3559.
12. Hoffman, R. M. (1999) *Invest. New Drugs* **17**, 343–359.
13. Yang, M., Baranov, E., Jiang, P., Sun, F.-X., Li, X.-M., Li, L., Hasegawa, S., Bouvet, M., Al-Tuwaijri, M., Chishima, T., *et al.* (2000) *Proc. Natl. Acad. Sci. USA* **97**, 1206–1211.
14. Yang, M., Baranov, E., Li, X.-M., Wang, J.-W., Jiang, P., Li, L., Moossa, A. R., Penman, S. & Hoffman, R. M. (2001) *Proc. Natl. Acad. Sci. USA* **98**, 2616–2621.
15. Yang, M., Baranov, E., Moossa, A. R., Penman, S. & Hoffman, R. M. (2000) *Proc. Natl. Acad. Sci. USA* **97**, 12278–12282.
16. Bevis, B. J. & Glick, B. S. (2002) *Nat. Biotechnol.* **20**, 83–87.
17. Rashidi, B., Yang, M., Jiang, P., Baranov, E., An, Z., Wang, X., Moossa, A. R. & Hoffman, R. M. (2000) *Clin. Exp. Metastasis* **18**, 57–60.
18. Bouvet, M., Yang, M., Nardin, S., Wang, X., Jiang, P., Baranov, E., Moossa, A. R. & Hoffman, R. M. (2000) *Clin. Exp. Metastasis* **18**, 213–218.
19. An, Z., Wang, X., Geller, J., Moossa, A. R. & Hoffman, R. M. (1998) *Prostate* **34**, 169–174.
20. Zhao, M., Yang, M., Baranov, E., Wang, X., Penman, S., Moossa, A. R. & Hoffman, R. M. (2001) *Proc. Natl. Acad. Sci. USA* **98**, 9814–9818.
21. Kisker, O., Onizuka, S., Banyard, J., Komiyama, T., Becker, C. M., Achilles, E. G., Barnes, C. M., O'Reilly, M. S., Folkman, J. & Pirie-Shepherd, S. R. (2001) *Cancer Res.* **61**, 7298–7304.
22. Guba, M., Cernaianu, G., Koehl, G., Geissler, E. K., Jauch, K. W., Anthuber, M., Falk, W. & Steinbauer, M. (2001) *Cancer Res.* **61**, 5575–5579.
23. Sweeney, T. J., Mailander, V., Tucker, A. A., Olomu, A. B., Zhang, W., Cao, Y., Negrin, R. S. & Contag, C. H. (1999) *Proc. Natl. Acad. Sci. USA* **96**, 12044–12049.

MEDICAL SCIENCES

Visualizing gene expression by whole-body fluorescence imaging

Meng Yang*, Eugene Baranov*, A. R. Moossa†, Sheldon Penman‡, and Robert M. Hoffman*†§

*AntiCancer, Inc., 7917 Ostrow Street, San Diego, CA 92111; †Department of Surgery, University of California, 200 West Arbor Drive, San Diego, CA 92103-8220; and ‡Department of Biology, Massachusetts Institute of Technology, 77 Massachusetts Avenue, Cambridge, MA 02139-4307

Transgene expression in intact animals now can be visualized by noninvasive techniques. However, the instruments and protocols developed so far have been formidable and expensive. We describe here a system for rapidly visualizing transgene expression in major organs of intact live mice that is simple, rapid, and eminently affordable. Green fluorescent protein (GFP) is expressed in the cells of brain, liver, pancreas, prostate, and bone, and its fluorescence is encoded in whole-body optical images. For low-magnification images, animals are illuminated atop a fluorescence light box and directly viewed with a thermoelectrically cooled color charge-coupled device camera. Higher-magnification images are made with the camera focused through an epi-fluorescence dissecting microscope. Both nude and normal mice were labeled by directly injecting 8×10^{10} plaque-forming units/ml of adenoviral GFP in 20–100 μl PBS and 10% glycerol into either the brain, liver, pancreas, prostate, or bone marrow. Within 5–8 h after adenoviral GFP injection, the fluorescence of the expressed GFP in brain and liver became visible, and whole-body images were recorded at video rates. The GFP fluorescence continued to increase for at least 12 h and remained detectable in liver for up to 4 months. The system's rapidity of image acquisition makes it capable of real-time recording. It requires neither exogenous contrast agents, radioactive substrates, nor long processing times. The method requires only that the expressed gene or promoter be fused or operatively linked to GFP. A comparatively modest investment allows the study of the therapeutic and diagnostic potential of suitably tagged genes in relatively opaque organisms.

green fluorescent protein fluorescence optical imaging | *in vivo* gene expression | real time

Gene expression, when studied in cultured animal cells, is largely concerned with scalar quantities such as the amount of gene product. Extending these studies to the expression of genes in whole animals adds spatial and temporal dimensions. The regional distribution of gene activity is of fundamental importance as is the timing of response to physiological signals. Making such measurements in animals has been extremely difficult. Every data point required killing and dissecting the experimental animal and measuring the distribution of a reporter gene. Following a time course in a single subject was, of course, impossible.

New techniques can visualize transgene expression noninvasively in intact animals and promise a veritable revolution in genetic and physiological studies (1–6). The methods are a significant extension of the century-old, noninvasive imaging of the internal tissues of intact animals. From Röntgen's x-rays to modern computed x-ray tomography and MRI, the static distribution of tissue mass has been visualized with ever-increasing resolution. Recent developments, such as MRI, have made possible visualizing dynamic processes. Now, noninvasive imaging has been extended to imaging the spatial distribution of transgene expression in living animals. Marker gene products have been visualized by MRI (2–3), by emitted gamma rays in micropositron emission tomography (4) and single-photon emission computed tomography (5), or by luciferin fluorescence (6).

Unfortunately, the procedures require complex and expensive apparatus as well as the administration either of contrast agents or substrates that are radioactive or fluorescent. Also, the signals are generally weak and so require long processing times, which limits detailed time-course measurements.

This report describes a simple, inexpensive optical system using GFP as a reporter. It can visualize gene expression in small mammals requiring only that the gene under study be coupled to GFP. The measurements are sufficiently rapid as to allow video recording for real-time measurements. The apparatus is sufficiently modest as to allow many laboratories to adopt the technique.

Materials and Methods

Animals. Four- to 6-week-old both male and female nude/nude, nude/+, and C57BL/6 mice were used. All animal studies were conducted in accordance with the principles and procedures outlined in the National Institutes of Health Guide for the Care and Use of Animals under assurance number A3873–1. Mice were fed with autoclaved laboratory rodent diet (Tecklad LM-485, Western Research Products, Orange, CA).

DNA Expression Vector. The adenoviral (vAd) vector AdCMV5GFPAE1/AE3 [vAd-green fluorescent protein (GFP)] (Quantum, Montreal, Canada) expresses enhanced GFP and the ampicillin resistance gene.

Delivery of vAd-GFP to Various Organs. *Brain.* The parietal bone of the skull was exposed after an upper midline scalp incision. Twenty microliters containing 8×10^{10} plaque-forming units (pfu)/ml vAd-GFP per mouse was injected in the brain by using a 1-ml 27G1/2 latex-free syringe (Becton Dickinson). The puncture hole in the skull was plugged with bone wax. The incision in the scalp was closed with a 7–0 surgical suture in one layer. The animals were kept under isofluorane anesthesia during surgery.

Liver. The portal vein was exposed after an upper midline abdominal incision. One-hundred microliters containing 8×10^{10} pfu/ml vAd-GFP per mouse was injected in the portal vein by using a 1-ml 30G½ latex-free syringe (Becton Dickinson). The puncture hole in the portal vein was pressed for about 10 sec with sterile cotton for hemostasis. The incision in the abdominal wall was closed with a 7–0 surgical suture in one layer. The animals were kept under Ketsel anesthesia during surgery. All procedures of the operation described above were performed with a ×7 magnification stereo microscope (Leica MZ12, Nussloch, Germany).

Pancreas. The pancreas was exposed after an upper midline abdominal incision. One-hundred microliters containing 8×10^{10} pfu/ml vAd-GFP per mouse was injected in the pancreas by using a 1-ml 30G½ latex-free syringe (Becton Dickinson). The puncture hole was pressed for about 10 sec with sterile cotton for hemostasis. The incision was closed with a 7–0 surgical suture in one layer. The animals were kept under Ketsel anesthesia during surgery. All procedures of the operation described above were performed with a ×7 magnification stereo microscope.

Prostate. The bladder and prostate were exposed after a lower midline abdominal incision. Thirty microliters containing 8×10^{10} pfu/ml vAd-GFP per mouse was injected in the prostate by using a 1-ml 30G½ latex-free syringe (Becton Dickinson). The puncture hole in the prostate was pressed for about 10 sec with sterile cotton for hemostasis. The incision in the abdominal wall was closed with a 6–0 surgical suture in one layer. The animals were kept under isoflurane anesthesia during surgery. All procedures of the operation described above were performed with a ×7 magnification stereo microscope.

Bone Marrow. For bone marrow injection, animals were anesthetized by inhalation of isofluorane. The skin on the hind leg was opened with a 1-cm incision to expose the tibia. A 27-gauge needle with latex-free syringe (Becton Dickinson) then was inserted in the bone marrow cavity. A total volume of 20 μl (8×10^{10} pfu/ml) vAd-GFP per mouse was injected into the bone marrow cavity. The puncture hole in the bone was plugged with bone wax, and the incision was closed with a 6–0 surgical suture.

External Imaging of Transgene Expression. A Leica fluorescence stereo microscope, model LZ12, equipped with a 50-W mercury lamp, was used for high-magnification imaging. Selective excitation of GFP was produced through a D425/60 band-pass filter and 470 DCXR dichroic mirror. Emitted fluorescence was collected through a long-pass filter GG475 (Chroma Technology, Brattleboro, VT) on a Hamamatsu C5810 3-chip cooled color charge-coupled device camera (Hamamatsu Photonics Systems, Bridgewater, NJ). Images were processed for contrast and brightness and analyzed with the use of IMAGE PRO PLUS 3.1 software (Media Cybernetics, Silver Springs, MD). Images of $1,024 \times 724$ pixels were captured directly on an IBM PC or continuously through video output on a high-resolution Sony VCR model SLV-R1000 (Sony, Tokyo). Imaging at lower magnification that visualized the entire animal was carried out in a light box illuminated by blue light fiber optics (Lightools Research, Encinitas, CA) and imaged by using the thermoelectrically cooled color charge-coupled device camera, as described above.

Measuring the Intensity of GFP Expression. Estimating the intensity of GFP fluorescence is complicated by variations in the exciting illumination with time and across the imaging area. These factors are corrected for by using the intrinsic red fluorescence of mouse skin as a base line to correct the increase over intrinsic green fluorescence caused by GFP. This can be done because there is relatively little red luminance in the GFP radiance. Consequently, the green fluorescence was calculated relatively to red based on red and green channel composition in the skin image. A ratio (γ) of green to red channels was determined for each pixel in the image of skin without and with GFP. Values of γ for mouse skin throughout the image in the absence of GFP were fairly constant, varying between 0.7 and 1.0. The contribution of GFP fluorescence from within the animal increased the green component relative to red, which was reflected in higher γ values. The total amount of GFP fluorescence was approximated by multiplying the number of pixels in which value γ was higher than 1 times the γ value of each pixel. Such a product roughly corresponds to the integral GFP fluorescence [I'_{GFP}] above the maximum value of γ for skin without GFP. The number of pixels
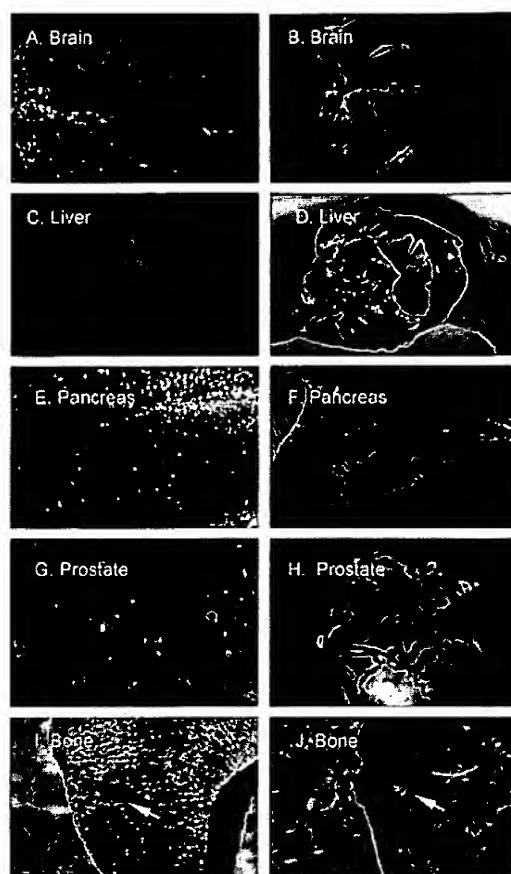

Fig. 1. External and internal images of vAd-GFP gene expression in various organs. External fluorescent whole-body images were compared with direct images of vAd-GFP gene expression in various organs. Series of external fluorescence images of vAd-GFP gene expression in brain, liver, pancreas, prostate, and tibia. (*A, C, E, G,* and *I*) compared with corresponding images of the exposed organs (*B, D, F, H,* and *J*). See *Materials and Methods* for vector delivery and imaging details.

in mouse skin images with γ value > 1.0 without GFP was less than 0.02% and increased with GFP expression. The value of [I'_{GFP}] is presented as a function of time after virus injection in Figs. 3 and 5 for the brain and liver.

Results

Fluorescence of vAd-GFP Gene Expression in Labeled Mouse Organs. The crucial test of external imaging is its ability to represent the internal distribution of gene activity. Fig. 1 compares external images of vAd-GFP fluorescence from labeled mouse organs in live, intact animals to the fluorescence of the organs viewed directly after death and dissection. The fluorescence maps the region of gene expression in the brain (Fig. 1 *A* and *B*), liver (Fig. 1 *C* and *D*), pancreas (Fig. 1 *E* and *F*), prostate (Fig. 1 *G* and *H*), and bone (Fig. 1 *I* and *J*). The images made externally to the animal appear very similar to those of the exposed organs, reproducing much of the detailed structure of the direct image.

Real-Time Quantitative Whole-Body Imaging of vAd-GFP Gene Expression. Another important advantage of the GFP fluorescence assay for gene expression is its extremely rapid data acquisition. Under the conditions used here, images could be obtained at video rates, i.e., with exposure times in the order of 1/30 sec. The fluorescence from vAd-GFP gene expression in the brain of a single animal was visible within 6 h after local delivery of the
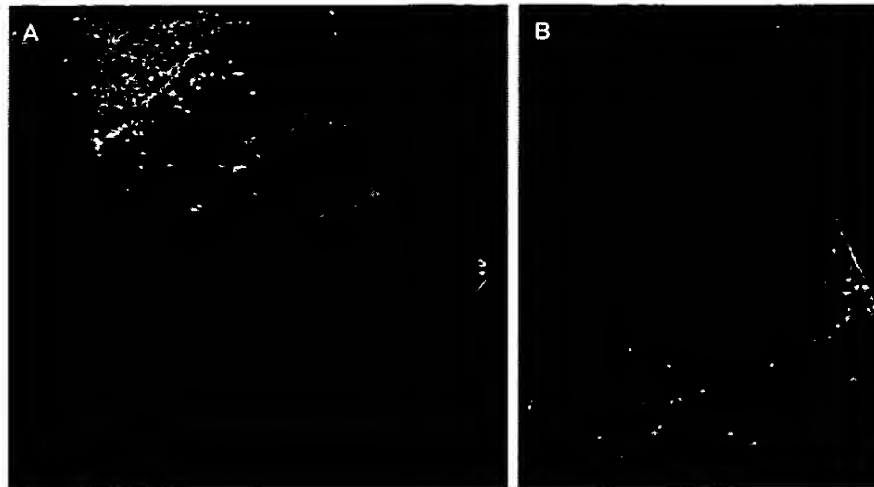
Fig. 2. External whole-body image of vAd-GFP gene expression in the brain. An external image of vAd-GFP gene expression in the brain acquired from a nude mouse in the light box 24 h after gene delivery. Clear image of transgene expression in the brain can be visualized through the scalp and skull. See *Materials and Methods* for imaging.

vAd-GFP gene in a nude mouse (Fig. 2). The fluorescence intensity was monitored by real-time video recording and measured as described in *Materials and Methods*. The data are shown in Fig. 3. Liver fluorescence first became detectable at about 7 h after the injection of vAd-GFP into the tail vein. The time course of observed intensity measured from a video recording is plotted in Fig. 4.

Whole-Body, External Images of vAd-GFP Gene Expression in Liver.
The simplest and most rapid method of observing whole-body fluorescent images of vAd-GFP gene expression is shown in Fig. 5. Images showing fluorescence emanating from the liver were acquired from a mouse freely moving in a light box (Fig. 5). This inexpensive system suggests the feasibility of high-throughput screening of agents that affect specific gene expression.

Imaging Sensitivity. GFP transgene expression in various organs and tissues was considered to be externally measurable if the

average fluorescence of the GFP-expressing organs was at least 20% above the average fluorescence of the surrounding skin. The fluorescence intensity at maximal level of GFP expression in the liver exceeded more than 100 times backdorsal and abdominal skin fluorescence. The intensity of GFP fluorescence of vAd-GFP expression in the mouse liver at a depth of 0.8 mm under the skin was ≈25% of that of the exposed organ.

Discussion

The enormous potential of visualizing gene expression in intact living animals has motivated development of several quite ingenious techniques. MRI is a nonoptical method that has been adapted for imaging a transgene product that perturbs the magnetic field. MRI can image intact, opaque organisms in three dimensions with resolution at approximately 50 μM^3 (2). However, the low sensitivity entails long imaging times and consequently slow data acquisition. Most importantly, the method depends on administering a systemic contrast agent selectively
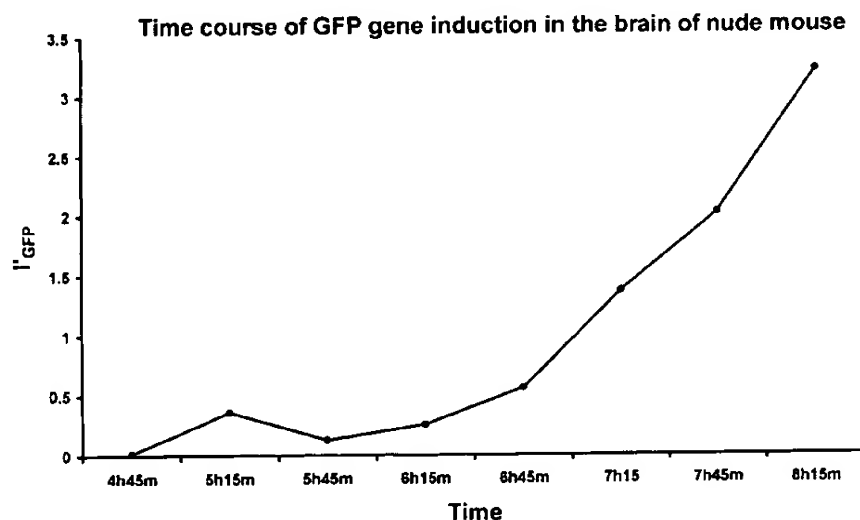

Fig. 3. Time course of GFP gene induction in the brain of a nude mouse. [I'$_{GFP}$] (see *Materials and Methods*) from a series of whole-body images determined that vAd-GFP expression could be first visualized by 5 h, 15 min after local introduction of vAd-GFP gene in a nude mouse. Increases in expression could be visualized in 30-min intervals.

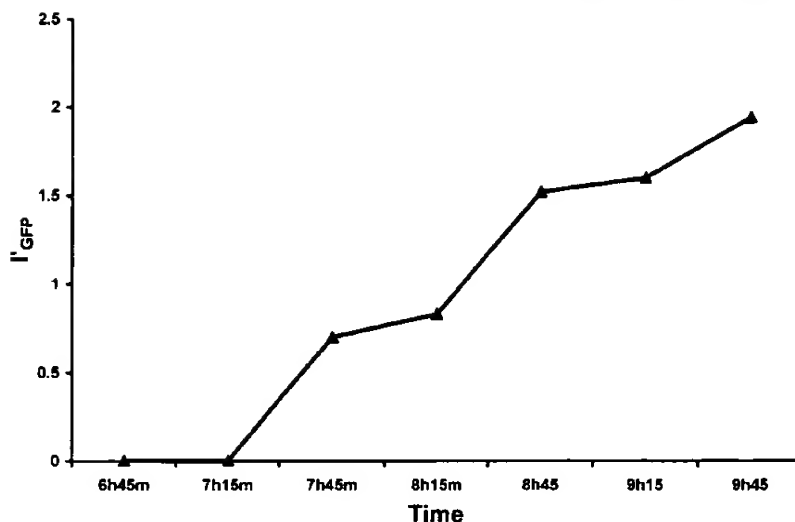## Time course of GFP gene induction in the liver of nude mouse

Fig. 4. Time-course GFP gene induction in the liver of a nude mouse. vAd-GFP expression [I'GFP] (see *Materials and Methods*) could be first visualized in the liver by 7 h, 45 min after introduction of vAd-GFP gene in a nude mouse. Increases in expression could be visualized in 30-min intervals.

activated by the gene product (2, 3), a requirement that restricts the type of gene product that can be imaged.

Another approach to noninvasive imaging uses gamma emission from the target region. The techniques, such as micropositron emission tomography and single-photon emission computed tomography (4, 5), require radio-labeled substrates to be localized to some degree by an enzymatic activity of the expressed transgene product. This demanding requirement and the sophisticated equipment for detection and image formation would seem to limit possible applications.

Although animal tissue is rather opaque, optical methods nevertheless offer advantages for noninvasive imaging of transgene expression. Both MRI and radiographic techniques require the expressed gene product to modify either a magnetic field or a diffusion gradient. In contrast, the method described here uses the gene product itself as a source of visible

Fig. 5. External whole-body image of vAd-GFP gene expression in the liver. An external image of vAd-GFP gene expression acquired from a nude mouse in the light box 72 h after gene delivery. Lateral, whole-body image of transgene expression in the liver can be clearly visualized through the abdominal wall.

radiation. This radiance is recorded and processed by essentially garden-variety optical instrumentation and image processing. A previous report (6) used the luciferase gene as a reporter for whole-body optical imaging of gene expression. The technique is limited by the need to anesthetize the animals and inject the luciferase substrate. The sensitivity appears inherently low requiring long-term photon acquisition and integration to produce images of immobilized animals (6). Such limits preclude real-time studies and high-throughput *in vivo* screening of gene expression.

Optical imaging of GFP to map regions of gene expression dispenses with exogenous contrast agents and substrates and offers specificity, sensitivity, simplicity, and real-time recording capability. We previously showed whole-body fluorescence imaging of tumors expressing GFP in living intact animals (7). Other studies have demonstrated superficial imaging of GFP transgene expression in specialized sites such as the skin (8), retina (9), and testis (10). These are unusual in having relatively little tissue between the chromophore and external detector. In the present study, using vAd-GFP as the reporter gene and illumination with a simple light box or fluorescence dissecting microscope, we demonstrate noninvasive, whole-body, real-time fluorescence optical imaging of transgene expression in the major organs of mice including brain, liver, pancreas, prostate, and bone.

vAd-GFP delivered to various organs was induced rapidly and was stable over long time periods, allowing real-time quantitative imaging of transgene expression. These results indicate that gene induction and other kinetic studies can be visualized by whole-body imaging. The high intensity of GFP fluorescence makes transgene expression externally observable from internal organs including brain, liver, pancreas, prostate, and bone (Fig. 1) and presumably in many other organs such as breast, lymph nodes, etc. No contrast agents, radioactive sources, or enzyme substrates need be administered to the animals; only blue light illumination is necessary. The images can be acquired in real time because of the strong GFP signal. The technology reported here can be applied to any gene or promoter fused or operatively linked to GFP in any organ.

We chose vAd-GFP as a vector, because it can transduce many normal tissues efficiently. It was found that vAd-GFP gene is stably expressed in the brain and liver at least for a number of months. Similar studies could be performed in transgenic animals in which GFP or other fluorescent proteins were fused or operatively linked to any gene or promoter.

It is worth noting that the sensitivity and specificity of the method can be greatly increased. Future use of tissue-specific promoters in combination with the ultra-fast lasers (11), dual photon imaging (12), and ballistic photon imaging (13, 14) should offer large gains in specificity, sensitivity, increased depth of detection, and spatial resolution. Visualizing in three dimensions would be possible by using tomographic techniques. This technology provides a powerful *in vivo* tool for noninvasive, real-time visualization of gene expression in living animals. It should facilitate the identification of gene function and development of gene diagnostics and therapeutics.

1. Herschman, H. R., MacLaren, D. C., Iyer, M., Namavari, M., Bobinski, K., Green, L. A., Wu, L., Berk, A. J., Toyokuni, T., Barrio, J. R., *et al.* (2000) *J. Neurosci. Res.* **59**, 699–705.
2. Louie, A. Y., Huber, M. M., Ahrens, E. T., Rothbacher, U., Moats, R., Jacobs, R. E., Fraser, S. E. & Meade, T. J. (2000) *Nat. Biotechnol.* **18**, 321–325.
3. Weissleder, R., Moore, A., Mahmood, U., Bhorade, R., Benveniste, H., Chiocca, E. A. & Basilion, J. P. (2000) *Nat. Med.* **6**, 351–355.
4. Gambhir, S. S., Barrio, J. R., Phelps, M. E., Iyer, M., Namavari, M., Satyamurthy, N., Wu, L., Green, L. A., Bauer, E., MacLaren, D. C., *et al.* (1999) *Proc. Natl. Acad. Sci. USA* **96**, 2333–2338.
5. Tjuvajev, J. G., Finn, R., Watanabe, K., Joshi, R., Oku, T., Kennedy, J., Beattie, B., Koutcher, J., Larson, S. & Blasberg, R. G. (1996) *Cancer Res.* **56**, 4087–4095.
6. Contag, P. R., Olomu, I. N., Stevenson, D. K. & Contag, C. H. (1998) *Nat. Med.* **4**, 245–247.
7. Yang, M., Baranov, E., Jiang, P., Sun, F.-X., Li, X.-M., Li, L., Hasegawa, S., Bouvet, M., Al-Tuwaijri, M., Chishima, T., *et al.* (2000) *Proc. Natl. Acad. Sci. USA* **97**, 1206–1211.
8. Kishimoto, J., Ehama, R., Ge, Y., Kobayashi, T., Nishiyama, T., Detmar, M. & Burgeson, R. E. (2000) *Am. J. Pathol.* **157**, 103–110.
9. Bennett, J., Duan, D., Engelhardt, J. F. & Maguire, A. M. (1997) *Invest. Ophthalmol. Visual Sci.* **38**, 2857–2863.
10. Yamazaki, Y., Yagi, T., Ozaki, T. & Imoto, K. (2000) *J. Exp. Zool.* **286**, 212–218.
11. Alfano, R. R., Demos, S. G. & Gayen, S. K. (1997) *Ann. N.Y. Acad. Sci.* **820**, 248–270.
12. Masters, B. R., So, P. T. & Gratton, E. (1998) *Ann. N.Y. Acad. Sci.* **838**, 58–67.
13. Wu, J., Perelman, L., Dasari, R. & Feld, M. (1997) *Proc. Natl. Acad. Sci. USA* **94**, 8783–8788.
14. Alfano, R. R., Demos, S. G., Galland, P., Gayen, S. K., Guo, Y., Ho, P. P., Liang, X., Liu, F., Wang, L., Wang, Q. Z. & Wang, W. B. (1998) *Ann. N.Y. Acad. Sci.* **838**, 14–28.

Spatial–temporal imaging of bacterial infection and antibiotic response in intact animals

Ming Zhao*, Meng Yang*, Eugene Baranov*, Xiaoen Wang*, Sheldon Penman†, A. R. Moossa‡, and Robert M. Hoffman*‡§

*AntiCancer, Inc., 7917 Ostrow Street, San Diego, CA 92111; †Department of Biology, Massachusetts Institute of Technology, 77 Massachusetts Avenue, Cambridge, MA 02139-4307; and ‡Department of Surgery, University of California, 200 West Arbor Drive, San Diego, CA 92103

Contributed by Sheldon Penman, June 1, 2001

We describe imaging the luminance of green fluorescent protein (GFP)-expressing bacteria from outside intact infected animals. This simple, nonintrusive technique can show in great detail the spatial–temporal behavior of the infectious process. The bacteria, expressing the GFP, are sufficiently bright as to be clearly visible from outside the infected animal and recorded with simple equipment. Introduced bacteria were observed in several mouse organs including the peritoneal cavity, stomach, small intestine, and colon. Instantaneous real-time images of the infectious process were acquired by using a color charge-coupled device video camera by simply illuminating mice at 490 nm. Most techniques for imaging the interior of intact animals may require the administration of exogenous substrates, anesthesia, or contrasting substances and require very long data collection times. In contrast, the whole-body fluorescence imaging described here is fast and requires no extraneous agents. The progress of Escherichia coli-GFP through the mouse gastrointestinal tract after gavage was followed in real-time by whole-body imaging. Bacteria, seen first in the stomach, migrated into the small intestine and subsequently into the colon, an observation confirmed by intravital direct imaging. An i.p. infection was established by i.p. injection of E. coli-GFP. The development of infection over 6 h and its regression after kanamycin treatment were visualized by whole-body imaging. This imaging technology affords a powerful approach to visualizing the infection process, determining the tissue specificity of infection, and the spatial migration of the infectious agents.

green fluorescent protein | external optical imaging | Escherichia coli | antibiotic response | mice

Many biological research techniques depend on detecting uniquely distinguishable cells, e.g., cells exhibiting unique or aberrant morphologies. Far greater sensitivity is achieved by adding exogenous markers, especially those that are optically visible. The techniques of early embryologists marking developmental pathways with India ink injections have evolved into modern methods that include genetically transducing cells with reporters such as dye-activating enzymes. However, such methods still could not detect small, rare targets and usually could not be visualized in living systems. A qualitative advance in sensitivity is afforded by the new class of cell marking reagents exemplified by green fluorescent protein (GFP) and its derivatives. Genetically based, these can be permanent and nontoxic, and are very strongly fluorescent. Most importantly, because their presence seems to have little effect on the marked cell, observations in living tissue are now possible. We show here that GFP enables previously impossible, noninvasive tracking of bodily disease agents in space and time.

GFP has been used as a reporter gene for numerous biological processes (1). Its freedom from required substrates or cofactors allows it to be expressed and visualized in living cells with no apparent biological damage (1). The extreme sensitivity afforded by GFP-expressing cells has been a powerful tool in studying metastasis. We developed the necessary GFP-expressing human cancer cells and showed that these gave rise to metastases that

can be visualized at the single-cell level in freshly dissected tissue or in intravital examination (1, 2). Studies with GFP-expressing cancer cells of the lung (3, 4), ovary (2), prostate (5), and pancreas (6) have revealed the earliest metastatic events and afford rapid, accurate determination of the metastatic potential of these tumor types.

In the course of experiments with implanted GFP-labeled tumors, we noted that the fluorescence was sufficiently strong as to be visible from outside the animal. This led to a simple but effective technique for imaging whole, intact mice so that internal GFP-fluorescent tumors were clearly visible. These whole-body images afforded unique, real-time views of tumor growth and metastasis of GFP-expressing cancer cells (7). The whole-body imaging technique requires only simple (490-nm from a xenon or mercury lamp) illumination of mice bearing GFP-expressing tumors and image capture with a charge-coupled device color video camera (7). Tumor growth and metastasis were imaged in the colon, brain, liver, skeleton, and other organs (7). The nonintrusiveness of the technique is worth noting. In contrast to other imaging techniques, no substrate injection, radioactivity, contrast agent, or anesthesia is required (8). Also, whereas most imaging technologies require lengthy exposures of immobilized animals (8–18), the whole-body fluorescence images of GFP-expressing tumors are acquired essentially instantaneously (7).

The relative ease and efficacy with which implanted fluorescent tumors can be imaged externally suggested extending the technique to other foreign agents such as infecting bacteria. Escherichia coli was transfected with a high-expression plasmid containing the GFP gene. The GFP-expressing E. coli (E. coli-GFP) was administered to mice by various routes and the fate of the bacteria was readily visualized in real time by whole-body imaging. This technique makes possible the rapid in vivo screening and evaluation of antibiotics, the role of virulence genes, and other determinants of infection, pathology, and immunity.

Materials and Methods

GFP Vector. A variant of the Renilla mulleri (RMV)-GFP (M.Z., M. Xu., and R.M.H., unpublished data) was used. RMV-GFP was cloned into the BamHI and NotI sites of the pUC19 derivative pPD16.43 (CLONTECH) with GFP expressed from the lac promoter. The vector was termed pRMV-GFP.

E. coli-GFP. pRMV-GFP was transfected into E. coli JM 109 competent cells (Stratagene) by standard methods. Transformed E. coli JM109 were selected by ampicillin resistance on agar plates. High-expression E. coli-GFP clones were selected by fluorescence microscopy.
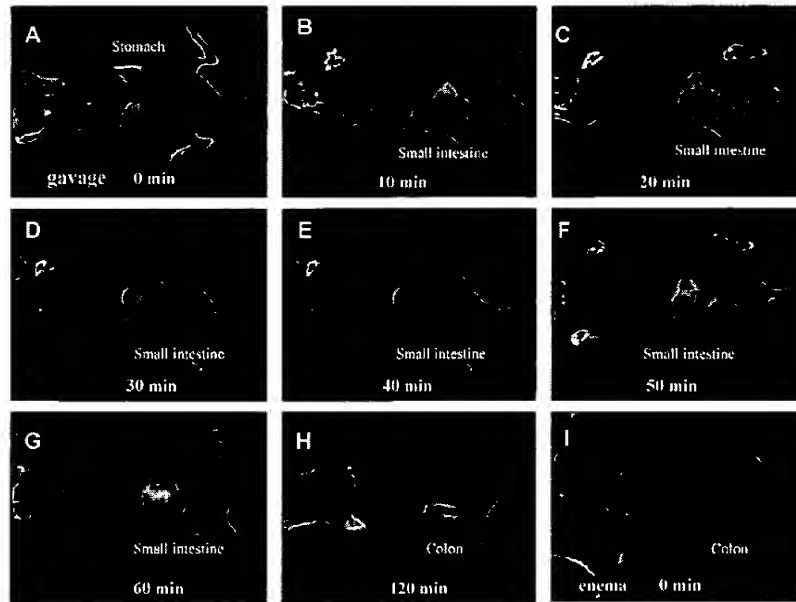
Fig. 1. Whole-body imaging of *E. coli*-GFP infection in various organs. (*A*) *E. coli*-GFP infection in the stomach immediately after gavage of 10^{11} *E. coli*-GFP. (*B*) *E. coli*-GFP infection in the small intestine 10 min after gavage. (*C*) *E. coli*-GFP infection in the small intestine 20 min after gavage. (*D*) *E. coli*-GFP infection in the small intestine 30 min after gavage. (*E*) *E. coli*-GFP infection in the small intestine 40 min after gavage. (*F*) *E. coli*-GFP infection in the small intestine 50 min after gavage. (*G*) *E. coli*-GFP infection in the small intestine 60 min after gavage. (*H*) *E. coli*-GFP infection in the colon 120 min after gavage. (*I*) *E. coli*-GFP infection in the colon immediately after enema of 10^{11} *E. coli*-GFP.

Mice. *nu/nu*/CD-1 mice (4-week-old females) were used for infection studies. All animal studies were conducted in accordance with the principles and procedures outlined in the National Institutes of Health Guide for the Care and Use of Laboratory Animals under assurance number A3873-1.

E. coli-GFP Infection of Stomach, Small Intestine, and Colon in Mice. Mice were gavaged with 1 ml of an *E. coli*-GFP suspension (1 × 10^{11} cells per ml) with a 20-gauge barrel tip feeding needle (Fine Science Tools, Belmont, CA) and latex-free syringe (Becton Dickinson).

E. coli-GFP Direct Colon Infection. A solution (1 ml) containing 1 × 10^{11} *E. coli*-GFP per mouse was administered into the colon by enema using a 20-gauge barrel-tip feeding needle (Fine Science Tools) and latex-free syringe (Becton Dickinson).

E. coli-GFP Peritoneal Infection. The mice in each group were given an i.p injection of 10^9 to 10^{10} *E. coli*-GFP. A 1-ml 29G1 latex-free syringe (Becton Dickinson) was used.

Antibiotic Treatment. *E. coli*-GFP-infected mice were given an i.p. injection of 2 mg of kanamycin (Fisher Scientific) in 100 μl. Mice in the control group were given an i.p. injection of 100 μl of PBS instead of antibiotic.

Whole-Body and Intravital Imaging of E. coli-GFP (7). Imaging was carried out in a light box illuminated by blue light fiber optics (Lightools Research, Encinitas, CA). Images were captured by using a Hamamatsu C5810 three-chip cooled color charge-coupled device camera (Hamamatsu Photonics Systems, Bridgewater, NJ). Images of 1024 × 724 pixels were captured either directly on an IBM PC or continuously through video output on a high-resolution Sony VCR (model SLV-R1000; Sony, Tokyo). Images were processed for contrast and brightness and analyzed with the use of IMAGE PRO PLUS 3.1 software (Media Cybernetics, Silver Spring, MD).

Results

External Whole-Body Imaging of Gastrointestinal Infection with E. coli-GFP. *E. coli*-GFP introduced to the mouse gastrointestinal tract by gavage became visible in the stomach in whole-body
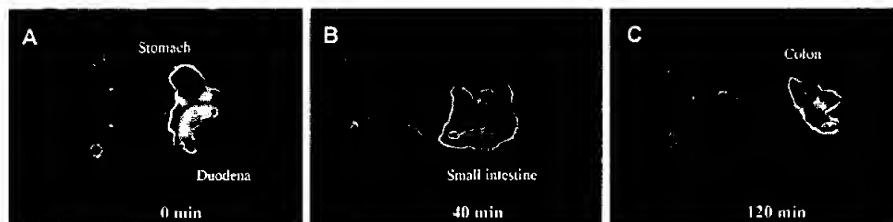
Fig. 2. Intravital imaging of *E. coli*-GFP infection in the stomach, small intestine, and colon after gavage. (*A*) *E. coli*-GFP infection in the stomach and the duodenum immediately after gavage of 10^{11} *E. coli*-GFP. (*B*) *E. coli*-GFP infection in the small intestine 40 min after gavage. (*C*) *E. coli*-GFP infection in the colon 120 min after gavage.

small intestine appeared to peak at 40 min after gavage (Fig. 1*E*) and disappeared by 120 min (Fig. 1*H*). After 120 min, *E. coli*-GFP appeared in the colon (Fig. 1*H*). Direct colonic inoculation with *E. coli*-GFP was also visualized after intra-anal enema delivery (Fig. 1*I*).

Comparison of Whole-Body and Intravital Imaging of Gastrointestinal *E. coli*-GFP. At appropriate times after gavage, the abdominal cavity was opened and intravital images made of the *E. coli*-GFP fluorescence. The stomach (Fig. 2*A*), small intestine (Fig. 2*B*), and colon (Fig. 2*C*) were brightly fluorescent with *E. coli*-GFP as seen by intravital imaging. Multiple gavage with *E. coli*-GFP allowed simultaneous inoculation of the stomach, small intestine, and colon, which were imaged by whole-body (Fig. 3*A*) and intravital techniques (Fig. 3*B*). Comparison of whole-body and intravital images of *E. coli*-GFP in the stomach, small intestine, and colon showed a high degree of correspondence (Figs. 1–3).

External Whole-Body Imaging of an i.p. Infection and Its Response to an Antibiotic. An authentic infection was established in a mouse by i.p. inoculation with *E. coli*-GFP. Immediately after injection, the fluorescent bacteria were seen localized around the injection site by external whole-body imaging (Fig. 4 *A* and *C*). Six hours later, the *E. coli*-GFP were seen to spread throughout the peritoneum (Fig. 4*B*), coinciding with the death of the animal. Intravital imaging of *E. coli*-GFP in the open peritoneal cavity at 6 h (Fig. 5) showed a bacterial distribution similar to that seen by external whole-body imaging. Intraperitoneally infected animals were next treated with kanamycin after inoculation. Whole-body imaging showed a marked reduction of the bacterial population over the next 6 h (Fig. 4 *C* and *D*). Previous attempts to image infection in intact animals used bacteria expressing luciferase (14), which, because of the much lower luminosity, is a far more difficult and intrusive procedure.

Discussion

The advent of GFP as a fluorescent cell marker has brought unprecedented sensitivity and discrimination to the study of cell behavior. These qualities were uniquely applicable to our ongoing studies of tumor metastases. GFP-labeled tumors were
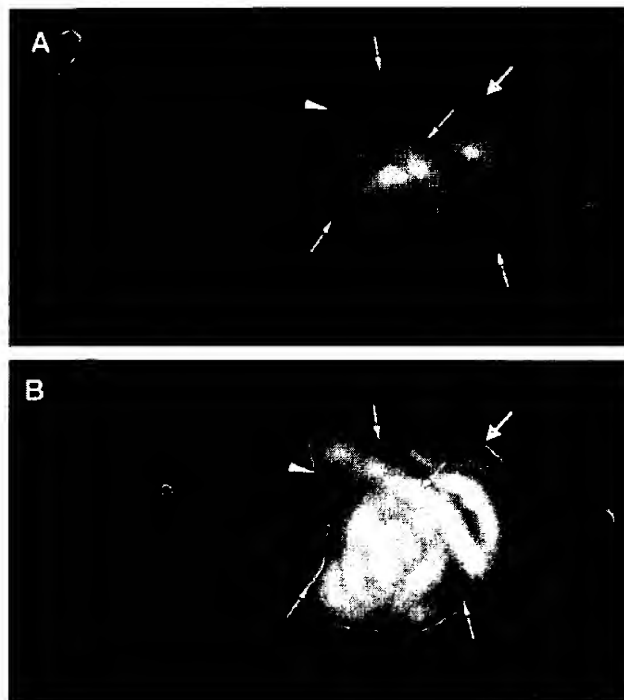
Fig. 3. Whole-body and intravital imaging of *E. coli*-GFP infection in the stomach, small intestine, and colon after gavage. (*A*) Whole-body image of *E. coli*-GFP infection in the stomach (arrowhead), the small intestine (fine arrows), and the colon (thick arrow) after multiple gavage of aliquots 3 × 10¹¹ *E. coli*-GFP. (*B*) Intravital image of *E. coli*-GFP infection in the stomach (arrowhead), the small intestine (fine arrows), and the colon (thick arrow) after multiple gavage of aliquots of 3 × 10¹¹ *E. coli*-GFP.

images almost immediately (Fig. 1*A*). The stomach emptied within 10 min after gavage and the *E. coli*-GFP next appeared in the small intestine (Fig. 1 *B–G*). The bacterial population in the

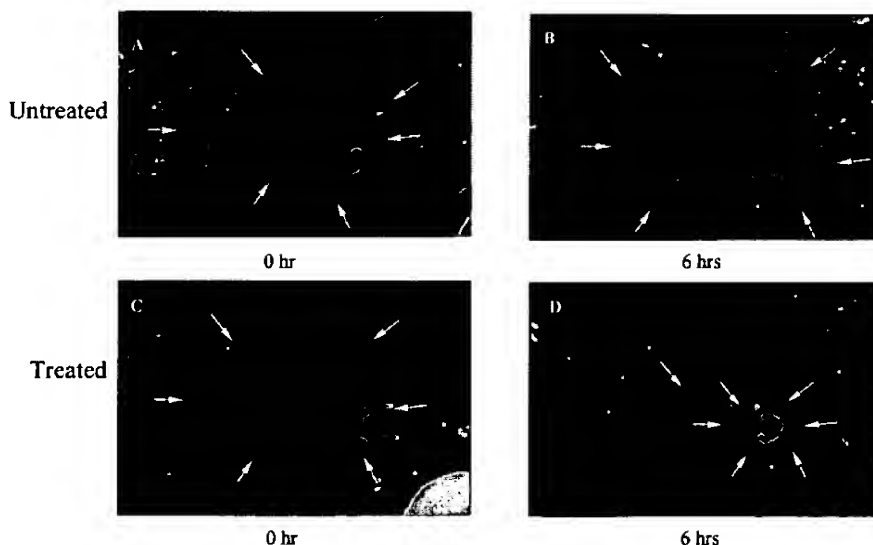**Fig. 4.** Whole-body imaging of *E. coli*-GFP peritoneal cavity infection and antibiotic response. (*A* and *C*) *E. coli*-GFP infection in the peritoneal cavity immediately after i.p. injection of 10⁹ *E. coli*-GFP. (*B*) Untreated mouse 6 h after i.p. injection. Animal died at this time point. (*D*) Kanamycin-treated mouse 6 h after i.p. injection. Animal survived. Arrows indicate the fluorescent images.

Fig. 5. Intravital imaging of *E. coli*-GFP peritoneal cavity infection. *E. coli*-GFP infection in the peritoneal cavity immediately after i.p. injection of 10^9 *E. coli*-GFP. The wall of the abdominal cavity was removed.

developed and implanted orthotopically, where they express their proper metastatic behavior. The strong GFP fluorescence allowed detection of micrometastases down to the single-cell level. In the course of these studies, we noted that the strong tumor luminescence was visible from outside the intact, living animal. The ability to noninvasively image tumors enabled an entire program of research.

We also applied the GFP whole-body imaging technique to visualize gene expression in several organs of the mouse (19). Mice were labeled in the brain, liver, pancreas, prostate, or bone by using adenoviral-GFP (19). This technique may allow the noninvasive visualizing of the expression and modulation of specific genes that have been coupled to GFP.

Recently, we have shown whole-body images of angiogenesis in GFP-expressing tumors in mice, including orthotopically implanted tumors (20). In this technique the nonfluorescent tumor induced blood vessels are readily apparent in stark contrast to the GFP-fluorescent tumors. The whole-body images, enable quantitation of tumor vascularization noninvasively in real time.

GFP-expressing bacteria have been previously used in a number of studies that did not involve intact, living animals (21–29). An example of such studies was the visualization of the *in vitro* infection of muscle tissue by the pathogenic *E. coli* O157H GFP (28). Another approach examined the mouse gastrointestinal tract after gavage infection by removal and fixation of the gastrointestinal tissue (29). Fish infected with

GFP-transduced *Edwardsiella tarda* were imaged for infection after removal of their organs (22). Genes associated with virulence and other infectious processes were evaluated by linkage to GFP expression (22–25).

A very different technique for generating and imaging interior luminescence uses bioluminescent bacteria. The light source is the luciferin–luciferase reaction, the quantum yield of which appears to be far lower than for an equivalent bacterial population labeled with GFP. Although the infection could be whole-body imaged, the signal was relatively weak. Consequently, imaging required long collection times during which the animal had to be immobilized and anesthetized. The signal from the much brighter GFP-labeled bacteria allowed instantaneous image capture with high organ resolution, even in a simple light box, with freely moving animals in a lighted room. No substrates, radioactivity, contrast agent, anesthesia, or other perturbation is required, just illumination with blue light.

The technique of whole-body imaging of *E. coli*-GFP infection in mice reported here is a significant advance that enables real-time infection studies in a mammal without perturbing the animal. The whole-body imaging capability could be used to screen and study the efficacy of new antibiotics on drug-resistant, GFP-labeled bacteria. It will be possible to see the bacterial behavior in various organs of the mouse. Virulence genes can also be studied with regard to how they influence infection in various organs by whole-body imaging in real time. The whole-body imaging technique should allow greatly increased precision and detail in examining bacterial–host interactions.

<div style="writing-mode: vertical-rl">MEDICAL SCIENCES</div>

1. Hoffman, R. M. (1999) *Methods Enzymol.* 302, 20–31.
2. Chishima, T., Miyagi, Y., Wang, X., Yamaoka, H., Shimada, H., Moossa, A. R. & Hoffman, R. M. (1997) *Cancer Res.* 57, 2042–2047.
3. Rashidi, B., Yang, M., Jiang, P., Baranov, E., An, Z., Wang, X., Moossa, A. R. & Hoffman, R. M. (2000) *Clin. Exp. Metastasis* 18, 57–60.
4. Yang, M., Hasegawa, S., Jiang, P., Wang, X., Tan, Y., Chishima, T., Shimada, H., Moossa, A. R. & Hoffman, R. M. (1998) *Cancer Res.* 58, 4217–4221.
5. Yang, M., Jiang, P., Sun, F. X., Hasegawa, S., Baranov, E., Chishima, T., Shimada, H., Moossa, A. R. & Hoffman, R. M. (1999) *Cancer Res.* 59, 781–786.
6. Bouvet, M., Yang, M., Nardin, S., Wang, X., Jiang, P., Baranov, E., Moossa, A. R. & Hoffman, R. M. (2000) *Clin. Exp. Metastasis* 18, 213–218.
7. Yang, M., Baranov, E., Jiang, P., Sun, F.-X., Li, X.-M., Li, L., Hasegawa, S., Bouvet, M., Al-Tuwaijri, M., Chishima, T., *et al.* (2000) *Proc. Natl. Acad. Sci. USA* 97, 1206–1211.
8. Budinger, T. F., Benaron, D. A. & Koretsky, A. P. (1999) *Ann. Rev. Biomed. Eng.* 1, 611–648.

9. Herschman, H. R., MacLaren, D. C., Iyer, M., Namavari, M., Bobinski, K., Green, L. A., Wu, L., Berk, A.J. Toyokuni, T., Barrio, J. R., *et al.* (2000) *J. Neurosci. Res* 59, 699–705.
10. Louie, A. Y., Huber, M. M., Ahrens, E. T., Rothbacher, U., Moats, R., Jacobs, R. E., Fraser, S. E. & Meade, T. J. (2000) *Nat. Biotechnol.* 18, 321–325.
11. Weissleder, R., Moore, A., Mahmood, U., Bhorade, R., Benveniste, H., Chiocca, E. A. & Basilion, J. P. (2000) *Nat. Med.* 6, 351–354.
12. Gambhir, S. S., Barrio, J. R., Phelps, M. E., Iyer, M., Namavari, M., Satyamurthy, N., Wu, L., Green, L. A., Bauer, E., MacLaren, D. C., *et al.* (1999) *Proc. Natl. Acad. Sci. USA* 96, 2333–2338.
13. Tjuvajev, J. G., Finn, R., Watanabe, K., Joshi, R., Oku, T., Kennedy, J., Beattie, B., Koutcher, J., Larson, S. & Blasberg, R. G. (1996) *Cancer Res.* 56, 4087–4095.
14. Contag, P. R., Olomu, I. N., Stevenson, D. K. & Contag, C. H. (1998) *Nat. Med.* 4, 245–247.
15. Alfano, R. R., Demos, S. G. & Gayen, S. K. (1997) *Ann. N.Y. Acad. Sci.* 820, 248–270.
16. Masters, B. R., So, P. T. & Gratton, E. (1998) *Ann. N.Y. Acad. Sci* 838, 58–67.

17. Wu, J., Perelman, L., Dasari, R. & Feld, M. (1997) *Proc. Natl. Acad. Sci. USA* **94,** 8783–8788.
18. Alfano, R. R., Demos, S. G., Galland, P., Gayen, S. K., Guo, Y., Ho, P. P., Liang, X., Liu, F., Wang, L., Wang, Q. Z. & Wang, W. B. (1998) *Ann. N.Y. Acad. Sci.* **838,** 14–28.
19. Yang, M., Baranov, E., Moossa, A. R., Penman, S. & Hoffman, R. M. (2000) *Proc. Natl. Acad. Sci. USA* **97,** 12278–12282.
20. Yang, M., Baranov, E., Li., X-M., Wang, J-W., Jiang, P., Li, L., Moossa, A. R., Penman, S. & Hoffman, R. M. (2001) *Proc. Natl. Acad. Sci. USA* **98,** 2616–2621.
21. Wu, H., Song, Z., Hentzer, M., Andersen, J. B., Heydorn, A., Mathee, K., Moser, C., Eberl, L., Molin, S., Hoiby, N. & Givskov, M. (2000) *Microbiology* **146,** 2481–2493.
22. Ling, S. H., Wang, X. H., Xie, L., Lim, T. M. & Leung, K. Y. (2000) *Microbiology* **146,** 7–19.
23. Badger, J. L., Wass, C. A. & Kim, K. S. (2000) *Mol. Microbiol.* **36,** 174–182.
24. Kohler, R., Bubert, A., Goebel, W., Steinert, M., Hacker, J. & Bubert, B. (2000) *Mol. Gen. Genet.* **262,** 1060–1069.
25. Valdivia, R. H., Hromockyj, A. E., Monack, D., Ramakrishnan, L. & Falkow, S. (1996) *Gene* **173,** 47–52.
26. Valdivia, R. H. & Falkow, S. (1997) *Science* **277,** 2007–2011.
27. Scott, K. P., Mercer, D. K., Richardson, A. J., Melville, C. M., Glover, L. A. & Flint, H. J. (2000) *FEMS Microbiol. Lett.* **182,** 23–27.
28. Prachaiyo, P. & McLandsborough, L. A. (2000) *J. Food Prot.* **63,** 427–433.
29. Geoffroy, M. C., Guyard, C., Quatannens, B., Pavan, S., Lang, M. & Mercenier, A. (2000) *Appl. Environ. Microbiol.* **66,** 383–391

Whole-body and intravital optical imaging of angiogenesis in orthotopically implanted tumors

Meng Yang*, Eugene Baranov*, Xiao-Ming Li*, Jin Wei Wang*, Ping Jiang*, Lingna Li*, A. R. Moossa†, Sheldon Penman‡, and Robert M. Hoffman*†§

*AntiCancer, Inc., 7917 Ostrow Street, San Diego, CA 92111; †Department of Surgery, University of California, 200 West Arbor Drive, San Diego, CA 92103-8220; and ‡Department of Biology, Massachusetts Institute of Technology, 77 Massachusetts Avenue, Cambridge, MA 02139-4307

The development of drugs for the control of tumor angiogenesis requires a simple, accurate, and economical assay for tumor-induced vascularization. We have adapted the orthotopic implantation model to angiogenesis measurement by using human tumors labeled with *Aequorea victoria* green fluorescent protein for grafting into nude mice. The nonluminous induced capillaries are clearly visible against the very bright tumor fluorescence examined either intravitally or by whole-body luminance in real time. The orthotopic implantation model of human cancer has been well characterized, and fluorescence shadowing replaces the laborious histological techniques for determining blood vessel density. Intravital images of orthotopically implanted human pancreatic tumors clearly show angiogenic capillaries at both primary and metastatic sites. A quantitative time course of angiogenesis was determined for an orthotopically growing human prostate tumor periodically imaged intravitally in a single nude mouse over a 19-day period. Whole-body optical imaging of tumor angiogenesis was demonstrated by injecting fluorescent Lewis lung carcinoma cells into the s.c. site of the footpad of nude mice. The footpad is relatively transparent, with comparatively few resident blood vessels, allowing quantitative imaging of tumor angiogenesis in the intact animal. Capillary density increased linearly over a 10-day period as determined by whole-body imaging. Similarly, the green fluorescent protein-expressing human breast tumor MDA-MB-435 was orthotopically transplanted to the mouse fat pad, where whole-body optical imaging showed that blood vessel density increased linearly over a 20-week period. These powerful and clinically relevant angiogenesis mouse models can be used for real-time *in vivo* evaluation of agents inhibiting or promoting tumor angiogenesis in physiological microenvironments.

green fluorescent protein | metastatic models | external optical imaging

Tumor vascularization or angiogenesis is a critical step in tumor growth, progression, and metastasis. As such, angiogenesis promises a uniquely effective yet remarkably benign target for cancer chemotherapy. A major requirement for the effective discovery of angiogenesis-related drugs is an assay system that is accurate, rapid, and economical. We report a model system that meets these requirements.

The discovery and evaluation of antiangiogenic substances initially relied on *in vivo* methods such as the chorioallantoic membrane assay (1, 2), the monkey iris neovascularization model (3), the disk angiogenesis assay (4), and various models that use the cornea to assess blood vessel growth (5–10). Although they are important for understanding the mechanisms of blood vessel induction, these models did not deal with tumor angiogenesis and are poorly suited to drug discovery.

Subcutaneous tumor xenograft angiogenesis models have been developed to study tumor angiogenesis, but these require cumbersome pathological examination procedures such as histology and immunohistochemistry. Measurements require animal sacrifice and therefore preclude ongoing angiogenesis stud-

ies in individual, live, tumor-bearing animals (11–14). Moreover, s.c. xenografts are not ideal models of human disease.

Tumors transplanted in the cornea of the rodents (15–17) and rodent skin-fold window chambers have been used for angiogenesis studies (18–20, 29–32). The cornea and skin-fold chamber models provide a means for studying angiogenesis in living animals. However, quantification requires specialized procedures, and the sites do not represent natural environments for tumor growth. The cornea and skin-fold tumor models do not allow orthotopic and metastatic angiogenesis, which may involve mechanisms of angiogenesis (33) that are qualitatively different from these ectopic models.

A suitable model for drug discovery will accurately represent clinical cancer as well as enable real-time visualization of the angiogenesis process and its inhibition by effective agents. To develop realistic and real-time tumor angiogenesis models, the present study utilizes surgical orthotopic implantation (SOI) metastatic models of human cancer (23). These models place tumors in natural microenvironments and replicate clinical tumor behavior more closely than do ectopic implantation models (23). For these studies the tumors implanted in the orthotopic model have been transduced and selected to strongly express green fluorescent protein (GFP) *in vivo* (23–27).

GFP expression in primary tumors and in their metastases in the mouse models can be detected by an intense fluorescence seen by intravital or by whole-body imaging. The nonluminous angiogenic blood vessels appear as sharply defined dark networks against this bright background. The high image resolution permits quantitative measurements of total vessel length. These genetically fluorescent tumor models allow quantitative optical imaging of angiogenesis *in vivo*. Tumor growth, vascularization, and metastasis can now be followed in real time (21–22).

Materials and Methods

Fluorescence Optical Imaging. A Leica fluorescence stereo microscope model LZ12 equipped with a mercury lamp and a 50-W power supply was used. Selective excitation of GFP was produced through a D425/60 band-pass filter and a 470 DCXR dichroic mirror. Emitted fluorescence was collected through a long-pass filter (GG475; Chroma Technology, Brattleboro, VT) on a Hamamatsu C5810 3-chip cooled color charge-coupled device camera (Hamamatsu Photonics, Bridgewater, NJ). Images were processed for contrast and brightness and analyzed with the use of IMAGE PRO PLUS 3.1 software (Media Cybernetics,
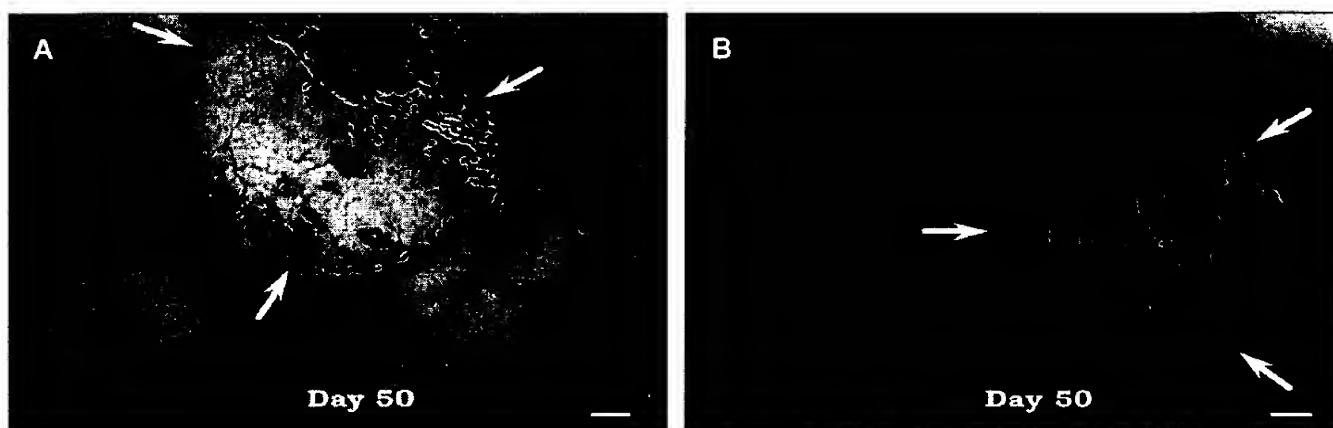
Fig. 1. Intravital fluorescence imaging of Bx-PC-3-GFP human pancreas cancer angiogenesis. (A) Orthotopic tumor. (B) Metastatic lesion in spleen. The GFP-expressing human tumor was transplanted to nude mice by SOI and intravitally imaged 50 days later, as described in *Materials and Methods*. (Bar = 200 μm.)

Silver Spring, MD). High-resolution images of 1024 × 724 pixels were captured directly on an IBM PC or continuously through video output on a high-resolution Sony VCR (model SLV-R1000; Sony, Tokyo).

Production of GFP Retrovirus. *GFP expression vector.* The pLEIN retroviral vector (CLONTECH) expressing enhanced GFP and the neomycin resistance gene on the same bicistronic message, which contains an internal ribosome entry site (24), was used to transduce tumor cells.

Packaging cell culture, vector production, transfection, and subcloning. PT67, a NIH 3T3-derived packaging cell line expressing the 10 Al viral envelope, was purchased from CLONTECH. PT67 cells were cultured in DMEM (Irvine Scientific) supplemented with 10% heat-inactivated FBS (Gemini Biological Products, Calabasas, CA). For vector production, packaging cells (PT67), at 70% confluence, were incubated with a precipitated mixture of N-[1-(2,3-dioleoyloxy)propyl]-N,N,N-trimethylammonium methylsulfate reagent (Roche Molecular Biochemicals) and saturating amounts of pLEIN plasmid for 18 h. Fresh medium was replenished at this time. The cells were examined by fluorescence microscopy 48 h after transfection. For selection, the cells were cultured in the presence of 500-2000 mg/ml of G418 (Life Technologies, Grand Island, NY) for 7 days (24).

Retroviral GFP Transduction of Tumor Cells. The cells used were PC-3 human prostate cancer (24), Bx-PC-3 pancreatic cancer (25), MDA-MB-435 human breast cancer (34), and mouse Lewis lung carcinoma (26). For GFP gene transduction, ≈25% confluent cells were incubated with a 1:1 precipitated mixture of retroviral supernatants of PT67 cells and RPMI 1640 (GIBCO) containing 10% FBS (Gemini Biological Products) for 72 h. Fresh medium was replenished at this time. Cells were harvested by trypsin/EDTA 72 h after transduction and subcultured at a ratio of 1:15 into selective medium, which contained 200 mg/ml of G418. The level of G418 was increased stepwise up to 1000 mg/ml for PC-3, 800 mg/ml for Bx-PC-3, 600 mg/ml for MDA MB-435, and 400 mg/ml for Lewis lung carcinoma cells. Clones stably expressing GFP were isolated with cloning cylinders (Bel-Art Products) with the use of trypsin/EDTA and were then amplified and transferred by conventional culture methods.

Animals. All animal studies were conducted in accordance with the principles and procedures outlined in the National Institutes of Health Guide for the Care and Use of Laboratory Animals

under assurance number A3873-1. Six-week-old BALB/c *nu/nu* male and female nude mice were used in this study.

SOI of Tumors (23). Tumor fragments (1 mm³), stably expressing GFP, previously grown s.c. in nude mice, were implanted by SOI on the appropriate organ in nude mice. After proper exposure of the organ to be implanted, 8-0 surgical sutures were used to penetrate the tumor pieces and attach them to the appropriate orthotopic organ. The incision in the skin was closed with a 7-0 surgical suture in one layer. The animals are kept under isoflurane anesthesia during surgery. All procedures of the operation described above were performed with a ×7 magnification microscope (MZ6; Leica, Nussloch, Germany).

Footpad Tumor Implantation. Nude mice were injected s.c. in the footpad with 2×10^4 Lewis lung carcinoma-GFP cells. Cells were first harvested by trypsinization and washed three times with cold serum medium and then injected in a total volume of 10 μl within 40 min of harvesting.

Quantitative Analysis of Angiogenesis. Periodically, the tumor-bearing mice were examined by intravital or whole-body fluorescence imaging. The extent of blood vessel development in a tumor was evaluated based on the total length of blood vessels (L) in chosen areas: areas containing the highest number of vessels were identified by scanning the tumors (28) by intravital or whole-body imaging. To compare the level of vascularization during tumor growth, the "hot" areas with the maximum development of vessels per unit area (35) were then quantitated for L expressed in pixels. Captured images were corrected for unevenness in illumination. Then the total number of pixels derived from the blood vessels was quantified with IMAGE PRO PLUS software.

Results and Discussion

Intravital Images of Angiogenesis of Orthotopic Bx-PC-3-GFP Pancreas Cancer. The clarity of angiogenic blood vessel imaging is illustrated by intravital examination of the orthotopic growth of a Bx-PC-3-GFP pancreatic tumor (Fig. 1A). The nonluminous blood vessels are clearly visible against the GFP fluorescence of the primary tumor. Angiogenesis associated with metastatic growths is also easily imaged by intravital examination. Fig. 1B shows angiogenesis of a Bx-PC-3-GFP tumor metastasis that has migrated to the spleen.

Intravital Imaging of Angiogenesis of Orthotopic PC-3-GFP Prostate Tumor. Because angiogenesis can now be measured without animal sacrifice, it is possible determine a time course for
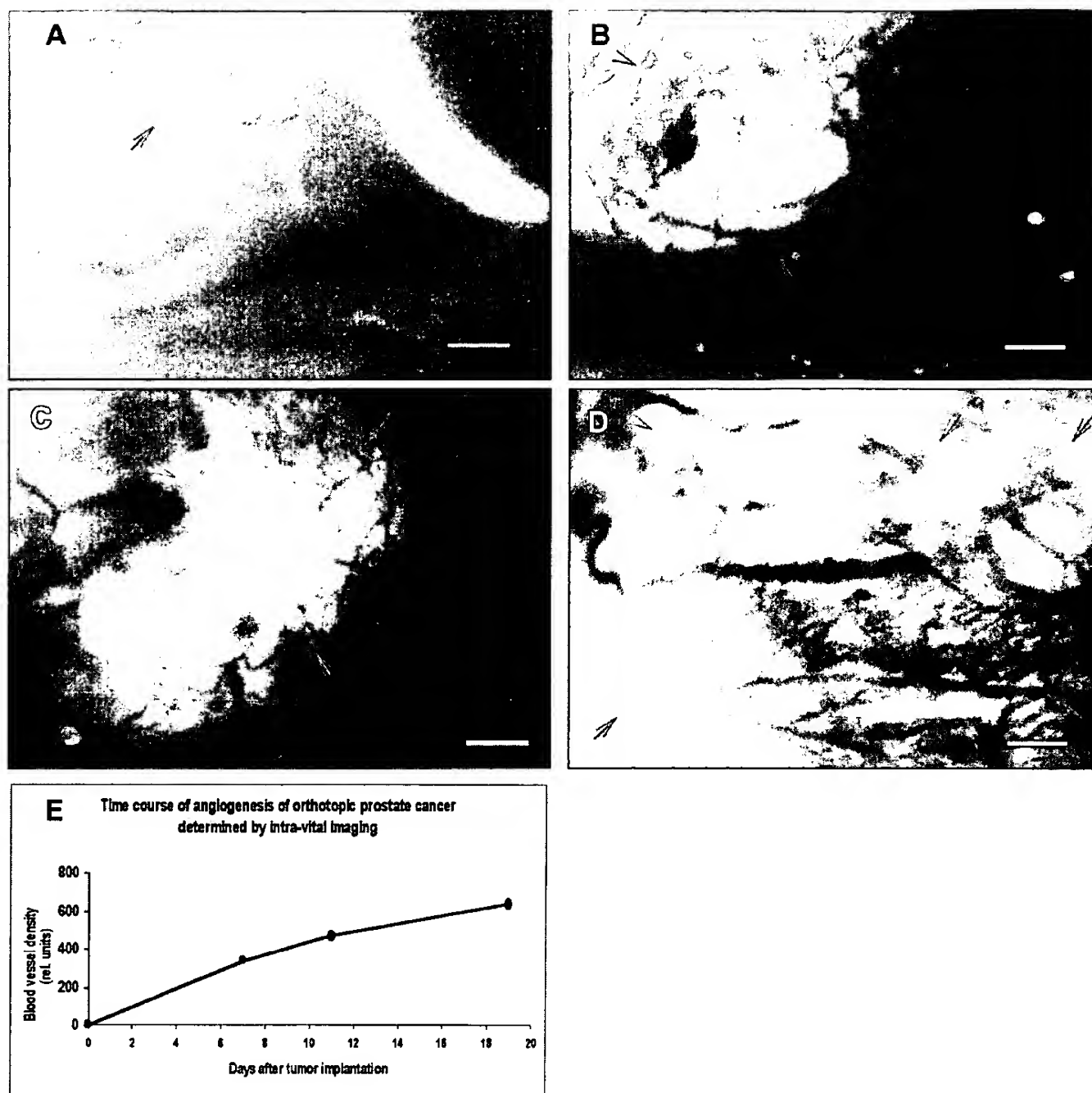
Fig. 2. Time course of intravital fluorescence imaging of PC-3-GFP human prostate cancer angiogenesis in orthotopic primary tumor. The GFP-expressing human tumor was transplanted to nude mice by SOI and imaged as described in *Materials and Methods*. (*A*) Day 1. (*B*) Day 7. (*C*) Day 11. (*D*) Day 19. (*E*) Quantitative graph of microvessel density as function of time. (Bar = 470 μm.)

individual animals. Fig. 2 shows sequential intravital images of angiogenesis for the human prostate tumor PC-3-GFP growing orthotopically in a single nude mouse. The tumor-associated blood vessels are clearly visible by day 7 and continue to increase at least until day 19.

Whole-Body Imaging of Angiogenesis of the Lewis Lung Carcinoma-GFP in the Mouse Footpad. Where possible, the most rapid, least invasive measurement is whole-body optical imaging. Fig. 3 *A–D* comprises whole-body optical images of the Lewis lung carcinoma-GFP growing in the footpad of a nude mouse. The footpad

was chosen for its relative transparency and comparatively few resident blood vessels. The onset of tumor angiogenesis and its progression over a 10-day period are clearly imaged in a completely noninvasive manner.

Whole-Body Imaging of Angiogenesis in MDA-MB-435-GFP Breast Cancer Growing Orthotopically in the Breast Fat Pad. Fig. 4 demonstrates the whole-body images and quantitation of the time course of angiogenesis of the MDA-MB-435-GFP human breast cancer growing orthotopically in the breast fat pad in a nude mouse. The development of the tumor and its angiogenesis could be imaged in a completely noninvasive manner.
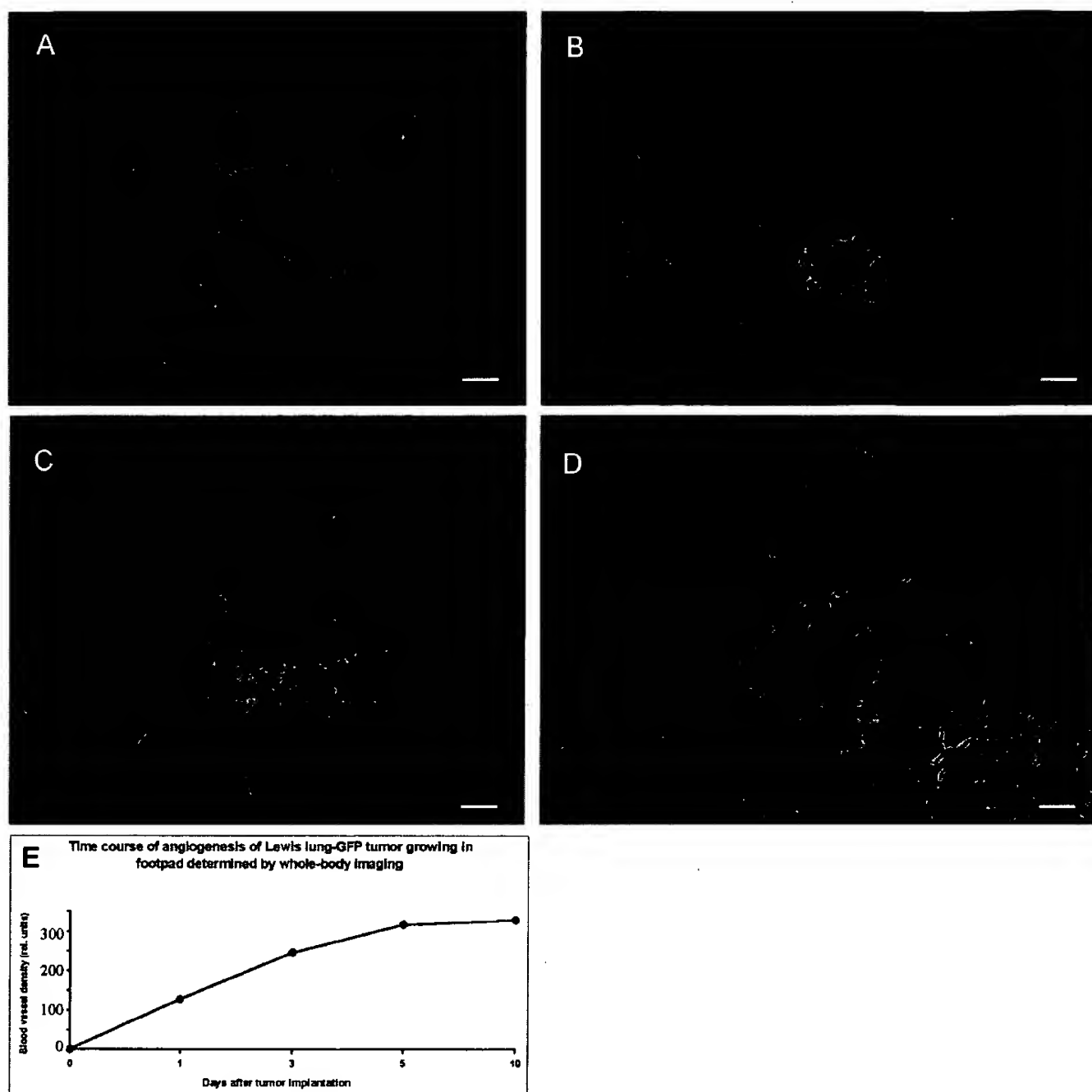
Fig. 3. Time course of whole-body fluorescence imaging of Lewis lung carcinoma-GFP angiogenesis in the mouse footpad. The GFP-expressing tumor cells were injected into the footpad of nude mice and whole-body imaged as described in *Materials and Methods*. (A) Day 3. (B) Day 6. (C) Day 8. (D) Day 13. (E) Quantitative graph of microvessel density as a function of time. (Bar = 500 μm.)

Quantitative Determination of Angiogenesis. The well-resolved, high-contrast images of tumor-associated blood vessels afforded by high-GFP-expression tumor cells allows real-time quantitative measurements of angiogenesis *in vivo*. The quantitative data obtained by intravital examination of the PC-3-GFP prostate tumor (Fig. 2E) show an increase in vessel density over 20 days. These demonstrate quantifying angiogenesis of internally growing, orthotopic tumors without sacrificing the animal.

A wholly noninvasive, quantitative measurement of angiogenesis is possible at sites such as the mouse foot pad. The tissue is relatively transparent, with few endogenous blood vessels. The

increase in vessel density of the Lewis lung carcinoma-GFP was quantified from whole-body images over 10 days (Fig. 3E). The sensitivity of the method is shown by detection of Lewis lung carcinoma-GFP angiogenesis at high resolution as early as 3 days after implantation (Fig. 3A).

The mouse breast fat pad is the orthotopic environment for the implanted MDA-MB-435-GFP breast cancer and allows noninvasive, whole-body imaging of tumor angiogenesis. The quantitative angiogenesis data show that microvessel density increased over 20 weeks (Fig. 4E). Thus, tumors, even in their natural microenvironment, growing orthotopically in sites such
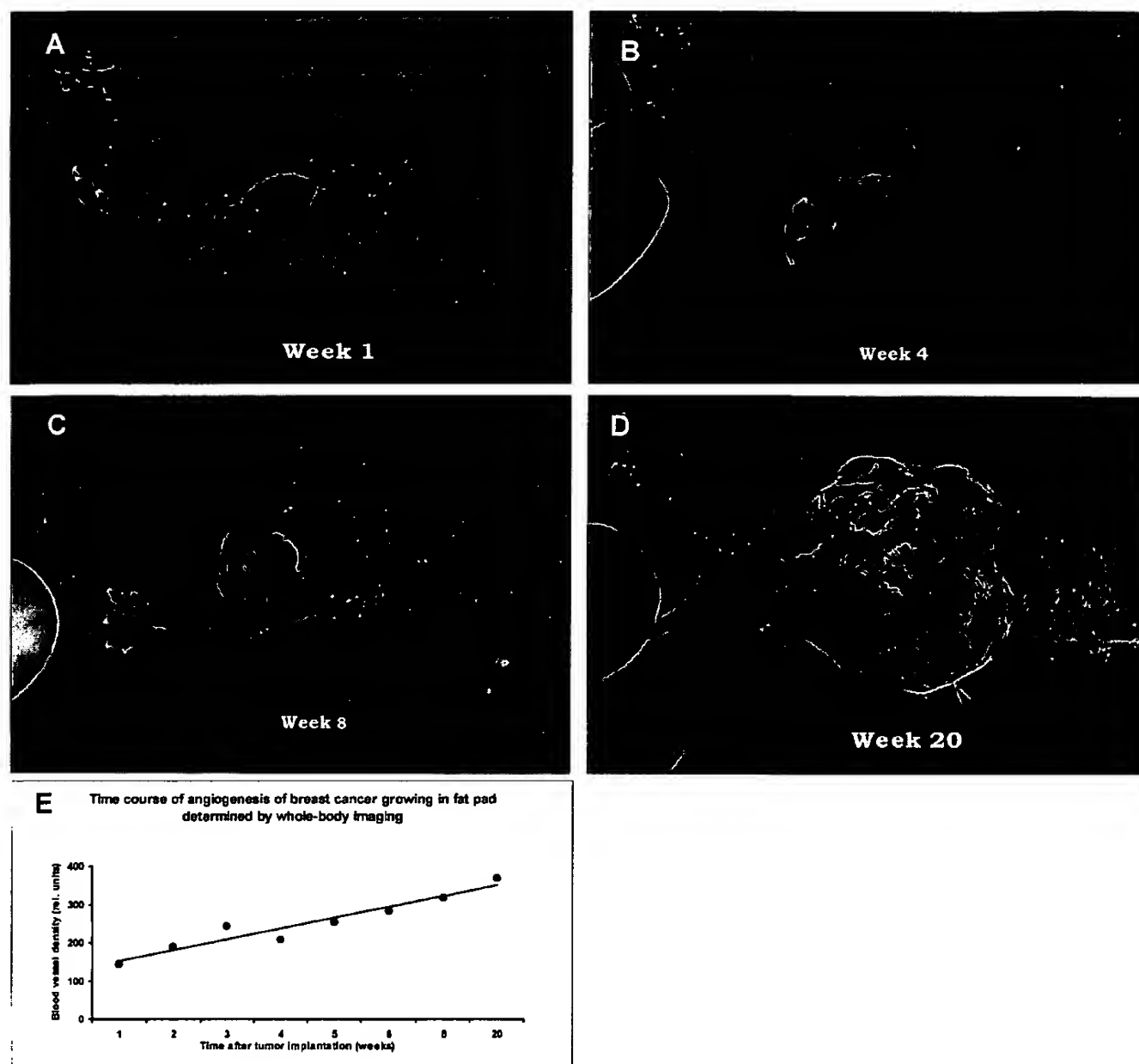
Fig. 4. Time course of whole-body fluorescence imaging of MDA-MB-435-GFP human breast cancer angiogenesis in orthotopic primary tumor. The GFP-expressing human tumor was transplanted by SOI in the fat pad of nude mice and whole-body imaged as described in *Materials and Methods*. (*A*) Week 1. (*B*) Week 4. (*C*) Week 8. (*D*) Week 20. (*E*) Quantitative graph of microvessel density as a function of time.

as the fatpad and presumably others, can be whole-body imaged for quantitative angiogenesis studies.

Comparative Advantages of Fluorescent Tumor Imaging. The present tumor angiogenesis models shown here have many advantages over the traditional tumor angiogenesis models such as the chicken chorioallantoic membrane assay (1, 2), rabbit cornea (5–10), skin-fold window (18–20, 29–32), and s.c. implantation (11–14). These sites are not normal sites for tumor growth, and their microenvironments are very different from orthotopic sites with regard to regulation not only of tumor growth but of the angiogenesis process itself (33). Furthermore, without a marker such as GFP, any type of visualization of angiogenesis requires animal sacrifice and cumbersome preparatory histological and

histochemical procedures, ruling out any type of noninvasive real-time studies.

Orthotopically implanted GFP-labeled tumors also allow the study of angiogenesis for metastasis. The orthotopically growing tumors, in contrast to most other models, give rise to spontaneous metastases that resemble, both in target tissues and in frequency of occurrence, the clinical behavior of the original human tumor (23). Moreover, the extreme detection sensitivity afforded by the strong GFP fluorescence allows imaging of very early events in blood vessel induction. As Li *et al.* (30) point out, angiogenesis initiation in metastatic tumors may be very different from that of primary tumors and require different interventions. They used skin-fold chambers with a transparent window for studies of early events in rodent tumor models, including

those expressing GFP (30, 32). Although these afforded a high detection sensitivity and allowed imaging of early angiogenic events, these were not actual metastases, and the ectopic microenvironment can be far from physiological.

The models for whole-body and intravital imaging of angio-genesis of human tumors described here enable the angiogenesis process to be visualized in real time at orthotopic sites, allowing relevant mechanistic studies. The whole-body imaging models will be of particular value for *in vivo* screening and evaluation of antiangiogenesis drugs.

1. Auerbach, R., Kubai, L., Knighton, D. & Folkman, J. (1974) *Dev. Biol.* **41**, 391–394.
2. Crum, R., Szabo, S. & Folkman, J. (1985) *Science* **230**, 1375–1378.
3. Miller, J. W., Stinson, W. G. & Folkman, J. (1993) *Ophthalmology* **100**, 9–14.
4. Passaniti, A., Taylor, R. M., Pili, R., Guo, Y., Long, P. V., Haney, J. A., Pauly, R. R., Grant, D. S. & Martin, G. R. (1992) *Lab. Invest.* **67**, 519–528.
5. Alessandri, G., Raju, F. & Gullino, P. M. (1983) *Cancer Res.* **43**, 1790–1797.
6. Deutsch, T. A. & Hughes, W. F. (1979) *Am. J. Ophthalmol.* **87**, 536–540.
7. Korey, M., Peyman, G. A. & Berkowitz, R. (1977) *Ann. Ophthalmol.* **9**, 1383–1387.
8. Mahoney, J. M. & Waterbury, L. D. (1985) *Curr. Eye Res.* **4**, 531–535.
9. Li, W. W., Grayson, G., Folkman, J. & D'Amore, P. A. (1991) *Invest. Ophthalmol. Vis. Sci.* **32**, 2906–2911.
10. Epstein, R. J., Hendricks, R. L. & Stulting, R. D. (1990) *Cornea* **9**, 318–323.
11. O' Reilly, M. S., Boehm, T., Shing, Y., Fukai, N., Vasios, G., Lane, W. S., Flynn, E., Birkhead, J. R., Olsen, B. R. & Folkman, J. (1997) *Cell* **88**, 277–285.
12. Drevs, J., Hofmann, I., Hugenschmidt, H., Wittig, C., Madjar, H., Muller, W., Wood, J., Martiny-Baron, G., Unger, C. & Marme, D. (2000) *Cancer Res.* **60**, 4819–4824.
13. Prewett, M., Huber, J., Li, Y., Santiago, A., O'Connor, W., King, K., Overholser, J., Hooper, A., Pytowski, B., Witte, L., *et al.* (1999) *Cancer Res.* **59**, 5209–5218.
14. Kurebayashi, J., Kunisue, H., Yamamoto, S., Kurosumi, M., Otsuki, T. & Sonoo, H. (2000) *Oncology* **59**, 158–165.
15. Gimbrone, M. A., Cotran, I. S., Leapman, S. B. & Folkman, J. (1974) *J. Natl. Cancer Inst.* **54**, 413–427.
16. Fournier, G. A., Lutty, G. A., Watt, S., Fenselau, A. & Patz, A. (1981) *Invest. Ophthalmol. Vis. Sci.* **21**, 351–354.
17. Muthukkaruppan, V. & Auerbach, R. (1979) *Science* **205**, 1416–1418.
18. Papenfuss, H. D., Gross, J. F., Intaglietta, M. & Treese, F. A. (1979) *Microvasc. Res.* **18**, 311–318.
19. Gross, J., Roemer, R., Dewhirst, M. & Meyer, T. (1982) *Int. J. Heat Mass Transfer* **25**, 1313–1320.
20. Dewhirst, M., Gross, J., Sim, D., Arnold, P. & Boyer, D. (1984) *Biorheology* **21**, 539–558.
21. Yang, M., Baranov, E., Jiang, P., Sun, F.-X., Li, X.-M., Li, L., Hasegawa, S., Bouvet, M., Al-Tuwaijri, M., Chishima, T., *et al.* (2000) *Proc. Natl. Acad. Sci. USA* **97**, 1206–1211.
22. Yang, M., Baranov, E., Moossa, A. R., Penman, S. & Hoffman, R. M. (2000) *Proc. Natl. Acad. Sci. USA* **97**, 12278–12282.
23. Hoffman, R. M. (1999) *Investigational New Drugs* **17**, 343–359.
24. Yang, M., Jiang, P., Sun, F. X., Hasegawa, S., Baranov, E., Chishima, T., Shimada, H., Moossa, A. R. & Hoffman, R. M. (1999) *Cancer Res.* **59**, 781–786.
25. Bouvet, M., Yang, M., Nardin, S., Wang, X., Jiang, P., Baranov, E., Moossa, A. R. & Hoffman, R. M. (2001) *Clin. Exp. Metastasis*, in press.
26. Rashidi, B., Yang, M., Jiang, P., Baranov, E., An, Z., Wang, X., Moossa, A. R. & Hoffman, R. M. (2000) *Clin. Exp. Metastasis* **18**, 57–60.
27. Chishima, T., Miyagi, Y., Wang, X., Yamaoka, H., Shimada, H., Moossa, A. R. & Hoffman, R. M. (1997) *Cancer Res.* **57**, 2042–2047.
28. Takahashi, Y., Kitadai, Y., Bucana, C. D., Cleary, K. R. & Ellis, L. M. (1995) *Cancer Res.* **55**, 3964–3968.
29. Fukumura, D., Xavier, R., Sugiura, T., Chen, Y., Park, E. C., Lu, N., Selig, M., Nielsen, G., Taksir, T., Jain, R. K., *et al.* (1998) *Cell* **94**, 715–725.
30. Li, C. Y., Shan, S., Huang, Q., Braun, R. D., Lanzen, J., Hu, K., Lin, P. & Dewhirst, M. W. (2000) *J. Natl. Cancer Inst.* **92**, 143–147.
31. Al-Mehdi, A. B., Tozawa, K., Fisher, A. B., Shientag, L., Lee, A. & Muschel, R. J. (2000) *Nat. Med.* **6**, 100–102.
32. Huang, Q., Shan, S., Braun, R. D., Lanzen, J., Anyrhambatla, G., Kong, G., Borelli, M., Corry, P., Dewhirst, M. W. & Li, C. Y. (1999) *Nat. Biotechnol.* **17**, 1033–1035.
33. Cowen, S. E., Bibby, M. C. & Double, J. A. (1995) *Acta Oncol.* **34**, 357–360.
34. Bagheri-Yarmand, R., Kourbali, Y., Rath, A. M., Vassy, R., Martin, A., Jozefonvicz, J., Soria, C., Lu, H. & Crepin, M. (1999) *Cancer Res.* **59**, 507–510.
35. Van Der Laak, J. A., Westphal, J. R., Schalkwijk, L. J., Pahlplatz, M. M., Ruiter, D. J., De Waal, R. M. & De Wilde, P. C. (1998) *J. Pathol.* **184**, 136–143.

Nestin Enhancer Requirements for Expression in Normal and Injured Adult CNS

Clas B. Johansson,[1] Carina Lothian,[1] Magnus Molin,[2] Hideyuki Okano,[3] and Urban Lendahl[1]*

[1]Department of Cell and Molecular Biology, Medical Nobel Institute, Karolinska Institute, Stockholm, Sweden
[2]Department of Medical Biochemistry and Microbiology, BioMedical Center (BMC), Uppsala, Sweden
[3]Department of Physiology, Keio University School of Medicine, Tokyo, Japan

The nestin gene is expressed in many CNS stem/progenitor cells, both in the embryo and the adult, and nestin is used commonly as a marker for these cells. In this report we analyze nestin enhancer requirements in the adult CNS, using transgenic mice carrying reporter genes linked to three different nestin enhancer constructs: the genomic rat nestin gene and 5 kb of upstream nestin sequence (NesP*lacZ*/3), 636 bp of the rat nestin second intron (E/nestin:EGFP), and a corresponding 714 bp region from the human second intron (Nes714tk/*lacZ*). NesP*lacZ*/3 and E/nestin:EGFP mice showed reporter gene expression in stem cell-containing regions of brain and spinal cord during normal conditions. NesP*lacZ*/3 and E/nestin:EGFP mice showed increased expression in spinal cord after injury and NesP*lacZ*/3 mice displayed elevated expression in the periventricular area of the brain after injury, which was not the case for the E/nestin:EGFP mice. In contrast, no expression in adult CNS in vivo was seen in the Nes714tk/*lacZ* mice carrying the human enhancer, neither during normal conditions nor after injury. The Nes714 tk/*lacZ* mice, however, expressed the reporter gene in reactive astrocytes and CNS stem cells cultured ex vivo. Collectively, this suggests a species difference for the nestin enhancer function in adult CNS and that elements outside the second intron enhancer are required for the full injury response in vivo.
© 2002 Wiley-Liss, Inc.

Key words: stem cell; CNS injury; astrocyte; spinal cord; neurogenesis

In the embryonic mammalian brain, neuroectodermal stem cells lining the neural tube proliferate and migrate to give rise to neurons, astrocytes and oligodendrocytes (Jacobson, 1991; Temple and Davis, 1994; Williams and Price, 1995). More recently, the adult CNS has also been shown to harbor stem cells. Adult CNS stem cells were isolated originally from the ventricular wall of the brain and could be cultured in vitro and maintained in the stem cell state in the presence of epidermal growth factor

(EGF) and basic fibroblast growth factor (bFGF) (Reynolds and Weiss, 1992; Gritti et al., 1995). In vivo, the adult CNS stem cells located in the ventricular wall give rise to immature neurons that migrate along the rostral migratory stream to the olfactory bulb, where they differentiate and integrate as interneurons (Lois and Alvarez-Buylla, 1994; Luskin and McDermott, 1994). The precise localization of the adult CNS stem cells in the ventricular wall remains a matter of debate. Evidence has been provided for stem cells that are located both in the subventricular zone (Doetsch et al., 1999) and in the ependymal layer (Johansson et al., 1999a), but the relationship between these two stem cell populations remains to be elucidated (Wang and Barres, 2000; Cassidy and Frisén, 2001). It has also been shown that adult CNS stem cells are endowed with a very wide differentiation potential. Transplantation of adult CNS stem cells to the hematopoietic system of sublethally irradiated mice leads to repopulation of blood cells (Bjornson et al., 1999), and transplantation to injured muscle leads to differentiation to myotubes (Galli et al., 2000). In addition, when adult CNS stem cells are introduced into early mouse or chick embryos, the cells contribute to tissues of all three germ layers (Clarke et al., 2000).

Although adult and embryonic CNS stem cells both generate all principal CNS cell types (Reynolds and Weiss, 1996), less is known about potential differences in gene regulation between the adult and embryonic CNS stem cells. In this article, we analyze the regulation of the nestin gene, because nestin is expressed both in embryonic and adult CNS stem cells. Nestin expression in the embryonic

CNS is spatially and temporally linked closely to the proliferating cell state (Lendahl et al., 1990), which makes it a commonly used marker for this cell type (Hockfield and McKay, 1985; Frederiksen and McKay, 1988; Fishell et al., 1993; Williams and Price, 1995). Similarly, nestin expression is a hallmark of adult CNS stem cells, both in vivo and when the adult CNS stem cells are cultured in vitro under nondifferentiating conditions (Reynolds and Weiss, 1992; Morshead et al., 1994; Johe et al., 1996). Nestin expression is downregulated when CNS stem cells differentiate and other members of the intermediate filament gene family are expressed, primarily neurofilament in neurons and glial fibrillary acidic protein (GFAP) in astrocytes (Frederiksen and McKay, 1988; Dahlstrand et al., 1995; Johe et al., 1996). In addition to the expression in embryonic and adult CNS stem cells, nestin is re-expressed after different types of cellular stress in the CNS. In particular, reactive astrocytes re-express nestin, both in the spinal cord (Frisén et al., 1995) and in the brain (Holmin et al., 1997). Nestin is also expressed in CNS tumors, and the degree of nestin expression correlates with the severity of the CNS tumor (Dahlstrand et al., 1992; Tohyama et al., 1992).

Regulatory elements controlling the embryonic expression of nestin in the CNS have been identified by linking various regions of the nestin gene to the reporter gene *lacZ* in transgenic mice. Originally, it was observed that the second intron of the rat nestin gene contains important enhancer elements for embryonic CNS expression (Zimmerman et al., 1994) and more recent investigations have revealed a complex composition of the second intron enhancer for embryonic expression. The second intron is evolutionarily highly conserved between rat and humans, particularly in the more 3' part, and a 374 basepair (bp) region of the human second intron is sufficient to mediate a pan-CNS expression in the developing CNS (Lothian and Lendahl, 1997). In addition, removal of a 120 bp domain within the most conserved 714 bp in the second intron results in loss of the pan-CNS embryonic expression, and expression is only retained in a small region in the embryonic mid/forebrain and at rhombomere boundaries (Josephson et al., 1998; Lothian et al., 1999; Yaworsky and Kappen, 1999). A 636 bp region of the rat nestin second intron is sufficient to recapitulate nestin expression in the developing CNS (Kawaguchi et al., 2001). In sum, these data indicate a complex regulation of the nestin gene during embryonic CNS development, and in this report we have addressed which regulatory nestin regions are required for expression in adult CNS stem cells under both normal conditions and after CNS injury. We have approached this by using three different transgenic mouse lines, carrying nestin enhancer elements of different length and derived from human or rat nestin, to reveal possible species differences and to identify important regulatory regions. These three lines were also selected because they have very similar reporter gene expression patterns in the embryonic CNS, which largely mimic the nestin expression in the proliferating CNS cells

(Zimmerman et al., 1994; Lothian and Lendahl, 1997; Kawaguchi et al., 2001). We also analyze the enhancer requirements for expression in adult CNS stem cells and reactive astrocytes during in vitro culture, and in a CNS tumor cell line. We conclude from these experiments that the origin of the nestin second intron enhancer, i.e., whether it is derived from rat or man, makes a differences for reporter gene expression in the adult; thus, we observe expression in the adult CNS only in transgenic mice carrying rat enhancer elements. The human second intron enhancer, however, is sufficient for expression in CNS stem cells and reactive astrocytes cultured ex vivo. In addition to this species difference, we also conclude that elements located outside a 714 bp region of the second rat intron are required for the full response after brain and spinal cord injury.

MATERIALS AND METHODS

DNA Constructs

The NesP*lacZ*/3 construct consists of the *lacZ* gene flanked by 5 kb of rat nestin upstream sequences and the almost complete nestin gene, including the three introns, as described by Zimmerman et al. (1994). In this construct, transcription starts from the endogenous transcription start site in the nestin gene. The Nes714tk/*lacZ* construct carries 714 bp of the second intron of the human nestin gene in front of a 107 bp basic thymidine kinase promoter and the *lacZ* gene, and has been described previously (Lothian and Lendahl, 1997).

Generation and Analysis of Transgenic Mice

Transgenic mice were generated by pronuclear injection of linearized plasmid DNA from the NesP*lacZ*/3 and Nes714tk/*lacZ* constructs into the pronuclei of newly fertilized F2 (C57Bl6 × CBA) oocytes, and the oocytes were transferred to fostermothers as previously described (Nilsson and Lendahl, 1993). The resulting offspring was screened for integration of the DNA by PCR analysis for the *lacZ* gene, as described previously (Nilsson and Lendahl, 1993; Lothian and Lendahl, 1997). Stable transgenic mouse lines were established by breeding one founder male from each line with F1 (C57Bl6 × CBA) or C57Bl6 females. Sections for X-gal histochemistry (see below) from adult CNS tissue of wild-type and transgenic mice obtained from cryosectioning.

Analysis of Adult E/nestin:EGFP Transgenic Mice

Three adult female E/nestin:EGFP transgenic mice (Kawaguchi et al., 2001) on the C57Bl/6 genetic background were used to study the endogenous nestin and the nestin-EGFP expression under normal condition (one mouse) and after a lesion to the spinal cord and the brain (cortex; two mice). Four days post surgery mice were deeply anaesthetized with an overdose of chloral hydrate and perfused with 37°C NaCl (9 mg/ml) followed by ice cold 4% formaldehyde in phosphate buffered saline (PBS). Tissue of interest was mounted in Tissue-Tek®, frozen rapidly, cut (10–14 μm) in a cryostat and collected on Superfrost Plus® glasses.

Injury Model

Four animals from the Nes714tk/*lacZ* and the NesP*lacZ*/3 lines, respectively, were used to study the reporter gene expression pattern in the CNS induced by needle insertion to the cortex. The mice were anesthetized deeply with chloral hydrate (150 mg/kg) and placed in a stereotaxic frame. The needle was inserted with the following coordinates: 0.4 mm posterior and 1.8 mm lateral to bregma and 3.0 mm below the dura mater. A lesion to the spinal cord was generated after a laminectomy at the upper thoracic level (T2), where the dorsal funiculus was cut transversely with microsurgical scissors and extended rostrally by a superficial longitudinal incision in the dorsal funiculus, as described previously (Frisén et al., 1992).

Neurosphere Cultures

Adult neural stem cell cultures, grown as neurospheres, were generated as described previously (Johansson et al., 1999b). Briefly, the lateral wall of the lateral ventricles in the brain or the area immediately surrounding the central canal in the spinal cord were collected from transgenic and control mice. The tissue was dissociated enzymatically at 37°C for 20 min in Hank's buffered salt solution (HBSS) with 2 mM glucose containing 1 mg/ml hyaluronic acid, 0.2 mg/ml kynurenic acid, 5 mg/ml trypsin and 200 U/ml DNase I. The cells were centrifuged at 200×*g* for 5 min and the pellet was resuspended in culture medium consisting of Dulbecco's modified Eagle medium (DMEM)/F-12 media containing 20 ng/ml EGF, 20 ng/ml bFGF, B27 supplement, 100 U/ml penicillin and 100 μg/ml streptomycin. Differentiation of neurospheres was carried out as described previously (Johansson et al., 1999b). Clonally derived neurospheres were plated on poly-L-ornithin (PLO, 15 μg/ml) coated glass coverslips and cultured in DMEM/F-12 with penicillin/streptomycin, B27 and 1% FBS without mitogens. After 7–10 days in culture the neurospheres were fixed with ice cold 4% formaldehyde in PBS for 10–15 min, rinsed with PBS and processed for immunohistochemistry.

Astrocyte Cultures

Eight newborn (P2) pups from the transgenic lines NesP*lacZ*/3 and Nes714tk/*lacZ* were used for establishing primary cell cultures. The meninges were removed and the brains digested enzymatically with papain (2.5 mg in 5 ml PBS, containing 1 mg/ml BSA, 10 mM glucose and 100 μg/ml DNase I) for 30 min in 37°C. After trituration, the cells were collected by centrifugation and resuspended in DMEM with 10% FCS, 100 U/ml penicillin, 100 mg/ml streptomycin, and 2 mM L-glutamine, then plated in 75 cm² tissue culture flasks. This procedure results in a mixed glial culture. The medium was changed the next day and every fourth day thereafter. When the cultures were confluent after 10–12 days, they were placed on a rotary shaker set at 700 rpm for 3 hr in 37°C and the medium containing loosely adhering cells was discarded. The remaining cells, predominantly astrocytes, were rinsed with PBS and removed from the flask with trypsin-EDTA in PBS collected by centrifugation. The cells were resuspended in the medium and plated on a 10 cm tissue culture plate for 30 min. The supernatant containing more than 95% astrocytes was transferred to new 75 cm² flasks. This was done to obtain separate glial cultures based on difference in adhesion (McCarthy and de Vellis, 1980;

Frisén et al., 1995). After 7 days the cultures were detached with 0.17 mg/ml trypsin and 0.07 mg/ml EDTA (Life Technologies), collected by centrifugation, resuspended and plated on 35 mm cell culture dishes. Cultures were fixed after 5 days with 4% formaldehyde in PBS for 10–15 min before immunohistochemistry.

Immunohistochemistry

Astrocyte cultures. Cell cultures were incubated for 1 hr at 37°C with the following primary antibodies: rabbit anti-nestin 130 (1:2,000; Dahlstrand et al.,1992) or rabbit anti-GFAP (1:250; DAKO) diluted in PBS with 5% BSA and 0.3% Triton X-100. Primary antibodies were visualized with donkey anti-rabbit CY2 (1:500; Jackson ImmunoResearch) or donkey anti-rabbit CY3 (1:500; Jackson ImmunoResearch) diluted in PBS and incubated at room temperature for 45 min.

Neurospheres. After blocking for 1 hr at room temperature, the neurospheres were incubated with mouse anti-βIII-tubulin (1:500; BAbCO) and rabbit anti-β-gal (1:200; ICN/Cappel), or mouse anti-GFAP conjugated to CY3 (1:500; Sigma) and rabbit anti-β-gal (1:200; ICN/Cappel), or rabbit anti-nestin 130 (1:2000) and goat anti-β-gal (1:2,000; Biogenesis) for 1 hr at 37°C. Primary antibodies were visualized with donkey anti-mouse CY3 (1:500), donkey anti-rabbit CY2 (1:250) and donkey anti-goat CY3 (1:500; all Jackson ImmunoResearch). All antibodies were incubated in PBS with 5% BSA and 0.3% Triton X-100.

Cryostat Sections. Sections from the brain and spinal cord were incubated at 4°C O/N with rabbit anti-nestin #130 (1:2,000; Dahlstrand et al., 1992) diluted in PBS, 5% BSA, 0.3% Triton X-100 and 0.1% sodium azide. Secondary antibody, donkey anti-rabbit CY-3 (1:500; Jackson ImmunoResearch), was diluted in PBS and incubated at room temperature for 45 min. Sections were rinsed in PBS and mounted with Prolong® anti-fading medium (Molecular Probes). All images were collected with a Nixon Eclipse 800 epifluorescent microscope equipped with a CCD camera (SPOT diagnostics). Images were processed using Adobe® Photoshop®.

X-Gal Histochemistry and β-Galactosidase Quantification Assay

Cryosections (10 μm) from fresh frozen adult CNS were collected on Superfrost® glasses (Fisher Science) and fixed for 10 min with 4% formaldehyde in PBS, washed in PBS and incubated with X-gal solution for 2 hr as described previously (Lothian and Lendahl, 1997). In vitro cultured or adenovirus-infected cells were fixed with 4% paraformaldehyde or 0.2% glutaraldehyde and processed through X-gal histochemistry for 1 and 4 hr, respectively. For the β-galactosidase quantification assay, transgenic astrocytes were lysed and mixed with β-gal solution containing 2.5 mg/ml o-nitrophenyl-β-D-galactopyranoside (ONPG) and 3.5 μl/ml β-mercaptoethanol and measured in an Anthos Luminoscan Lucy 1.

Construction of a Nes1852tk*lacZ* Recombinant Adenovirus

The nes1852tk*lacZ* construct, encompassing the full length human second intron in front of the *lacZ* gene, was generated by first cloning the complete second intron,

nes1852 (Lothian and Lendahl, 1997), into the transfer plasmid pdeltaE1sp1A (Microbix Biosystems Inc.) in the *Hind*III restriction site. Plasmid E1sp1A.nes1852tk*lacZ* was reconstructed into a recombinant adenovirus essentially as described by Stow (1981). Briefly, a vector arm was produced by double digestion of genomic Ad5-dl309 DNA with *Xba*I and *Cla*I, followed by sucrose gradient purification of the long right hand 3.71–100 unit genomic fragment. Recombinant viruses were generated by in vivo recombination. Thus, 5 μg of the transfer plasmid E1sp1A.nes1852tk*lacZ* was mixed with 1 μg of Ad5-dl309 vector arm and cotransfected by the calcium phosphate coprecipitation technique to 293 cells. Plaque purified recombinant viruses were verified by Southern blot analysis of Hirt-extracted viral DNA (Hirt, 1967). The final reporter virus was named ad.nes1852tk*lacZ*. A high-titer stock of ad.nes1852tk*lacZ* was produced as described in Current Protocols in Human Genetics (Dracopoli, 1995).

Adenoviral Infection of RG2 and JEG-3 Cells

Ad.nes1852tk*lacZ* was diluted in DMEM containing 2% FCS and was added to rat glioma (RG2) and human choriocarcinoma (JEG-3) cells. After 1 hr incubation at 37°C 10% fresh FCS/DMEM was added and after 24 hr the cells were fixed with 0.2% glutaraldehyde for 5 min and processed for X-gal histochemistry as described previously (Lothian and Lendahl, 1997). The cells were incubated in the X-gal solution over night (as described above) and photographed.

RESULTS

NesP*lacZ*/3 but not Nes714tk/*lacZ* Transgenic Mice Express LacZ in Stem Cell-Containing Regions of the Brain and Spinal Cord

In this report we analyze reporter gene expression in adult CNS before and after injury from transgenic mice carrying various nestin enhancer combinations. We first analyzed reporter gene expression from the two transgenic lines that carry the *lacZ* reporter gene. One line, Nes714tk/*lacZ*, carries 714 bp of the 3′-most region of the human second intron coupled to a basic thymidine kinase promoter and the *lacZ* gene (Lothian and Lendahl, 1997). The other line, NesP*lacZ*/3, contains the complete rat nestin gene including the three introns and 5 kb of upstream nestin sequences (Zimmerman et al., 1994). A schematic depiction of the constructs may be seen in Figure 1A. We analyzed lacZ expression in the adult brain and spinal cord under normal, uninjured conditions. In the brain, cells in the ventricular wall from NesP*lacZ*/3 mice displayed a low level of lacZ expression, as visualized by X-gal histochemistry (Fig.1C). Similarly, sections from the spinal cord of the NesP*lacZ*/3 mice showed robust X-gal staining in cells immediately around the central canal (Fig. 1D). In contrast, we did not observe any detectable lacZ expression in the uninjured brain or spinal cord from the Nes714tk/*lacZ* mice (Fig. 1E,F).

Increased LacZ Expression is Observed in the Brain and Spinal Cord of NesP*lacZ*/3 Mice After CNS Injury

We next analyzed lacZ expression after a needle injury to the brain or after transection of the dorsal funiculus in the spinal cord (the injury paradigms are depicted schematically in Fig. 1B). In the majority of the NesP*lacZ*/3 mice, we observed cells expressing lacZ in the area close to the needle scar in the cortex, 4–5 days after the injury (Fig. 1G), which is in line with a previous report by Lin et al. (1995). Furthermore, a higher level of lacZ expression was observed in the ventricular wall both at the ipsilateral and contralateral side of the injury (Fig. 1G,K). No X-gal staining was observed after injury in sections from the Nes714tk/*lacZ* mice (Fig. 1I).

In the spinal cord, transection in the dorsal funiculus resulted in a distinct increase in lacZ expression in the NesP*lacZ*/3 mice as compared to the uninjured situation, both around the central canal and in the dorsal horns (Fig. 1H). In contrast, no lacZ expression could be detected in the spinal cord of Nes714tk/*lacZ* mice after injury (Fig. 1J). We conclude from these experiments that the two transgenic lines respond differently in the regulation of reporter gene expression in the adult CNS both in the uninjured situation and after injury. This may reflect a species difference, because the enhancers in the NesP*lacZ*/3*lacZ* and Nes714tk/*lacZ* mice were of rat and human origin, respectively.

E/nestin:EGFP Transgenic Mice Express EGFP in Brain and Spinal Cord and Partially Respond to CNS Injury

To address the possible species difference we analyzed the E/nestin:EGFP transgenic mice, which carry a 636 bp rat second enhancer, largely corresponding to the 714 bp human enhancer region in the Nes714tk/*lacZ* mice. We found that these mice express EGFP in the periventricular area of the brain (data not shown), which is in keeping with previous observations (Kawaguchi et al., 2001). The expression was not altered after a needle injury to the brain, neither at the ipsilateral or contralateral side, i.e., expression was still confined to the majority of cells in the ependymal layer and the subventricular zone (Fig. 2A–H). Notably, there was a close but not perfect correlation between EGFP and nestin expression. In contrast, we observed an upregulation of EGFP and endogenous nestin expression at the lesion site (Fig. 2I–L), but expression of EGFP was restricted to a subset of the nestin-expressing cells.

We next analyzed expression in the spinal cord before and after transection of the dorsal funiculus. In the uninjured situation, both nestin and EGFP were expressed around the central canal (Fig. 3A–D), in keeping with previous data (Kawaguchi et al., 2001). In contrast, the injury resulted in a markedly increased nestin expression (Fig. 3F), as observed previously (Frisén et al., 1995), and an increase in EGFP expression (Fig. 3G). In addition to the EGFP expression around the central canal, cells lo-
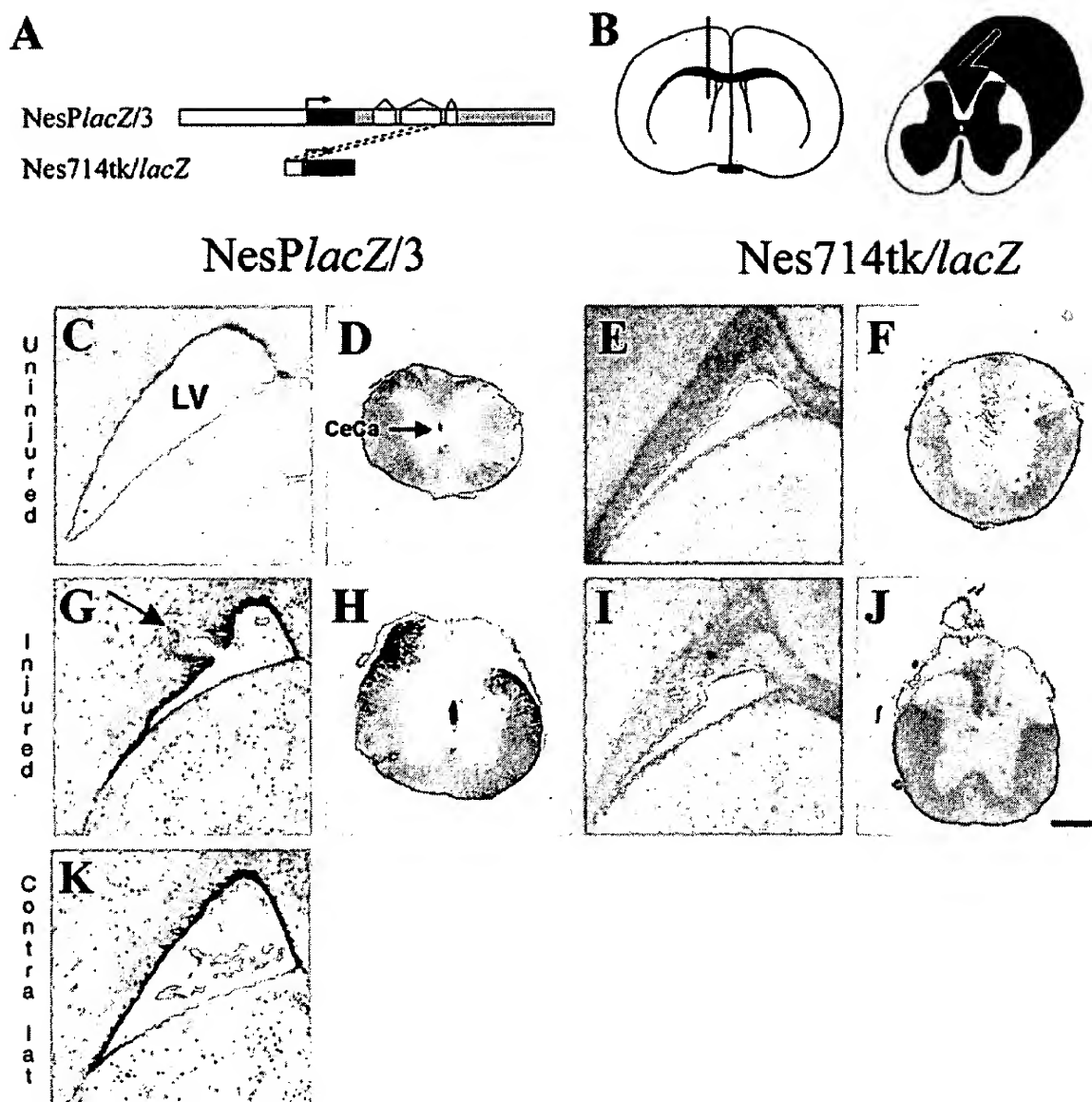
A

NesP*lacZ*/3

Nes714tk/*lacZ*

B

NesP*lacZ*/3

Nes714tk/*lacZ*

Fig. 1. LacZ expression in adult NesP*lacZ*/3 and Nes714tk/*lacZ* transgenic mice during normal conditions and after injury. **A:** Schematic depiction of the reporter constructs NesP*lacZ*/3 and Nes714tk/*lacZ*. The NesP*lacZ*/3 construct consists of the *lacZ* gene (blue) flanked by 5 kb of rat nestin upstream sequences and the complete genomic rat nestin gene, including the three introns (exons in grey, introns in white). The Nes714tk/*lacZ* construct carries 714 bp of the second intron of the human nestin gene (pink) in front of a basic thymidine kinase promoter (red) and the *lacZ* gene (blue). The region in the rat second intron corresponding to the human intron sequence is denoted by dashed lines. **B:** Schematic depiction of the brain and spinal cord injury paradigms. To the left, a coronal section of an adult mouse brain is shown with a needle trauma introduced into the left hemisphere; to the right ,a transection made to the dorsal funiculus of the spinal cord is depicted. **C–K:** X-gal histochemistry on sections from adult brain and spinal cord of NesP*lacZ*/3 and Nes714tk/*lacZ* transgenic mice. Note that robust lacZ expression was observed in normal (uninjured) NesP*lacZ*/3 mice in the ventricular wall of the brain (C) and in the cells surrounding the central canal in the spinal cord (D). Five days after injury, lacZ expressing cells were observed at the injury site in the left cortex (marked with an arrow). Note also the elevated expression of lacZ after injury, as compared to the uninjured situation, both at the ipsilateral (G) and contralateral (K) side. Five days after injury a clear increase in lacZ expression was observed in the spinal cord particularly in the dorsal horns (H). In the Nes714tk/*lacZ* mice, no detectable lacZ expression was observed in the brain or spinal cord of normal (uninjured) or injured animals (E,F,I,J). LV, lateral ventricle; CeCa, central canal. Scale bar = 100 μm (C,E,G,I,K); 400 μm (D,F,H,J).

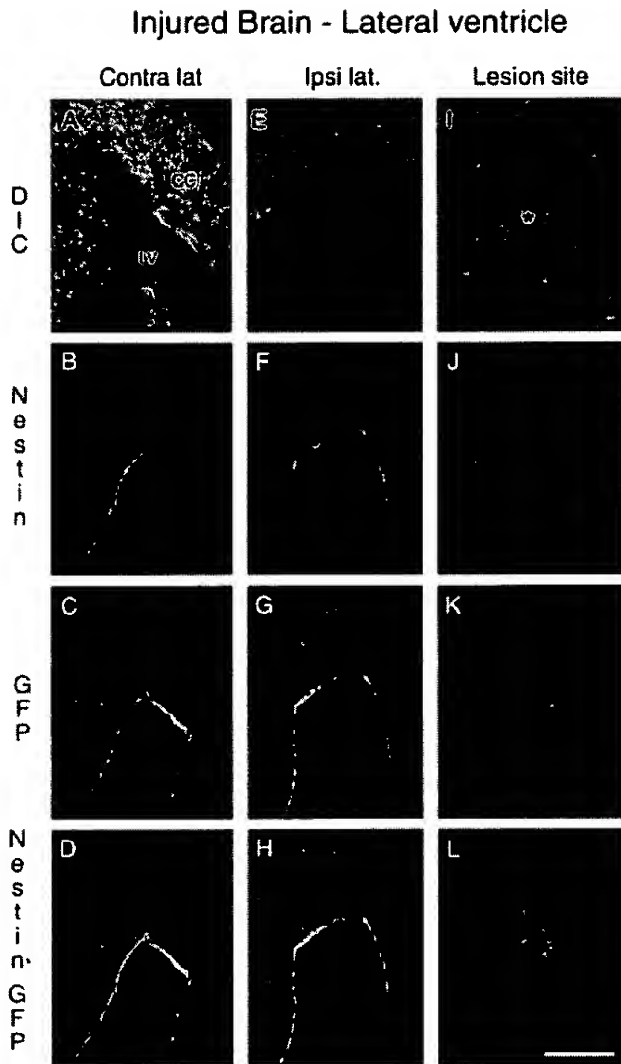## Injured Brain - Lateral ventricle

Fig. 2. Expression pattern of endogenous nestin and EGFP in adult E/nestin:EGFP transgenic mice after a needle insertion to the cortex. The analysis was made by DIC (A, E and I), anti-nestin immunohistochemistry (B, F and J) and EGFP expression (C, G and K). At both the ipsilateral and contralateral sides, nestin immunoreactivity was observed in both ependymal and subventricular zone cells under normal conditions (B,F), whereas EGFP was more restricted to the ependymal layer (C,G). The expression patterns were similar at the ipsilateral and contralateral sides. As seen in the merged images (D,H), coexpression between nestin and EGFP was not complete. I–L: Analysis at the site of the needle injury in cortex. Endogenous nestin was rapidly re-expressed in CNS after a lesion (J) whereas a more limited number of cells expressed EGFP (K). An asterisk indicates the lesion site (I). CC, corpus callosum; LV, lateral ventricle. Scale bar = 200 μm.

cated between the central canal and the site of injury now also expressed EGFP (Fig. 3G). Collectively, these data show that the 636 bp rat second intron enhancer is sufficient for adult CNS expression and that it at least partly can respond to CNS injury.

In Vitro Cultured Primary Astrocytes From NesPlacZ/3 and Nes714tk/lacZ Transgenic Mice Express LacZ

In addition to the expression in CNS stem cells, nestin is re-expressed in reactive astrocytes, both in vivo after injury and in CNS tumors, and also in astrocytes cultured in vitro (Frisén et al., 1995; Holmin et al., 1997; Pekny et al., 1999). Because the NesPlacZ/3 and Nes714tk/lacZ transgenic lines behaved differently in terms of lacZ expression in vivo, we wanted to learn whether in vitro cultured astrocytes from the two lines expressed the reporter gene. Astrocytes from postnatal day 2 mice were cultured for 14 days and analyzed by immunocytochemistry for expression of nestin and GFAP, or for staining with X-gal for β-galactosidase expression (Fig. 4). We found that primary astrocytes from both wild-type, NesPlacZ/3 and Nes714tk/lacZ mice, as expected, expressed endogenous nestin (Fig. 4A–C) and GFAP (Fig. 4D–F) proteins. Analysis of lacZ expression revealed that the wild-type astrocytes did not show any X-gal staining (Fig. 4G), whereas astrocytes from both the NesPlacZ/3 and Nes714tk/lacZ mice expressed the lacZ gene (Fig. 4H,I). The levels of lacZ expression were consistently three times higher in astrocytes from NesPlacZ/3 than from Nes714tk/lacZ astrocytes, as quantified by a luminometric assay for lacZ expression (Fig. 4J). These data show that the 714 bp enhancer element is sufficient for controlling expression in cultured astrocytes, but that additional sequences conferring quantitative control may be present elsewhere in the NesPlacZ/3 construct, because lacZ expression levels were higher in the NesPlacZ/3 mice.

In Vitro Cultured Adult Neural Stem Cells in Transgenic Mice Carrying the NesPlacZ/3 and Nes714tk/lacZ Constructs Express LacZ

It has been observed previously that cultured adult CNS stem cells express nestin in their undifferentiated state (Reynolds and Weiss, 1992; Johe et al., 1996; Johansson et al., 1999b) and we therefore analyzed NesPlacZ/3 and Nes714tk/lacZ mice for reporter gene expression in CNS stem cells cultured as neurospheres. Cells from the ventricular wall of the brain or the area immediately surrounding the central canal in the spinal cord were cultured as neurospheres for 14 days and then subjected to X-gal histochemistry. As expected, no X-gal staining was observed in neurospheres from wild-type mice (Fig. 5A,B). In neurospheres from the NesPlacZ/3 mice, we found that there was intense X-gal staining in neurospheres from both brain and spinal cord (Fig. 5C,D), whereas Nes714tk/lacZ-derived neurospheres from both brain and spinal cord showed a distinct but weaker X-gal staining located at the center of the neurosphere (Fig. 5E,F). The vast majority of X-gal positive cells were also reacting with the β-gal antibody (data not shown).

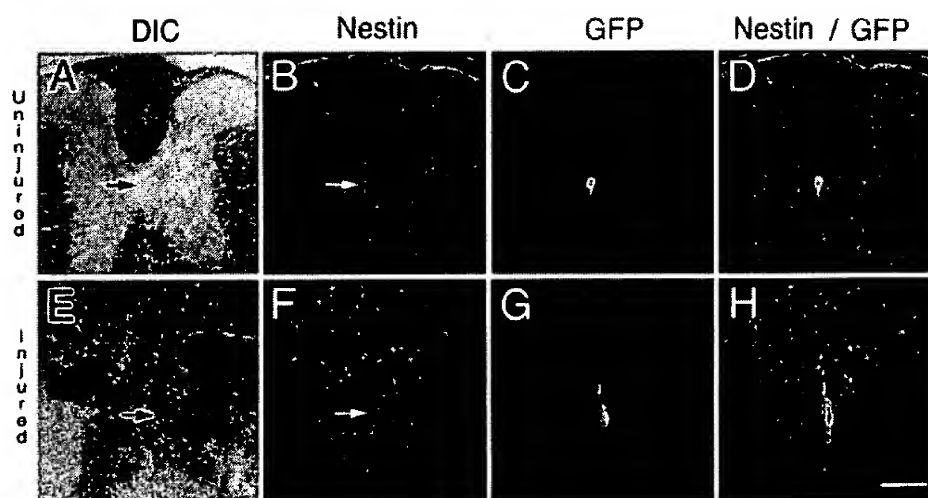To further address in which cell type lacZ was expressed, we carried out double-label immunohistochemistry

Fig. 3. DIC and immunohistochemistry analysis of the endogenous nestin and EGFP expression patterns in adult transgenic mice during normal condition and after a lesion to the spinal cord. A–D: Transverse section of an upper thoracic uninjured spinal cord. E–H: The corresponding pictures after injury. The analysis was made by DIC (A,E), anti-nestin immunohistochemistry (B,F) and EGFP expression (C,G). D is a merged image of B and C, and H is a merged image between F and G. (B) Normal expression of nestin visualized by anti-nestin immunoreactivity. Nestin expression was confined to endothelial and ependymal cells before injury (B), but more widespread after injury (F). The EGFP expression was restricted to ependymal cells before injury (D), but after injury EGFP-expressing cells were also found in the region between the central canal and the injury (G). Scale bar = 200 μm.

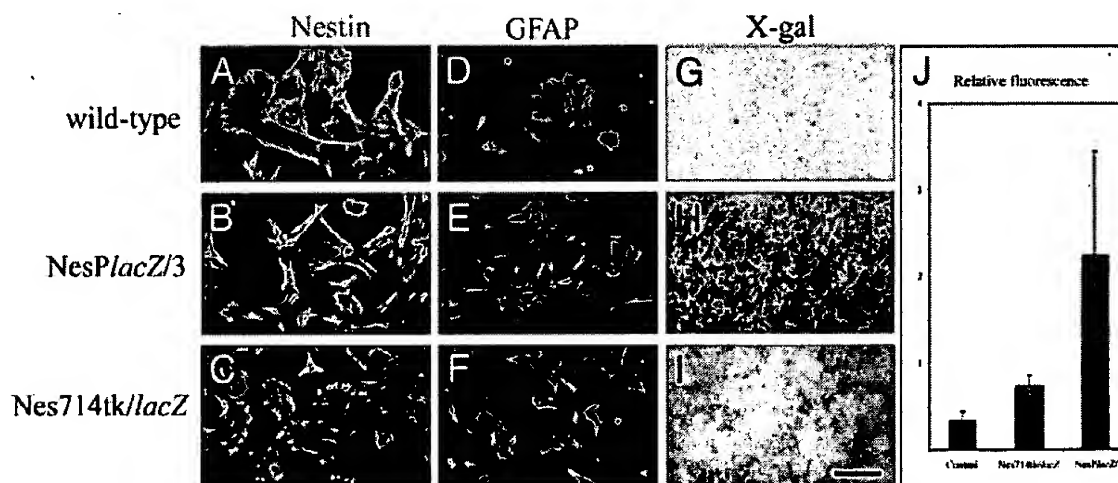Fig. 4. Immunocytochemistry with anti-nestin (A–C) and anti-GFAP (D–F) antisera and X-gal histochemistry (G–I) on primary astrocytes from postnatal day 2 wild-type, NesP*lacZ*/3 and Nes714tk/*lacZ* mice. Note that endogenous nestin and GFAP proteins are expressed in all cells. X-gal staining was observed in NesP*lacZ*/3 and Nes714tk/*lacZ* astrocytes, and was more intense in the former (H). Quantification by luminometric assay for lacZ expression revealed three-fold higher expression in NesP*lacZ*/3 astrocytes than in Nes714tk/*lacZ* astrocytes (J). Scale bar = 100 μm for A–F; 600 μm for G–I.

on lateral ventricle neurospheres from the NesP*lacZ*/3 mice, using an antibody against β-galactosidase combined with antibodies to nestin, GFAP or βIII-tubulin. Both nestin and GFAP immunoreactivity were observed in many cells of the neurosphere and in some cases seemed to colocalize with the β-galactosidase immunostaining, although colocalization was difficult to measure precisely because the β-galactosidase immunostaining in these cells is predom-

inantly nuclear (Fig. 5G,H). Of the β-galactosidase-positive cells, βIII-tubulin immunoreactivity was observed in less than 5% of the cells and coexpression with β-galactosidase could not be detected in the cells (Fig 5I), which may indicate that the *lacZ* gene is not expressed in differentiated neurons. Taken together, these results indicate that the 714 bp element is sufficient for expression in adult CNS stem cells cultured in vitro.
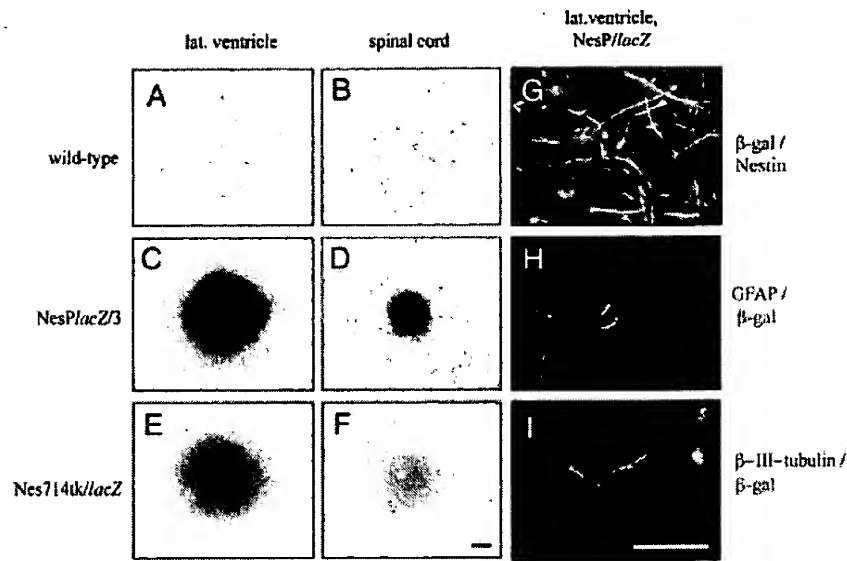
Fig. 5. Cultured adult CNS stem cells from NesP*lacZ*/3 and Nes714tk/*lacZ* transgenic mice express lacZ. A– F: X-gal histochemistry on cultured neurospheres generated from the ventricular wall of the brain and from the area immediately surrounding the central canal in the spinal cord. No X-gal staining is observed in neurospheres from wild-type mice (A,B). Neurospheres from NesP*lacZ*/3 mice show an intense X-gal staining (C,D), whereas neurospheres from Nes714tk/*lacZ* mice show weaker X-gal staining (E,F). (G–I) Double-label immunohistochemistry on lateral ventricle neurospheres from the NesP*lacZ*/3 mice with antibodies against β-galactosidase combined with antibodies to nestin, GFAP or brain specific tubulin (βIII-

tubulin). All three markers are expressed, demonstrating the presence of both undifferentiated and differentiated cells. Nestin immunoreactivity was observed in both the center and periphery of the neurosphere and colocalized extensively with the β-galactosidase immunoreactivity (G). GFAP immunoreactivity was confined to the center of the neurosphere (H), and was also largely colocalized with the β-galactosidase- positive cells. βIII-tubulin-positive cells were observed in the center with dendrites mediating from the neurosphere (I). β-galactosidase immunoreactivity was not observed in the dendrites, which may indicate that the *lacZ* gene was not expressed in differentiated neurons. Scale bar = 50 μm (A–F); 150 μm (G–I).

Human Second Intron is Sufficient for Expression of the *lacZ* Reporter Gene in the CNS Tumor Cell Line RG2

Nestin is re-expressed in CNS tumors, both in the tumor proper and in surrounding reactive astrocytes and endothelial cells, and the extent of nestin expression correlates with the severity of the tumor (Dahlstrand et al., 1992; Tohyama et al., 1992). To learn whether nestin expression in CNS tumor cells is regulated by the regulatory regions in the second intron and to explore the possibility of using adenovirus as a delivery system for genes under control of the nestin regulatory regions, we generated an adenovirus vector carrying the *lacZ* gene coupled to the basic thymidine kinase promoter and the complete second intron of the human nestin gene (ad.nes1852tk*lacZ*). We used ad.nes1852tk*lacZ* adenovirus particles to infect RG2 cells, which is a rat glioma cell line (Ko et al., 1980) expressing endogenous nestin (data not shown). As control, we infected JEG-3 cells in parallel; a human carcinoma cell line (Kohler and Bridson, 1971) that does not express nestin (data not shown). X-gal histochemistry revealed that noninfected RG2 and JEG-3 cells, as expected, did not stain blue (Fig. 6A,B). In contrast, infection with the ad.nes1852tk*lacZ* adenovirus resulted in a majority of RG2 cells expressing the *lacZ* gene,

although no blue cells were observed in the JEG-3 cells (Fig. 6C,D). As a control for adenovirus infectivity, we used a control adenovirus carrying *lacZ* under control of the general Rous sarcoma virus (RSV) promoter (ad.RS-V*lacZ*). Infection with the ad.RSV*lacZ* led to lacZ expression in the majority of both RG2 and JEG-3 cells (Fig. 6E,F), demonstrating that both cell lines could be infected readily with adenovirus vectors. These results show that the nestin second intron can direct nestin expression specifically to glioma cells expressing nestin, but that a nestin-negative tumor cell line does not express the reporter gene from the second intron.

DISCUSSION

We have analyzed the nestin enhancer requirements for adult CNS expression during normal conditions, after injury and in cells cultured ex vivo. We find that a 636 bp region of the rat second intron is sufficient for expression in the periventricular area of the brain and around the central canal of the spinal cord, whereas a corresponding region from the human second intron is not. Furthermore, the 636 bp rat region partly responds to CNS injury, whereas a more complete response is achieved by using a larger rat nestin construct. The human second intron sequences are, however, sufficient for expression in reac-
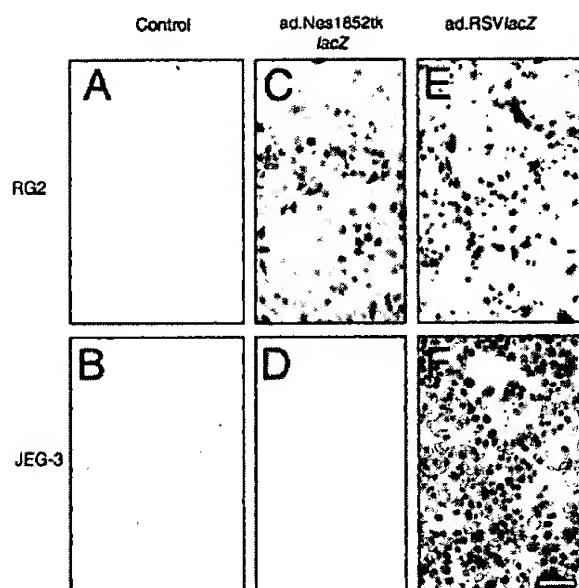
Fig. 6. The human nestin second intron controls expression in a nestin-positive CNS tumor cell line. Adenoviral particles with the second intron enhancer (ad.nes1852tk*lacZ*) were used to infect RG2 or JEG-3 cells and lacZ expression was analyzed by X-gal histochemistry. Non-infected RG2 (**A**) and JEG-3 (**B**) cells did not show any X-gal staining. In contrast, infection with ad.nes1852tk*lacZ* resulted in a robust X-gal staining in the RG2 cells (**C**), but not in JEG-3 cells (**D**). Infection with ad.RSV*lacZ* led to lacZ expression in both RG2 (**E**) and JEG-3 (**F**) cells. Scale bar =100 μm.

tive astrocytes and CNS stem cells cultured ex vivo, and for expression in a CNS tumor cell line.

The difference in expression in adult CNS from the E:nestin/EGFP and the nes714tk/*lacZ* mice was unexpected, considering that this region is the most highly conserved part of the second intron (Lothian and Lendahl, 1997) and that the embryonic CNS expression patterns are very similar for the two transgenic lines (Lothian and Lendahl, 1997; Kawaguchi et al., 2001). The most parsimonious explanation for this difference in expression is that there is a species difference between rat and man in terms of enhancer activity. It should be noted, however, that the use of two different reporter genes (GFP vs. lacZ expression) and different minimal promoters (hsp68 vs. tk) as well as the slight variation in genetic background (pure C57Bl6 vs. mixed CBA/C57Bl6) may partially influence the levels of expression. The comparison between the E:nestin/EGFP and the NesP*lacZ*/3 mice shows that the 636 bp region of the rat second intron is sufficient for transcription in adult brain and spinal cord under normal condition, but elements located outside this region probably play a role for a more complete injury response. This is based on the observation that expression levels were elevated both ipsilaterally and contralaterally in the periventricular area of NesP*lacZ*/3 mice, whereas this was not the case in E:nestin/EGFP mice. Moreover, the spinal cord response was more widespread and encompassed

expression in the dorsal horns in NesP*lacZ*/3 mice, which was not the case in E:nestin/EGFP mice. A comparison between the lacZ expression in the spinal core of the NesP*lacZ*/3 mice and the extent of upregulation of endogenous nestin (compare Fig. 1H and 3F), however, reveals that there may be additional elements even outside the 5 kb upstream sequence that are required for a complete injury response.

In contrast to the lack of detectable lacZ expression in the ventricular wall in vivo in the Nes714tk/*lacZ* mice, adult CNS stem cells cultured ex vivo as neurospheres expressed lacZ. This provides evidence that the transcriptional status of adult CNS stem cells is altered at the transition from the in vivo situation to in vitro culture, which may be a consequence of loss of cell-cell contact or exposure to a different repertoire of growth factors. As discussed above, the 714 bp region encompasses the most highly conserved region between human and rat in the second intron (Lothian and Lendahl, 1997), and binding sites for a number of transcription factors have been identified. For example, RXR, RAR, TR and COUP-TF, members of the nuclear receptor family, bind to elements in this region (Josephson et al., 1998; Lothian et al., 1999) and the POU domain factor Brn-2 has been shown by mutational analysis to be important, at least for embryonic expression (Josephson et al., 1998). It will be important to learn whether some of these factors are upregulated or activated at the transition from the in vivo state to in vitro culture. It should also be noted that although the 714 bp region is sufficient for expression in neurospheres, elements outside this region are likely to contribute quantitatively to the level of expression, because the lacZ expression was consistently higher in neurospheres from the NesP*lacZ*/3 mice, both from the brain and spinal cord. It should be kept in mind that different basic promoters were used in the NesP*lacZ*/3 and the Nes714tk/*lacZ* mice, which may to some extent influence expression levels. An increase in reporter gene transcription from the nestin enhancer at the transition from in vivo to in vitro CNS stem cell culture was also observed recently by Kawaguchi et al. (2001), as cells expressing moderate levels of EGFP in the ventricular wall became more intensively fluorescent when cultured in vitro. Taken together, these data support the notion that the 714 bp nestin enhancer becomes more active when the cells are taken out of the in vivo context.

Similar to the upregulation seen in cultured CNS stem cells, the 714 bp region was sufficient to induce reporter gene expression in cultured adult astrocytes. As is found with adult CNS stem cells, the levels of reporter gene expression in the astrocytes were higher from NesP*lacZ*/3 mice as compared to Nes714tk/*lacZ* mice. This may suggest that there is a similar transcriptional transition as for the stem cells when astrocytes are removed from the in vivo situation. Endogenous nestin expression can be upregulated in astrocytes also in vivo in response to various types of CNS injury (Frisén et al., 1995; Lin et al., 1995; Duggal et al., 1997; Holmin et al., 1997; Pekny et al., 1999), and activation of expression occurs quite a

distance away from the site of injury (unpublished observations). The factors mediating this rapid and widespread upregulation remain to be established, but the findings presented here on nestin enhancer activation upon ex vivo culturing may provide a good testing model for such factors.

We finally found that the complete second nestin intron coupled to *lacZ* in an adenovirus vector specifically directed expression to the nestin-positive CNS tumor cell line RG2 but not to JEG-3 cells, a cell line that does not express endogenous nestin. The observed specificity for expression only in a nestin-expressing tumor cell line is in keeping with a recent report from Kurihara et al. (2000). The specificity in expression is of considerable interest for the prospect of using the nestin enhancer to target expression of genes of interest directly to CNS tumor cells located in the brain. One therapeutically potentially interesting approach would be to direct expression of inducible suicide genes to the tumor cells using the nestin enhancer and a viral delivery system.

In conclusion, the data presented here argue that the adult CNS nestin enhancer is complex and modular, and contains species-unique and specific elements required for expression in cultured cells as well as for expression in neurogenic regions in vivo. This complex enhancer structure resembles the situation in the embryonic CNS, where nestin enhancer elements required for pan-neural as well as midbrain-specific expression have been identified (Josephson et al., 1998; Lothian et al., 1999; Yaworsky and Kappen, 1999).

ACKNOWLEDGMENTS

REFERENCES

Bjornson CRR, Rietze RL, Reynolds BA, Magli MC, Vescovi AL. 1999. Turning brain into blood: a hematopoietic fate adopted by adult neural stem cells in vivo. Science 283:534–537.

Cassidy R, Frisén J. 2001. Neurobiology: Stem cells on the brain. Nature 412:690–691.

Clarke D, Johansson C, Wilbertz J, Veress B, Nilsson E, Karlstrom H, Lendahl U, Frisén J. 2000. Generalized potential of adult neural stem cells. Science 288:1660–1663.

Dahlstrand J, Collins VP, Lendahl U. 1992. Expression of the Class VI intermediate filament nestin in human central nervous system tumors. Cancer Res 52:5334–5341.

Dahlstrand J, Lardelli M, Lendahl U. 1995. Nestin mRNA expression correlates with the CNS progenitor cell state in many, but not all, regions of developing CNS. Brain Res Dev Brain Res 84:109–129.

Doetsch F, Caillé I, Lim DA, Garcia-Verdugo JM, Alvarez-Buylla A. 1999. Subventricular zone astrocytes are neural stem cells in the adult mammalian brain. Cell 97:1–20.

Dracopoli NC. 1995. Current protocols in human genetics. New York: Current Protocols Corporation.

Duggal N, Schmidt-Kastner R, Hakim AM. 1997. Nestin expression in reactive astrocytes following focal cerebral ischemia in rats. Brain Res 768:1–9.

Fishell G, Mason CA, Hatten ME. 1993. Dispersion of neural progenitors within the germinal zones of the forebrain. Nature 362:636–638.

Frederiksen K, McKay R. 1988. Proliferation and differentiation of rat neuroepithelial precursor cells in vivo. J Neurosci 8:1144–1151.

Frisén J, Johansson CB, Török C, Risling M, Lendahl U. 1995. Rapid, widespread and long lasting induction of nestin contributes to the generation of glial scar tissue after CNS injury. J Cell Biol 131:453–464.

Frisén J, Verge V, Cullheim S, Persson H, Fried K, Middlemas D, Hunter T, Hokfelt T, Risling M. 1992. Increased levels of trkB mRNA and trkB protein-like immunoreactivity in the injured rat and cat spinal cord. Proc Natl Acad Sci USA 89:11282–11286.

Galli R, Borello U, Gritti A, Minasi M, Bjornson C, Coletta M, Mora M, Angelis MD, Fiocco R, Cossu G, Vescovi A. 2000. Skeletal myogenic potential of human and mouse neural stem cells. Nat Neurosci 3:986–991.

Gritti A, Cova L, Parati EA, Galli R, Vescovi AL. 1995. Basic fibroblast growth factor supports the proliferation of epidermal growth factor-generated neuronal precursor cells of the adult mouse CNS. Neurosci Lett 185:151–154.

Hirt B. 1967. Selective extraction of polyoma DNA from infected mouse cell cultures. J Mol Biol 26:365–369.

Hockfield S, McKay R. 1985. Identification of major cell classes in the developing mammalian nervous system. J Neurosci 5:3310–3328.

Holmin S, Almzvist P, Lendahl U, Mathiesen T. 1997. Adult nestin-expressing subependymal cells differentiate to astrocytes in response to brain injury. Eur J Neurosci 9:65–75.

Jacobson M. 1991. Developmental neurobiology. New York: Plenum Publishing Corp.

Johansson C, Momma S, Clarke D, Risling M, Lendahl U, Frisén J. 1999a. Identification of a neural stem cell in the adult mammalian central nervous system. Cell 96:25–34.

Johansson C, Svensson M, Wallstedt L, Janson A, Frisén J. 1999b. Neural stem cells in the adult human brain. Exp Cell Res 253:733–736.

Johe KK, Hazel TG, Muller T, Dugich-Djordjevic M, McKay RDG. 1996. Single factors direct the differentiation of stem cells from the fetal and adult central nervous system. Genes Dev 10:3129–3140.

Josephson R, Müller T, Pickel J, Okabe S, Reynolds K, Turner PA, Zimmer A, McKay RDG. 1998. POU transcription factors control expression of CNS stem cell-specific genes. Development 125:3087–3100.

Kawaguchi A, Miyata T, Sawamoto K, Takashita N, Murayama A, Akamatsu W, Ogawa M, Okabe M, Tano Y, Goldman S, Okano H. 2001. Nestin-EGFP transgenic mice: visualization of the self-renewal and multipotency of CNS stem cells. Mol Cell Neurosci 17:259–273.

Ko L, Koestner A, Wechsler W. 1980. Morphological characterization of nitrosourea-induced glioma cell lines and clones. Acta Neuropathol 51:23–31.

Kohler P, Bridson W. 1971. Isolation of hormone-producing clonal lines of human choriocarcinoma. J Clin Endocrinol 32: 683–687.

Kurihara H, Zama A, Tamura M, Takeda J, Sasaki T, Takeuchi T. 2000. Glioma/glioblastoma-specific adenoviral gene expression using the nestin gene regulator. Gene Ther 7:686–693.

Lendahl U, Zimmerman LB, McKay RDG. 1990. CNS stem cells express a new class of intermediate filament protein. Cell 60:585–595.

Lin RCS, Matesic DF, Marvin M, McKay RDG, Brüstle O. 1995. Reexpression of the intermediate filament nestin in reactive astrocytes. Neurobiol Dis 2:79–85.

Lois C, Alvarez-Buylla A. 1994. Long-distance neuronal migration in the adult mammalian brain. Science 264:1145–1148.

Lothian C, Lendahl U. 1997. An evolutionarily conserved region in the second intron of the human nestin gene directs gene expression to CNS progenitor cells and to early neural crest cells. Eur J Neurosci 9:452–462.

Lothian C, Prakash N, Lendahl U, Wahlström G. 1999. Identification of both general and region-specific embryonic CNS enhancer elements in the nestin promoter. Exp Cell Res 248:509–519.

Luskin MB, McDermott K. 1994. Divergent lineages for oligodendrocytes and astrocytes originating in the neonatal forebrain subventricular zone. Glia 11:211–226.

McCarthy KD, de Vellis J. 1980. Preparation of separate astroglial and oligo-dendroglial cell cultures from rat cerebral tissue. J Cell Biol 85:890–902.

Morshead CM, Reynolds BA, Craig CG, McBurney MW, Staines WA, Morassutti D, Weiss S, van der Kooy D. 1994. Neural stem cells in the adult mammalian forebrain: a relatively quiescent subpopulation of sub-ependymal cells. Neuron 13:1071–1082.

Nilsson E, Lendahl U. 1993. Transient expression of a human b-actin promoter/lacZ gene introduced into mouse embryos correlates with a low degree of methylation. Mol Repr Dev 34:149–157.

Pekny M, Johansson CB, Eliasson C, Stakeberg J, Wallén Å, Perlmann T, Lendahl U, Betsholtz C, Berthold C-H, Frisén J. 1999. Abnormal reaction to central nervous system injury in mice lacking glial fibrillary acidic protein and vimentin. J Cell Biol 145:503–514.

Reynolds BA, Weiss S. 1992. Generation of neurons and astrocytes from isolated cells of the adult mammalian central nervous system. Science 255:1707–1710.

Reynolds B, Weiss S. 1996. Clonal and population analyzes demonstrate that an EGF-responsive mammalian embryonic CNS precursor is a stem cell. Dev Biol 175:1–13.

Stow N. 1981. Cloning of a DNA fragment from the left-hand terminus of the adenovirus type 2 genome and its use in site-directed mutagenesis. J Virol 37:171–180.

Temple S, Davis AA. 1994. A self-renewing multipotential stem cell in embryonic rat cerebral cortex. Nature 372:263–266.

Tohyama T, Lee VM-Y, Rorke LB, Marvin M, McKay RDG, Trojanowski J. 1992. Nestin expression in embryonic human neuroepithelium and in human neuroepithelial tumor cells. Lab Invest 66:303–313.

Wang S, Barres B. 2000. Up a notch: instructing gliogenesis. Neuron 27:197.

Williams BP, Price J. 1995. Evidence for multiple precursor cell types in the embryonic rat cerebral cortex. Neuron 14:1–20.

Yaworsky PJ, Kappen C. 1999. Heterogeneity of neural progenitor cells revealed by enhancers in the nestin gene. Dev Biol 205:309–321.

Zimmerman L, Lendahl U, Cunningham M, McKay R, Parr B, Gavin B, Mann J, Vassileva G, McMahon AP. 1994. Independent regulatory elements in the nestin gene direct transgene expression to neural stem cells or muscle precursors. Neuron 12:11–24.